Electrospun Polymer Fiber Systems for Flexible Electronics

DISSERTATION

zur Erlangung des akademischen Grades eines Doktors

der Naturwissenschaften (Dr. rer. nat.)

in der Bayreuther Graduiertenschule für Mathematik und

Naturwissenschaften (BayNAT)

der Universität Bayreuth

vorgelegt von

Qiang Gao

Qinhuangdao City, Hebei Province, China

Bayreuth 2021

This doctoral thesis was prepared at the department of Macromolecular Chemistry II at the University of Bayreuth from 1/2018 until 10/2021 and was supervised by Prof. Dr. Andreas Greiner.

This is a full reprint of the thesis submitted to obtain the academic degree of Doctor of Natural Sciences (Dr. rer. nat.) and approved by the Bayreuth Graduate School of Mathematical and Natural Sciences (BayNAT) of the University of Bayreuth.

Date of submission: 03.11.2021

Date of defense: 26.01.2022

Acting director: Hans Keppler

Doctoral committee:

Prof. Dr. Andreas Greiner (reviewer)

Prof. Dr. Peter Strohriegl (reviewer)

Prof. Dr. Jürgen Senker (chairman)

Prof. Dr. Birgit Weber

(additional reviewer: Prof. Dr. Bin Ding)

The present dissertation is **Cumulative.**

Parts of the work have already been published as follows:

(1) **Q. Gao**, B. A. F. Kopera, J. Zhu, X. Liao, C. Gao, M. Retsch, S. Agarwal, A. Greiner.
Breathable and Flexible Polymer Membranes with Mechanoresponsive Electric Resistance.
Adv. Funct. Mater. **2020**, 30, 1907555.

(2) **Q. Gao**, T. Lauster, B. A. F. Kopera, M. Retsch, S. Agarwal, A. Greiner.
Breathable and Flexible Dual-sided Nonwovens with Adjustable Infrared Optical Performances for Smart Textile.
Adv. Funct. Mater. **2021**, 2108808.

(3) **Q. Gao**, T. Tran ,X. Liao, S. Rosenfeldt, C. Gao, H. Hou, M. Retsch, S. Agarwal, A. Greiner.
Ultralight heat-insulating, electrically conductive carbon fibrous sponges for wearable mechanosensing devices with advanced warming function.
(Submitted to ACS Applied Materials & Interfaces)

Table of Contents

List of Symbols and Abbreviations

1D	One-dimensional
2D	Two-dimensional
3D	Three-dimensional
A	Ampere
Ag	Silver
Au	Gold
cm	Centimeter
CNF	Carbon nanofiber
CNT	Carbon nanotube
Cu	Copper
EDX-SEM	Energy-dispersive X-ray-scanning electron microscopy
EMI	Electromagnetic interference
g	Gram
GF	Gauge factor
GO	Graphene oxide
h	Hour
IR	Infrared
m	Meter
N	Newton
NP	Nanoparticle
NW	Nanowire
LED	Light-emitting diode
m	Meter
mA	Milliampere
mg	Milligram
mL	Milliliter

List of Symbols and Abbreviations

MOF	Metal–organic framework
nm	Nanometer
NCS	Nanofibrous carbon sponge
P3HT	Poly (3-hexylthiophene)
PAN	Polyacrylonitrile
PANi	Polyaniline
PCL	Polycaprolactone
PDMS	Polydimethylsiloxane
PEDOT	Poly(3,4-ethylenedioxythiophene)
PEO	Poly(ethylene oxide)
PI	Polyimide
PLA	Poly(lactic acid)
PSS	Poly(styrene sulfonate)
PPy	Polypyrrole
PU	Polyurethane
PVA	Poly(vinyl alcohol)
PVDF	Poly (vinylidene fluoride)
s	Second
S	Siemens
SEM	Scanning electron microscopy
sq	Square
TEM	Transmission electron microscopy
TPU	Thermoplastic polyurethane
wt.%	Weight percent
U	Voltage
V	Volt
μm	Micrometer
Ω	Ohm
°C	Celsius

Summary/Zusammenfassung

Summary

Traditional heavy and rigid electronics, mostly based on metallic or semiconductor materials, are short of desirable sensitivity and flexibility, unsuitable applied as emerging flexible electronics devices in the aspect of mechanical sensors, wearable joule heating devices, conductors, optoelectronics, transistors, organic artificial synapses and energy harvesting and storage devices. The fiber-based structures and assemblies are highly demanded in wearable electronic devices, because of their expected to be flexible, lightweight, long-lasting, and shortening the carrier transportation pass in the way axial direction. The combination of high conductivity, desirable mechanical properties, breathability, optical transparency and low cost, gives the fibrous system a high possibility to be utilized in the next generation of flexible electronic devices.

This dissertation aimed to develop conductive systems based on electrospun polymer fibers simultaneously presenting excellent portability, mechanical flexibility and electrical conductivity, which could be utilized for emerging flexible electronics. To overcome the inherently non-conductive nature of conventional polymeric fibers, the underlying concept was to construct the advanced conductive system consisting of polymer fibers and conducting additives, or directly employing conductive carbonized polymer fibers, by the design of novel structures of dual-sided and sandwich-like membrane or porous sponge. These mechanically flexible fiber systems have been demonstrated for various wearable devices, such as wearable strain/pressure sensors and personal thermal management devices.

Breathable and flexible dual-sided nonwovens with tailored electrical and thermal properties are promising as smart textiles for personal thermal management. The dual-sided nonwoven consisting of polyimide (PI) electrospun nonwoven and silver nanowire (AgNW) networks presented significant differences of physical, electrical,

and thermal properties on the two sides, which can be tailored by using the amount of AgNW. The resultant dual-sided nonwoven possessed very low electrical resistance of 0.23 Ω sq^{-1} and excellent IR reflectance of more than 80 %, far higher than the normal textile. In addition, it could be integrated into a thermal management device by applying low current, realizing both functions of reducing heat dissipating into ambient air and heat compensation to the human body. Besides, the dual-sided membrane showed outstanding flexibility under different deformations, such as bending and crumpling deformations, as well as washing stability without sacrificing electrical resistance, very promising for next-generation wearable devices.

To improve the stretchability of conductive systems for strain sensors, we proposed a new strategy to fabricate sandwich-like electrically conductive membranes with very low electric resistance by employing elastic electrospun thermoplastic polyurethane (TPU) nonwovens as substrates. The sandwich-like conductive membrane consisted of an AgNW network sandwiched between two porous electrospun TPU nonwovens. Polycaprolactone (PCL) short fibers acted as glue and provide a strong interface between the three layers. Our membranes showed a high stretchability (breaking elongation more than 700 %) and very low initial electric resistance, as low as <0.1 Ω sq^{-1} depending upon the amount of AgNWs. The mechanoresponsive conductivity endows a potential for use as a strain sensor to monitor body movement and to be integrated into smart wearable devices to collect body movement signals using a connected personal computer or mobile phone in the future.

Furthermore, we explore ultralight carbon sponges by carbonizing graphene oxide (GO) -coated PI composite sponges. Intermediate modification with a polycation proved to be necessary for getting a stable and uniform GO coating on polymer precursor fibers. The resultant sponges demonstrate ultralow density, prominent mechanical flexibility, high electrical conductivity, and high thermal insulation as well as attractive mechanoresponsive electrical and thermal properties. Based on these advantageous characteristics, our sponge demonstrated a novel application for multifunctional wearable sensing systems with an advanced modality of thermal management.

In conclusion, advanced conductive systems have been fabricated in forms of flexible membrane and sponge composed of electrospun nanofibers and conducting additives. These advanced conductive systems demonstrated a variety of applications in flexible electronics, such as for strain/pressure sensors, flexible conductors and thermal management devices. The issues such as achieving high conductivity and flexibility, precise fabrication, and developing multifunctional portable devices are still to be improved.

Zusammenfassung

Herkömmliche schwere und starre Elektronik, die meist auf metallischen oder Halbleitermaterialien basiert, bietet nicht die gewünschte Empfindlichkeit und Flexibilität und ist daher ungeeignet für die Anwendung als aufstrebende flexible Elektronikgeräte in Form von mechanischen Sensoren, tragbaren Joule-Heizgeräten, Leitern, Optoelektronik, Transistoren, organischen künstlichen Synapsen und Geräten zur Energiegewinnung und -speicherung. Faserbasierte Strukturen und Baugruppen sind in tragbaren elektronischen Geräten sehr gefragt, da sie flexibel, leicht und langlebig sind und den Transportweg der Träger in axialer Richtung verkürzen. Die Kombination aus hoher Leitfähigkeit, wünschenswerten mechanischen Eigenschaften, Atmungsaktivität, optischer Transparenz und niedrigen Kosten gibt dem Fasersystem eine hohe Wahrscheinlichkeit, in der nächsten Generation flexibler elektronischer Geräte eingesetzt zu werden.

Ziel dieser Dissertation war es, leitfähige Systeme auf der Basis von elektrogesponnenen Polymerfasern zu entwickeln, die gleichzeitig eine hervorragende Tragbarkeit, mechanische Flexibilität und elektrische Leitfähigkeit aufweisen und für neu entstehende flexible Elektronik genutzt werden könnten. Um die nichtleitende Natur konventioneller Polymerfasern zu überwinden, bestand das zugrunde liegende Konzept darin, ein fortschrittliches leitfähiges System zu konstruieren, das aus Polymerfasern und leitenden Additiven besteht oder direkt leitfähige karbonisierte Polymerfasern verwendet, indem neuartige Strukturen aus doppelseitigen und sandwichartigen Membranen oder porösen Schwämmen entworfen werden. Diese mechanisch flexiblen Fasersysteme wurden für verschiedene tragbare Geräte, wie z. B. tragbare Dehnungs-/Drucksensoren und persönliche Wärmemanagementgeräte, demonstriert.

Atmungsaktive und flexible doppelseitige Vliesstoffe mit maßgeschneiderten elektrischen und thermischen Eigenschaften sind als intelligente Textilien für das persönliche Wärmemanagement vielversprechend. Der doppelseitige Vliesstoff, der aus einem elektrogesponnenen Polyimid-Vliesstoff (PI) und Silbernanodraht-

Summary/Zusammenfassung

Netzwerken (AgNW) besteht, weist auf beiden Seiten erhebliche Unterschiede in den physikalischen, elektrischen und thermischen Eigenschaften auf, die durch die Menge an AgNW maßgeschneidert werden können. Das daraus resultierende doppelseitige Vlies hatte einen sehr niedrigen elektrischen Widerstand von 0.23 Ω sq^{-1} und eine hervorragende IR-Reflexion von mehr als 80 %, die weit über der von normalen Textilien lag. Darüber hinaus konnte es durch die Anwendung von Schwachstrom in ein Wärmemanagementgerät integriert werden, wodurch beide Funktionen, die Verringerung der Wärmeabgabe an die Umgebungsluft und der Wärmeausgleich an den menschlichen Körper, realisiert werden konnten. Außerdem zeigte die doppelseitige Membran eine hervorragende Flexibilität bei verschiedenen Verformungen, wie z. B. Biegen und Zerknittern, sowie Waschstabilität ohne Einbußen beim elektrischen Widerstand, was für tragbare Geräte der nächsten Generation sehr vielversprechend ist.

Um die Dehnbarkeit leitfähiger Systeme für Dehnungssensoren zu verbessern, schlugen wir eine neue Strategie zur Herstellung sandwichartiger elektrisch leitfähiger Membranen mit sehr geringem elektrischem Widerstand vor, indem wir elastische elektrogesponnene thermoplastische Polyurethanvliese (TPU) als Substrate verwendeten. Die sandwichartige leitfähige Membran bestand aus einem AgNW-Netzwerk, das zwischen zwei porösen elektrogesponnenen TPU-Vliesstoffen eingebettet war. Kurze Fasern aus Polycaprolacton (PCL) fungierten als Klebstoff und bildeten eine starke Schnittstelle zwischen den drei Schichten. Unsere Membranen zeigten eine hohe Dehnbarkeit (Bruchdehnung von mehr als 700 %) und einen sehr niedrigen elektrischen Anfangswiderstand, der je nach Menge der AgNWs nur <0.1 Ω sq^{-1} betrug. Die mechanoresponsive Leitfähigkeit bietet das Potenzial, als Dehnungssensor zur Überwachung von Körperbewegungen eingesetzt zu werden und in Zukunft in intelligente tragbare Geräte integriert zu werden, um Körperbewegungssignale über einen angeschlossenen Computer oder ein Mobiltelefon zu erfassen.

Außerdem erforschen wir ultraleichte Kohlenstoffschwämme durch Karbonisierung von GO-beschichteten PI-Verbundschwämmen. Eine zwischenzeitliche Modifikation mit einem Polykation erwies sich als notwendig, um eine stabile und gleichmäßige GO-

Beschichtung auf den Polymervorläuferfasern zu erhalten. Die so entstandenen Schwämme weisen eine sehr geringe Dichte, eine hohe mechanische Flexibilität, eine hohe elektrische Leitfähigkeit und eine gute Wärmeisolierung, sowie attraktive mechanisch-flexible, elektrische und thermische Eigenschaften auf. Aufgrund dieser vorteilhaften Eigenschaften erwies sich unser Schwamm als geeignet für neuartige Anwendung für multifunktionale, tragbare Sensorsysteme mit einer fortschrittlichen Art des Wärmemanagements gezeigt.

Zusammenfassend kann gesagt werden, dass fortschrittliche leitfähige Systeme in Form von flexiblen Membranen und Schwämmen hergestellt wurden, die aus elektrogesponnenen Nanofasern und leitfähigen Additiven bestehen. Diese fortschrittlichen leitfähigen Systeme haben eine Vielzahl von Anwendungen in der flexiblen Elektronik gezeigt, z. B. für Dehnungs-/Drucksensoren, flexible Leiter und Wärmemanagementgeräte. Die probleme, wie das Erreichen einer hohen Leitfähigkeit und Flexibilität, die präzise Herstellung und die Entwicklung multifunktionaler tragbarer Geräte, müssen noch verbessert werden.

1. Introduction

1.1 Overview

Rapid progress in wearable technology allows us to imagine a large number of concepts related to the "Internet of things", such as electronic paper, wearable displays, electronic skins, implantable bioelectronics and smart gloves. Just as circuit miniaturization revolutionized the electronics industry in the 1905s, flexible electronics might also reshape the world in the future – if they have the flexibility desired, fulfilling the deformation requirements in daily life.[1, 2] Soft, skin-mounted electronics, for instance, that incorporate high-bandwidth, miniaturized motion sensors, enable digital, wireless measurements of mechanoacoustic signatures of both core vital signs (heart rate, respiratory rate and temperature) and underexplored biomarkers (coughing count) with high fidelity and immunity to ambient noises, have recently demonstrated their capability in continuous monitoring of COVID-19 infections in sick and healthy individuals in hospital and the home.[3] Flexibility can mean various properties to both manufacturers and users. As a mechanical characteristic, it is conveniently classified into three categories: (1) bendable or rollable, (2) permanently shaped, and (3) elastically deformed. Thus, currently most of fabrications is done on a flat workpiece that is shaped only as late as possible in the process, which benefits from the technology established by the planar integrated circuit and display industries.[4] Thus, the key building blocks of flexible electronics and sensing elements are capacitors, resistors, inductors, thin-film transistors, electrochemical elements and their combinations. The materials composed must possess remarkable tolerance to duplicated mechanical deformations. Most conventional high-performance electronic materials, such as metal, are stiff and heavy, whereas materials that are flexible and lightweight, such as conducting polymers, present undesirable electric properties. Utilizing the rational design of electronic circuits from both perspectives of material and structure, emerging flexible electrodes can perform high conductivity of metal level, have light weight, low

power consumption, low cost and are multifunctional under/in contact with various environments.[5-7] An essential property for flexible electronics with uses for human physiological health and physical movement monitoring is mechanical stress tolerance of the devices and their material constituents. These functional materials include the active semiconductor, the gate/interconnect dielectric, the charge injection/extraction promoting material and the conductor, as well as passive ones, such as the substrate, adhesion promoters, planarization and passivation materials, all of which are critical for the proper functioning of devices.[8-12] However, the conductor as a vital component of device integration is the dominant element in all electronic building blocks to determine the reliability and the bulk flexibility to mechanical stresses of the system. Conventional metallic wires have mechanical flexibility but poor deformation ability, endowing limited rigid circuit mechanical compliance to stress, resulting in severe limitation for integration in flexible devices due to an extreme mismatch of mechanical properties, because metals have typically > 100 –1000 times larger Young's moduli than those of common plastic substrates and human skin.[13, 14] Therefore, in order to construct reliable flexible conducting elements and minimize mechanical mismatches, a variety of strategies, such as the engineering design of the conducting lines (by using sputtering technology with mask, photolithographic processes or various printing technologies), employing conducting polymers (e.g. polypyrrole [PPy], polyaniline [PANi], poly(3,4-ethylenedioxythiophene) [PEDOT] and poly(styrene sulfonate) [PSS]), and structuring conductive nanostructures with conductive nanoscopic materials (e.g. metal nanoparticles, metal nanowires (NWs), carbon black, carbon nanotube (CNT), graphene, transition metal carbides), enable them to have a high tolerance to cracking and delamination upon stress.[2] The main challenge in flexible electronics is to incorporate the materials with the properties desired into the integrated systems whilst preserving the character of each component. Nanotechnology can play a role in achieving flexible systems with desirable functions. One-dimensional (1D) nanomaterials, such as nanorods, NWs, nanotubes and nanoribbons, are proven to be the most promising candidates as they can function as an electron pathway in the axial orientation, improve the carrier collection and shorten the carrier transport path.

Moreover, their prominent mechanical properties are essential for atomic-scale manipulation and further physiochemical properties. Thanks to the large surface area, 1D nanomaterials provide a high possibility to interact with a variety of inorganics at the surface.[15-17] Hence, fiber-based structures are highly demanded for wearable devices, which are expected to be flexible, lightweight and long-lasting. A large number of fibrous structures have been fabricated by well-established textile processing technologies under ambient surroundings. The hierarchical nature of fiber systems indicates that they are particularly suitable for the fabrication of flexible wearable devices. Multifunctional and multidimensional electrospun fibers can be engineered to have specific functions, for instance, surface hydrophobicity, electrical conductivity, antibacterial properties, antiwrinkle properties, selective light guidance and scattering, and thermal management. Such materials can be achieved by surface coating, patterning, filler mixing, freezing-dry, or foaming technologies.[18-20] Electrospun fibers enable the effective shortening of the carrier transportation path and enhance the carrier collection ability by functioning as an electron expressway in the axial direction. The combination of this merit and other unique features, such as light weight, high specific surface area, prominent mechanical properties, breathability, optical transparency and low cost, give the fiber system a great possibility of being utilized in the next generation of flexible electronic devices (**Figure 1-1**).[21-25]

Figure 1-1. Features of electrospun polymer fibers and their diverse applications for flexible electronics. Reprinted with permission from ref[26] (Copyright © 2019, American Chemical Society), ref[27] (Copyright © 2020, The Royal Society of Chemistry), ref[28] (Copyright © 2019, WILEY-VCH), ref[25] (Copyright © 2019, American Chemical Society), ref[29] (Copyright © 2019, The Royal Society of Chemistry), ref[30] (Copyright © 2019, American Chemical Society), ref[31] (Copyright © 2017, WILEY-VCH), ref[32] (Copyright © 2017, American Chemical Society), ref[33] (Copyright © 2017, Elsevier), ref[34] (Copyright © 2013, IOP), respectively.

1.2 Electrospinning technology

1.2.1 History of electrospinning

William Gilbert first observed that when a suitably electrically charged piece of amber was brought near a droplet of water it would form a cone shape and small droplets would be ejected from the tip of the cone in a study as early as the 17th century, which is the first recorded observation of the interaction of liquid droplets with the charged object.[35] In 1745, Bose demonstrated that water could be sprayed to form an aerosol with electrostatically charges.[36] Then in 1885, Lord Rayleigh systematically studied the behaviors of charged droplets and reckoned the maximum amount of charges which rejected a liquid droplet from the surface of liquid jets.[37] In 1887, Charles V. Boys discovered that viscoelastic liquid could be used to draw fibers by an apparatus consisting of an insulated disk in an external electric field, which demonstrated that a viscous liquid, such as beeswax and collodion, could be stretched into fine fibers at the edge of the disk.[38] In 1902 and 1903, John Francis Cooley described methods and the apparatus for dispersion of fluids by means of electrostatic force in several patents. Meanwhile, W. J. Morton proposed most of spinning methods with the assistance of using indirect and direct electric charging. Between 1931 and 1944, Anton Formhals made significant progresses to the development of electrospinning through a series of patents on aspects of the process taken out in America, France, the United Kingdom and Germany.[39] During this period, the cellulose acetate fibers were processed by electrospinning for the first time. He also investigated and introduced many other methods for composite fiber production in 1940.[35] In 1952, Bernard Vonnegut and Raymond L. Neubauer investigated the production of liquid jets by electrostatic force.[40] They noted the formation of uniformly sized droplets and estimated the size of the droplets. Between 1964 to 1969, Sir Geoffrey Ingram Taylor produced a significant advance in the theoretical underpinning of electrospinning by mathematically modeling the shape of the cone formed by the fluid droplet under the influence of an electric field, which is now known as the Taylor cone.[41] In 1971, Peter

Karl Baumgarten devised a method for photographing electrospun fibers in flight, and in the course of investigating the effects of solution viscosity, surrounding gas, voltage and jet radius on fiber diameter and jet length.[42] However, these early discoveries had not stimulated widespread interest in the industry, despite some explorations on filter applications were reported.[43]

From 1990, Darrell Reneker, Gregory Rutledge and a couple of other groups restarted focusing on the electrospinning technique by employing electronic microscopes to make it possible to access the features down to the nanoscale.[44-50] It was reported by those researchers that a variety of polymers could be used to fabricate nanofibers via this technique, which was termed electrospinning. Those studies gave a new life to electrospinning, by which continuous fibers with a nano-diameter were eventually produced. Notably, at the beginning of the 21st century, it attracted increasing attention and fiber composites prepared via electrospinning consisting of a mixture of organic and inorganic materials lead to the opening of a new world based on this technique.[51, 52] Additionally, as the fabricating technique improved dramatically, aligned fibers, coaxial fibers and yarns were developed, demonstrating the feasibility of tailoring the size, structure, porosity, composition and morphology of fibers[52-56], which greatly enhanced their applications, such as in the field of energy, environment, electronics, and biomedicine.

1.2.2 Principle of electrospinning

Electrospinning is a very simple and versatile way to fabricate fibers with a diameter in the range from nanometer to micrometer scale. The basic setup of electrospinning in a laboratory scale is shown in **Figure 1-2a**, consisting of a reservoir of polymer solution fed by an injecting pump, a high-voltage source connecting to the nozzle and the grounded collector. Polymer solution or melt is pumped to feed through a thin nozzle serving as an electrode, to which a high voltage ($100 - 500$ kV m^{-1}) is connected. A
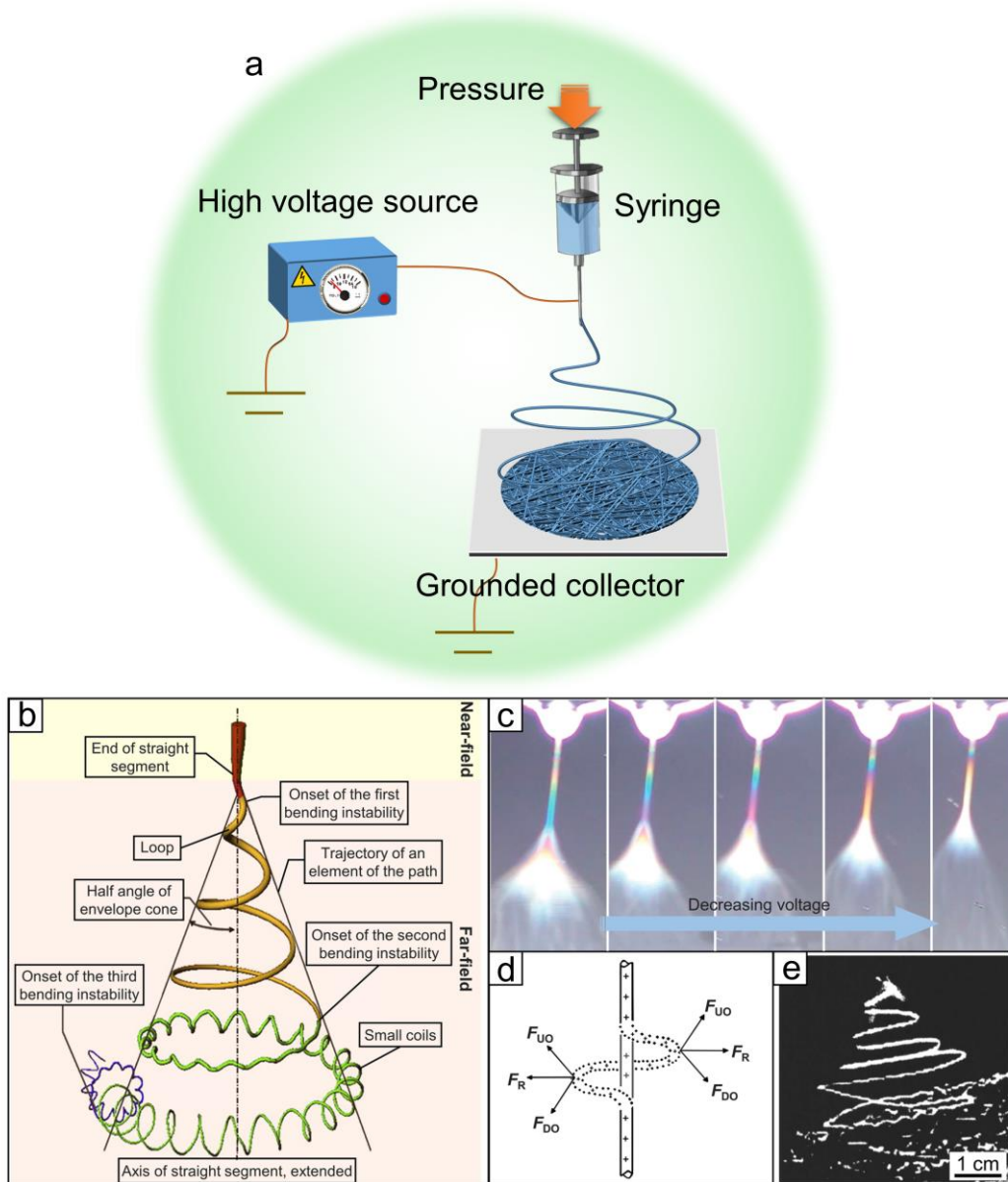
Figure 1-2. (a) Schematic diagram of electrospinning in laboratory. (b) Diagram depicting the pass of an electrospun jet. (c) Characteristic interference colors observed in the straight segment of a jet comprised of aqueous poly(ethylene oxide) (PEO), providing live information about the jet diameter and length of straight segment as a function of the applied voltage. (d) Schematic illustration of the forces acting on a charged jet. (F_{DO}: downward and outward force; F_{UO}: upward and outward force; F_R: radial direction force.). (e) Stereographic image showing the instantaneous position of the bending jet during the different stages of bending instabilities. (b, c and e) Reprinted with permission from ref[57]. Copyright © 2006 American Chemical Society. (d) Reprinted with permission from ref[58]. Copyright © 2008 Elsevier.

collector with a substrate, usually serving as a counter electrode, is placed at a distance of 10 – 25 cm to collect the fibers produced. In principle, electrospinning involves an electrohydrodynamic process[57, 58], during which a viscous liquid droplet is electrified to form a jet, followed by stretching and extending in the electrical force to generate fibers, and can execute vertically or horizontally. During electrospinning, the polymer solution or melt is extruded to form droplets at the tip of the nozzle, which further evolve into a Taylor cone upon electrification, and then produce a liquid jet. The jet initially extends in a straight line and then undergoes violent whipping motions due to bending instabilities to stretch into a thinner diameter and solidifies into fibers deposited on the grounded collector. The diagram is shown in **Figures 1-2b** to **1-2e**.

1.2.3 Materials of electrospinning

In theory, any soluble or fusible polymer can be processed into fibers by the electrospinning technique via adjusting molecular parameters (such as solubility, glass-transition temperature, melting point, crystallization velocity, molecular weight, molecular weight distribution, entanglement density, solvent vapor pressure, and pH value) and the process parameters (such as concentration, electrical conductivity, surface tension, feed rate, electrode separation and geometry, temperature, and relative humidity).[43] When taking sol-gel chemistry into consideration, varieties of composite materials containing nanoscale components, such as nanoparticles, nanorods, NWs, nanotubes and nanosheets, provide more feasible candidates to produce nanofibers by electrospinning. These diversified candidate materials could be illustrated into macromolecules, small molecules, colloids and composites.

a). Macromolecules

Most of the macromolecules, including both natural and synthetic materials, can be processed into fibers by electrospinning. Synthetic macromolecule (e.g. polystyrene, poly(vinyl chloride) and PEO) has currently been reported to produce electrospun nanofibers for environmental protection. Polycaprolactone (PCL), polylactic acid (PLA) and poly(lactic-co-glycolic acid) and other biodegradable materials are utilized to

fabricate tissue scaffolds via electrospinning in biomedical applications. Moreover, natural materials, for example, gelatin, collagen, chitosan, chitin and silk fibroin, are more widely used to produce nanofiber-related devices in biomedicine and demonstrate a lower biotoxicity than synthetic materials. Conductive materials, such as PANi, PPy, PEDOT and PSS, could also be electrospun into fibers, and are commonly applied in electronics and energy.[59] In addition, poly(tetrafluoroethylene) and poly (vinylidene fluoride) (PVDF) are reported to be electrospun into fibers for designing nanogenerators due to their excellent piezoelectric and/or pyroelectric properties.

b). Small molecules

When molecular chains significantly entangle and overlap in solution to stabilize the electrified jet, those small molecules can be processed directly into fibers by electrospinning. Presently, amphiphiles and cyclodextrin derivatives are reported to be electrospun into fibers in a suitable solvent system and concentration (usually surpassing critical micelle concentration).[60, 61] Matthew G. McKee firstly reported highly entangled lecithin solution in a 70/30 wt% mixture of chloroform and dimethylformamide at a concentration of 43 wt% which was used to continuously electrospun fibers.[62] In addition, other small molecules, such as surfactants and peptides, can also be electrospun into fibers. Similarly, even though the cyclodextrin derivatives are amorphous small molecules, Asli Celebioglu produced cyclodextrin nanofibers/nanowebs in good mechanical integrity as free-standing materials.[63]

c). Colloidal materials

In sol-gel chemistry, a colloid with sufficient entangled particles to maintain a continuous jet is also a candidate for electrospinning. Typically, metal oxides, such as NiO, Co_3O_4, and a mixture of Al_2O_3 and ZnO, have been reported to process ceramic fibers by direct electrospinning with diameters in several micrometers. Additionally, dispersions of metal nanoparticles in high concentration could be used to produce a spinnable mixture initially, followed by thermal annealing to weld into metal fibers. However, the difficulty in preparing highly concentrated suspensions of metal particles makes it extremely restrictive to electrospun fiber by this method. In another study, the aged silica sols prepared in a system of tetraethyl orthosilicate, distilled water, ethanol

and HCl was used to electrospin into nanofibers with a diameter in the range of 0.4 – 1.0 μm, and can further decrease to thinner than 400 nm by tuning the aged sols.[64, 65]

d). Composite materials

In order to prepare functional fibers, solutions containing certain or multiple nanocomponents are normally used for electrospinning. Zero-dimensional nanoparticles (AuNP, AgNP, SiO_2 NP, TiO_2 NP), 1D nanorods or NWs (Au nanorod, AuNW, AgNW, CNT) and 2D nanosheet (graphene, nanoclay, Mxene, WS_2) are widely reported to be prepared as an electrospinning solution by intense stirring or ultrasonic shaking nanocomponents.[66-70] The electrospinnability of composite solutions relies critically on the concentration, shape and size of the components integrated, which greatly affect the morphology of the resultant fibers. A stable and well-dispersed system is beneficial for forming nanofibers consisting of homogenously distributed nanocomponents. However, if those nanocomponents aggregate during the electrospinning process, nonuniformed fibers with numerous parts of aggregated nanocomponents form easily.[68] The surface modification of nanocomponents is an effective way to stabilize a composite solution consisting of nanocomponents. The size and concentration of nanocomponents also influence the dispersity and the resultant fiber morphology. Regarding the nanoparticle system, if the size of the particle is far smaller than the fiber diameter, particles are inclined to be encapsulated inside completely, forming a smooth surface of fiber. On the contrary, fibers prepared from a composite solution consisting of larger particles present a rough surface or necklace-like morphology of fibers.[71] This situation is also the same for fibers consisting of nanosheets, of which the size plays a significant role similar to the fiber morphology. The 1D nanocomponents with anisotropy are usually well-oriented parallel along the fibers as the impact of stretching during the electrospinning process.[69] Additionally, metal-organic framework (MOF), covalent organic framework, zeolitic imidazolate frameworks nanofibers emerge and attract a lot of attention, by precursor electrospinning and then conducting a sol-gel reaction.[72-74] Depending on the target MOF and different applications, the MOF-polymer system has been optimized, involving choosing of a suitable polymer solution, MOF slurry property and

electrospinning condition. The polymer phase in MOF composite fibers acts as a binder to endow flexibility to the fibers. However, the redundant polymer phase could block the pore structure and reduce the functional surface, causing poorly applied performance.

1.2.4 Methods of electrospinning

Classical electrospinning usually equipped with a single-nozzle, depicted in Figure 1-6a, is typically conducted in a far-field mode (height: 5 – 15 cm) in a laboratory scale for generating nanofiber. In this case, it is hard to precisely control the deposition of electrospun fibers as designed due to the drastic whipping instability. However, in the situation of near-field mode (500 μm – 5 cm), the polymeric liquid jet will be directly written onto the collector before approaching unpredicted whipping instability, which makes processing patterned fibers possible even in both the X and Y-axis directions.[75, 76] During this process, it is extremely critical to use a low voltage (0.60 – 3.00 kV) to keep the liquid jet stable and a lower extruding rate of liquid (0.01 – 1.00 mL/h). As the polymeric liquid jet cannot be stretched in the electrical field, the fibers achieved are normally thicker than those produced in a standard process, in the diameter of microscale. In order to improve the low yield of laboratory scale, a multiple-needle electrospinning system is put into the effort to replace the single needle system. An array-needle system is designed to achieve this goal. The productivity of nanofiber is significantly enhanced but the instability of multiple jets in the electrical field causes some problems for the electrospun nanofibers, such as undesirable reactions, poor fiber distribution in the collector or a bonding reaction among fibers. This has been observed in previous studies and needs further investigation in order to be resolved.[77] In order to improve the instability, a secondary electrical field between the needles and the electrode generated by auxiliary electrodes is introduced to neutralize the repulsion among the needles.[78, 79] Additionally, various types of spinneret, such as solid pin, flat plate, metal string, and a hollowed tube with holes allowing multiple jets to eject simultaneously for electrospinning, have been designed to enhance the yield of

nanofiber as well.[80-82] However, it is still hard to control the flow rate of liquid to emanate uniform jets precisely. Using a moving spinneret can solve this issue, such as in one example of using a rotating disc with a sharp edge to eject uniform jets.

Compared to typical single needle electrospinning, the coaxial electrospinning technique is often used to fabricate nanofibers of nonsingular components via a designed coaxial needle, which usually consists of a bigger external needle and one or smaller internal needle(s) in the coaxial configuration, driven by corresponding connected pumps. Coaxial electrospinning allows the fabrication of nanofibers by defined components in a core-shell structure, even regarding those uneasily spinnable materials, such as oligomers, metal salts, oils, crystal particles, or even living components (protein/RNA/DNA/cells/bacterial/viruses) encapsulated into nanofibers.[83-86] When a core or shell component is removed by solvents (not dissolving the other component), hollow nanotubes or thinner nanofibers can be achieved. In addition, side-by-side electrospinning by a spinneret comprising a split of outlets side-by-side is often to produce fibers with different components.[87] Unlike coaxial electrospinning, a nanofiber of side-by-side electrospinning allows both components with equal surface exposure to the environment, expressing the distinguished properties of each component of the fiber.

Different types of collectors have been developed to prepare nanofibers in terms of a need to replace the grounded conductive plate, mainly including solid and liquid bath setups. Those solid collectors can be designed with different materials (insulator, semiconductor and conductor) and into specific patterns (aligned or radical columns, raised or sunk microstructure) in order to obtain a better distribution of the electrical field and fiber deposition.[88-90] Moreover, a movable collector (horizontal, vertical or rotating movement) will be employed to generate well-aligned fibers.[91] Additionally, a rotating drum or funnel can be used to fabricate twisted yarn.[92, 93] Based on a similar principle, a liquid bath, greatly enhancing the solidification of the jet, was demonstrated to collect nanofibers on a liquid surface and then twisting into yarn by a vertex action and collected by a rotating drum, in which the vertex plays the role of a rotating funnel.[94, 95]

1.2.5 Short electrospun nanofiber

Electrospinning is a versatile technology to produce continuous nanofibers. However, short electrospun fibers have enhanced and extended the applications of electrospun nanofibers extensively. Short electrospun nanofibers can be currently produced by different methods. Direct electrospinning is a one-step method to prepare short electrospun fibers. A number of key factors, such as the polymer structure (linear or branched), molecular weight, solvent system, and solution concentration, should be taken into higher consideration when directly electrospinning short fibers.[96, 97] In addition, the effect of concentration and surface charges of the nanoparticles incorporated into the electrospinning solution also concerns factors that affect the length and morphology of the short fibers. Photolithography was also reported to produce short fibers. Either polymers with double bonds with a photocross-linker and photoinitiator or known photochemistry of coumarin without the addition of the photocross-linker and photoinitiator was utilized for preparing short electrospun fibers from long electrospun fibers. A mask with a defined slit width can be utilized to control the length of the short fibers targeted. Short fibers could be derived from those insoluble parts of long fibers exposed to ultraviolet light b removing those non-cross-linked parts in an appropriate solvent.[98] The mechanical cutting technology is the most popular way to prepare short electrospun fibers at present, including the simple blade cutting and ultrasonic homogenization method. A razor is usually employed to chop long fibers into short ones manually, which is a time-consuming and low-efficiency method of preparation, merely fitting for small-scale preparation. Another method is by employing a homogenizer or motor-driven blades to cut electrospun membrane into short fibers. In this method, liquid nitrogen is generally used to assist the cutting by decreasing the temperature of dispersion. Short electrospun fibers have various applications regarding those assemblies in different dimension formations from 1D to 3D assemblies or as filler to prepare composites, such as using them as reinforced components to significantly enhance the mechanical property[99, 100], incorporating them into a hydrogel to mimic a natural tissue scaffold[101] or embedding into an injectable hydrogel

for various biomedical applications[102, 103].

In order to produce economic nanofibrous flexible devices, electrospinning technology is a suitable candidate because various materials and conductive additives have been successfully fabricated from conductive nanofibers and/or conductive nanofiber composites. The nanofibers or nanofiber composites obtained present high porosity, exciting mechanical properties, a large surface area, ultrahigh flexibility and excellent conductivity, whilst being cost-effective, efficient and have the ability to be prepared on a large-scale preparation. In addition, diverse nanofiber assemblies are crucial to fabricate diverse sizes, of soft, breathable, lightweight and conformable wearable devices. Moreover, the electrospun nanofibers derived from biocompatible materials achieve substrate for flexible electronics directly interfacing with cells, tissues and organs.[104-106] Thus, the nanofibrous flexible system holds great promise for application in smart wearable devices at the frontiers of science.

1.3 Materials for flexible electronics

1.3.1 Conducting materials

a). Metal NWs

The growth of metallic NWs[107], such as copper (Cu), silver (Ag) and gold (Au), has already been widely reported in the past few decades. These metallic NWs have been prepared mainly by the template, electrochemical, wet chemical and polyol methods. Among them, AgNW is particularly attractive due to the prominent electrical properties. The AgNWs synthesized with the polyol method generally possess a typical diameter of 20 – 150 nm and a length in the range of a few to several hundred micrometers. The high electrical conductivity makes it more popular in the electronics industry compared to other materials, such as carbon-based materials or conductive polymers. Nevertheless, mechanical and electrical stability issues remain a challenge for applying them in the electronics industry. In order to fabricate conductive two-dimensional (2D) networks with high mechanical flexibility and stability, using flexible polymers as

substrates can well resolve this issue to construct composites combined with AgNWs by employing the techniques of spinning, drop-, spray, dip, or Mayer rod coating, and roll-to-roll lamination production.[108] In addition, printing technologies, such as ink-jet, screen printing gravure, and three-dimensional (3D) printing have been applied in AgNW 3D-network preparation, which makes large-scale manufacturing with low costs possible.[109, 110] Moreover, 3D pure AgNW network could be constructed by the ice templated method, without combining with a polymer matrix, which allows structural control of the 3D AgNW networks and presents lower AgNW content without degrading the density of the AgNW networks, resulting in significantly improving the conductivity and stretchability.[111] Nevertheless, 3D pure AgNW networks have unique anisotropic microporous structures, low density, high conductivity, but exhibit elastic stiffening behavior with Young's modulus inducing low mechanical flexibility, which would limit its application in flexible devices.[112] In order to overcome the issue of poor flexibility, a strategy is to induce a polymer or other flexible matrix, constructing 3D AgNW networks composites.[113-115] Previous research has indicated that when the AgNW diameter approaches the mean free path of electrons in the bulk material, the proportion of electrons undergoing surface scattering increases, resulting in an increase in AgNW resistivity. Using longer AgNWs helps to construct higher electrically conductive networks since it allows one to reduce the number of junction points involved in electrical percolating webs.[116] In this case, transparent electrodes combined with longer AgNWs show higher transparency, which fits for meeting the fabricating criteria in optoelectronic devices.[117]

The AgNW has been proved to have superior performance in flexible electronics, but the high price of Ag has limited the intensive use of this appealing approach. Whereas, CuNW has been explored as a potential substitute for Ag for applications in electronics because of its abundant amount and cheap cost, which makes it economically fascinating for applications. The CuNW can be currently prepared by following two methods: (1) Ethylenediamine-mediated synthesis or (2) alkylamine-mediated synthesis. Regardless of the synthesis method, the unifying principle of synthesis involves the reduction of Cu ions to their metal state in the company of the capping

agents which induce 1D growth. As a kind of active metal in air, the CuNWs fabricated need to encapsulate an extra layer of hydrophobic polymers, such as poly(methyl methacrylate), polyamide, and polydimethylsiloxane (PDMS), to prevent CuNWs from an oxidation reaction in a harsh environment.[118] Apart from using polymer encapsulation, graphene coating has also been demonstrated to alleviate the oxidation of CuNWs efficiently.[119] Methods such as thermal annealing, photonic welding or laser-induced welding can be used for improving conductivity by reducing the adjunction resistance for large-scale fabrication.[120-122] Up to date, the CuNWs have been widely investigated for various applications, such as transparent conductors, nanogererators, joule heaters and sensors using fabrication methods including sputtering , printing, spinning/blade coating and vacuum filtration.[123-126]

Intensive recent works have reported Ag- and Cu-NWs in applications for flexible electronics thanks to their high conductivity, excellent flexibility, simple synthesis method and low cost. However, some disadvantageous features such as easy to oxidation or rust, resulted in poor conductivity, which limits their applications in harsh environments. These issues could be conquered by importing inert metal, such as Au or platinum NWs.[127, 128] However the high cost of these novel metals restricts their applications, especially in large-scale fabrication.

b). Carbon material

Apart from metal materials, carbon materials have been considered as prominent candidates to be utilized for flexible electronics, including CNT, graphene and its derivatives, graphite, carbon black and carbon materials derived from natural-material. Carbon materials, compared to other candidates, present unique advantages, such as high chemical and thermal stability, low toxicity, good electrical conductivity, and are an easily functionalized property, endowing them with great promising applications in flexible electronics. The basic properties of carbon materials are illustrated in **Table 1-1**. Based on these unique superiorities, carbon materials have been developed as functional components for flexible wearable devices, such as stretchable/pressing mechanical sensors, temperature/humidity sensors, electrochemical devices, wearable healthcare systems and energy devices (e.g. nanogenerators, supercapacitors and Li

batteries).[129-132]

Table 1-1. Comparison of basic properties of carbon materials and metal materials.[133]

Materials	Carbon	Metal
Electrical conductivity/ S m^{-1}	0.17-2.0×10^7 (CNTs); ~10^8 (graphene); 2.0-3.0×10^5 (graphite); 1.25-2.0×10^3 (amorphous)	6.3×10^7 (Ag); 5.96×10^7 (Cu); 4.10×10^7 (Au)
Chemical /thermal stability	Superior	Inferior
Chemical modification	Yes	No
Metallic or semiconductive	Metallic; semimetallic; semiconductive	Metallic
Morphology variety	Rich	Poor
Lightweight	Good	Poor

Additionally, advanced integrated wearable systems for the comprehensive diagnosis of personal healthcare and the simultaneous monitoring of physical actions and physiological indicators are highly demanded, serving as an integrated multifunctional platform. Hence, the integration of various flexible electronics based on carbon materials are exploited for physical, physiological and biochemical sensing devices combined with flexible power functionality. Various carbon materials have been exploited to date in the design and controlled preparation with designed architecture in forms of fiber, yarn, film and the 3D porous architecture of sponge, foam and aerogel, for application in flexible electronics leading toward smart wearable devices.[134-137]

c). Conducting polymer

Conducting polymers are of particular interest within a wide range of conducting materials because of their electrical and optical properties which are similar to those of metals or inorganic semiconductors. Thanks to the advantageous properties, such as facile synthesis, structural diversity and flexibility, light weight and cost-effectiveness, conducting polymers have offered great potential applications in emerging flexible electronics. Due to their conjugated *p*-electron system, conducting polymers possess

fascinating chemical and physical properties and their oxidation level is readily influenced by chemical and electrochemical doping/dedoping mechanisms, leading to a change of inherent conductivity.

Conducting polymers, including PANi, PPy, polythiophene (PTh), and PEDOT, with their structures shown in **Figure 1-3**, have attracted a great deal of interest in recent years. Due to their particular doping/dedoping behavior, conducting polymers have been widely used for electronic devices in batteries, supercapacitors, sensors and advanced flexible electronics.[138, 139] Various morphologies, including nanofibers, nanotubes, NWs, nanorods, nanorings and nanoarrays, have been reported by using oxidative polymerization, electrochemical polymerization and/or processing approaches such as seeding, soft-template-assisted and post-synthesis electrospinning. The availability of diverse conducting polymers provides great promise for preparing flexible energy storage devices. However, these devices generally present unsatisfactory cycle performance, induced by their volume change during the doping/dedoping process, resulting in poor electrochemical performance. These challenges can be resolved by rationally designing microstructures, optimizing the size of pores or channels and preparing conducting polymer composites.[138, 140, 141]
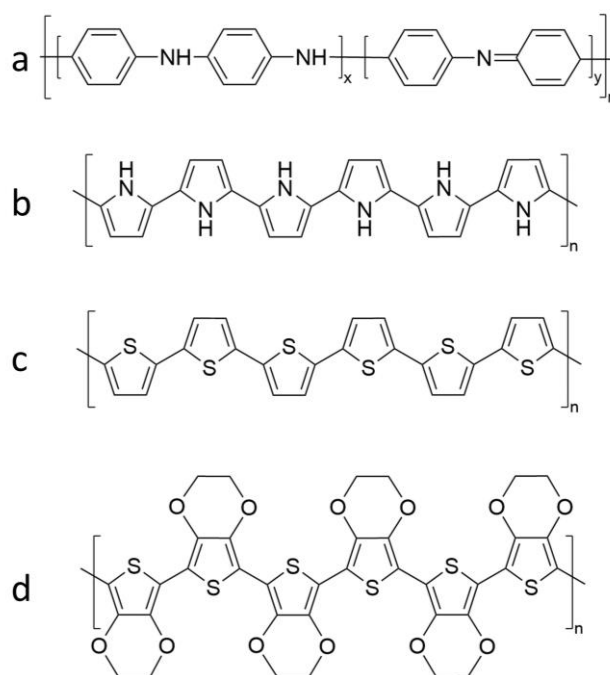
Figure 1-3. Chemical structure of (a) PANi ($x + y = 1$), (b) PPy, (c) PTh, and (d) PEDOT.

In addition, studies on conducting polymers have aimed to improve the conductivity and chemical stability of thin films for use in applications of flexible electronics. However, the conducting polymers have rarely been investigated on deformable electronics since they generate cracks when folded or stretched, leading to an irreversible reduction of conductivity. This drawback can be improved by blending plasticizers with numerous methods, including post-cast polymerization, purification, freeze-drying, re-dispersing, infiltration and curing, involved in the use of water-insoluble elastomers, such as PDMS and polyurethane (PU), and the blending of PEDOT:PSS dispersion with waterborne PU (WPU) constitute an easier and more effective way of making elastic composites while preserving the advantages of water-processability.[142-147] For example, a free-standing elastic highly conductive ($\sigma_{dc} > 140$ S cm^{-1}) and highly stretchable ($\varepsilon_f > 600$ %) PEDOT:PSS ionic liquid (IL)-WPU composites were obtained via solution casting of aqueous blends. The high conductivity and mechanical properties were attributed to the introduction of IL, because in comparison to the PEDOT:PSS-WPU composite without IL, the PEDOT:PSS-IL-WPU composites exhibit a 46-times larger elongation at break, a 35-times lower elastic modulus and are six orders of magnitude higher σ_{dc}.[148]

d). Other conducting materials

Except for fore mentioned materials and fabrications, the sputtering and evaporation of metals via shadow masks and photolithographic methods on soft substrates are another intensively used method to fabricate flexible circuits.[149] Metal oxides (i.e. indium tin oxide) are often used for optoelectronic applications because of their excellent conductivity and transparency, whereas they exhibit limited flexibility due to their brittle nature.[150] Nanoparticles blending with polymer matrices have been utilized to produce printable inks for the preparations of conductive circuits and patterns, addressing the brittle and conductivity challenges. These conductive inks can be processed to desirable conductive structures with various printing techniques, such as ink printing, melting printing and 3D printing technologies.[151-153] The emerging 2D materials, the thriving family of transition metal carbides, nitrides or carbonitrides (MXenes), standing out for their unique combination of metallic conductivity, solution

processability, high-aspect-ratio, and widely tunable properties, are also widely explored in soft electronics and are used in various forms from 1D fibers to 3D porous structures for a variety of applications including sensing, energy harvesting, electromagnetic interference (EMI) and optoelectronics.[154] Gallium-based liquid metals display remarkable conductivity, high thermal conductivity, high surface tension, excellent biocompatibility and adjustable adhesion. In addition to these prominent properties, liquid metal has a remarkable deformation ability, which offers novel strategies for innovation applications in soft machines and soft electronics.[155, 156]

1.3.2 Substrate materials

The current trend in flexible electronics aims to make these devices soft, bendable and even stretchable to achieve better mechanical conformability at the interface between electrical active material and substrates. Therefore, flexible electronics must possess the conformal integration of electrodes with curving matrices to accommodate various mechanical deformations in a dynamic environment.[157] To date, a variety of polymeric materials, such as poly(methyl methacrylate), polystyrene, polyacrylonitrile (PAN), polyimide (PI), poly(vinyl alcohol) (PVA) and poly(4-vinylphenol) have been applied as dielectrics and substrates in flexible electronics.[158] Polymeric substrates[159], such as parylene, and polyimide-based polymers have made vast progress in wearable/implantable electronics in recent decades. In addition, PIs are widely applied in electronics as mechanically and thermally robust insulators.[158] The PI used most extensively, Kapton (DuPont), strongly absorbs shorter visible wavelengths, endowing it a characteristic hue. Therefore, commercial PIs are not typically applied for transparent matrixes in light-emitting or soft display devices. Lab synthesized PIs were demonstrated to be suitable as a chemically, thermally and mechanically stable, substrate-cum-transparent electrode[160] or gate dielectrics[161] for flexible electronics. Moreover, the superior heat-resistant performance enables it to be applied in high-temperature plastic electronics.[162] However, the limited stretchable ability of PIs restricts their intensive applications in stretchable electronics.

Elastic substrates play a vital role in advanced stretchable wearable/implantable electronics. Silicon-based elastomers, such as PDMS, are attractive for stretchable electronics, especially due to cost-effectiveness, robustness, excellent flexibility, and chemically inert and feasible microfabrication techniques.[163, 164] Silicones provide desirable mechanical properties particularly for bioelectronics, including the tunable Young's modulus, high extensibility, and bulk hydrophobicity, making them continue to serve as the gold standard for substrates of bioelectronics because of additional outstanding biocompatibility.[163, 165]

Polyurethane is another favorable elastic polymer used as a substrate material for flexible electronics. Regarding diverse molecular constituents and structures, the appealing mechanical properties of PU, including prominent flexibility and superior elasticity, permit them excellent conformability when serving as substrates of wearable electronics, such as in e-skin and e-textile. Additionally, good solubility provides more feasible processing possibilities, such as coating, plastic shaping, electrospinning and various printing processes. Moreover, their diverse active functional groups endow plenty of novel properties. which endows PU with another appealing functionality as the substrate in wearable devices.[166, 167] For example, the side-chain quaternized PU exhibits excellent mechanical flexibility and additional antibacterial performance.

PVDF and its copolymers, as the most flexible piezoelectric polymer materials, have been intensively concerned and appealed as the research hotspot due to their excellent flexibility, strength, easy processing and low cost. The piezoelectric property of PVDF is attributed to the existence of polar crystalline phases, including β phase and γ phase, and its piezoelectric performance is majorly determined by the β phase because of its largest electric dipole moment among all crystalline phases.[168, 169] Thus, the PVDF containing a high amount of β phase is widely used in the development of high-performance devices, such as piezoelectric sensors, soft actuators and other flexible energy harvesters.[170]

In order to avert the decomposition issue by using traditional plastics, various biomaterials are chosen based on their mechanical properties, biocompatibility, biodegradability and eco-friendly features. PLA, polycaprolactone (PCL),

polydopamine, silk fiber, cellulose, and chitin are used in flexible electronics for improving the biocompatibility and progressing of eco-friendly development.[171] An organic transistor, for instance, based on a three-arm stereocomplex PLA as dielectric and substrate materials, is thermally stable up to 200 °C, and it polar groups of the dielectric are demonstrated to significantly enhance the temperature sensitivity of the device. The integrated skin-like temperature sensor array was successfully demonstrated based on such three-arm stereocomplex PLA transistors, which also exhibited good biocompatibility in cytotoxicity measurement.[172] These types of devices with combined advantages of transparency, flexibility, thermal stability, sensitive and fast response, crucial degradability and biocompatibility are highly promising for applications in flexible wearable/implantable electronics.

1.4 Fabrication strategies of nanofibrous flexible conductive systems

A variety of nanofibers, including polymeric, ceramic, carbon, metallic nanofibers, and inorganic composite nanofibers, have been increasingly applied in soft electronics for items such as flexible conductors, transparent electrodes, transistors, sensors, optoelectronics and energy devices. Accordingly, diverse methods have been developed to engineer electrospun nanofibers as passive components (e.g. functional substrates, precursors and templates) and active components (e.g. sensing layer for sensor, friction layer for nanogenerator, electrolyte separator for supercapacitor/battery) for flexible wearable devices.

Single electrospun semiconducting nanofibers exhibit good mechanical properties and high carrier mobility, thus have been applied as channel materials for flexible transistors. A large number of electrospun nanofibers, such as poly(3-decylthiophene)/poly (3-hexylthiophene) (P3HT) copolymer, P3HT, fused thiophene diketopyrrolopyrrole/PEO copolymer, and core-shell P3HT/PEO copolymer, have been currently reported to be fabricated into single nanofiber flexible transistors.[27, 173, 174] Compared to conventional filmwise semiconducting devices, single electrospun nanofiber from conjugated polymer present the following attractive features: (1) Larger contact area with a

dielectric layer, (2) better inherent flexibility, (3) easier patternability via direct printing technology, (4) the capability of engineered nanostructure for better responsiveness, and (5) more efficient and easier fabrication in scale-up.[175]

The micro/nanofiber manufactured by dry, force, melting and wet spinning methods have been widely investigated for e-textile application, but it is difficult to scale up production.[176] Consequently, various nanofiber bundles or yarn-shaped flexible conductors have been fabricated by electrospinning. Diverse conductive additives, such as graphene, CNTs, metal wires, and metal particles, are loaded in the fiber elements to obtain highly conductive yarns, which are generally utilized as highly sensitive strain and pressure sensors with a large working range.[177-180]

Apart from the single semiconducting nanofibers and yarns mentioned above, highly orientated nanofiber from conjugated polymers, which can be obtained by adjusting the spinning conditions regarding the molecular weight of the polymer used, the concentration of the spinning solution, flow rate and collector during the spinning process, have been employed as channel materials. In addition, highly aligned carbon nanofibers (CNFs) can be used to construct a stretchable multidirectional strain sensor via a facile, low-cost, and scalable electrospinning technique. The sensor prepared presented semitransparency, good stretchability of over 30%, outstanding durability for over 2500 cycles and an excellent anisotropic strain-sensing performance.[28]

In addition, electrospun nanofiber can be typically employed as temporary templates to fabricate transparent electrodes. The porous conductive mesh can be prepared by thermal decomposing or solvent dissolving to remove the nanofiber templates which tunes the properties by changing the parameters of the nanofibers used. Such mesh can be used for preparing transparent electrodes with both high transparency and high conductivity. Furthermore, a substrate-free, breathable, flexible, on-skin mesh-type conductor can be readily obtained by dissolving PVA nanofibers with a water mist after attachment.[181-183]

Flexible electronics devices are generally structured by embedding conductive elements into a film-type flexible matrix, such as PDMS, PI, poly(ethylene terephthalate), Ecoflex, parylene, latex rubber or paper, or by depositing conductive

elements onto them.[184, 185] However, the inherent mechanical mismatch between the polymeric matrix and employing electrical conductive elements will restrain their applications in wearable electronics for durable and continuous detection. The flexible substrates based on electrospun nanofibers, by contrast, can not only endow outstanding mechanical flexibility but also good breathability, greatly enhancing the wearing comfort of wearable devices.[181] The electrospun nanofibrous substrates, with their high pore volume and large surface area, are beneficial for loading a large amount of electrical additives, especially fitting for fabricating highly sensitive flexible devices.[186] The wearable devices derived from the electrospun membrane can be lightweight, breathable, flexible, conformable, highly sensitive and comfortable to wear. Someya recently reported a layer-by-layer structure of nanofiber/NW conductor which exhibited high conductivity (9190 S cm^{-1}), high stretchability (310 %), and good durability (82 % resistance increase after 1000 cycles of deformation at 70 % tensile strain). The good adhesion between the electrically active material and the nanofiber substrate enabled the as-prepared conductor to have excellent mechanical flexibility, indicating that it can be utilized as a breathable strain sensor for continuous electrophysiological signal recording.[187] The nonconductive electrospun nanofibrous membrane can typically serve as sensing-supporting, packaging layers in wearable devices, as well as be used as electrolytes and separators for batteries and insulating layers.[188, 189] Semiconducting nanofiber membranes are applied as channel materials in flexible transistors, friction layers in flexible nanogenerators and active layers in flexible sensors. Conducting nanofiber membranes are generally employed as active functional components in flexible conductors, electrodes, sensors and smart textiles.[175] The nanofiber nonwovens composed of short electrospun fibers by wet-laid method (also known as vacuum filtration) are more feasible in order to control the parameters, such as thickness, diameter, mechanical property, air permeability and homogeneity, and components to be fit for complicated applications, such as water treatment, energy storage devices, wearable devices and biomedical applications.[190-194] In order to achieve a conductive wet-laid sample, various additives including carbon fiber, carbon nanotube, graphene, nanoclay sheets, nanoparticles and NWs, are often integrated into

nonwovens. The weak mechanical property is also a disadvantage when perceived as a product. Therefore, postprocessing treatment, such as hot pressing or gluing, is necessary to enhance the mechanical stability of nonwovens. Researchers in a previous study fabricated a versatile electrical heater base on aramid short nanofibers and AgNWs by combining wet-laid and hot-pressing approaches. The resultant nanocomposite papers exhibited ultraflexibility, ultralow sheet resistance (minimum resistance of 0.12 Ω/sq), excellent thermal resistance, desirable mechanical properties, and fast electroheating performance, which are attributed to the partial embedding of AgNWs into the aramid short nanofiber substrate and the abundant hydrogen-bonding interactions, indicating their great promise for emerging smart wearable devices.[24] Another work was reported by our group: A flexible polymer nanofiber nonwoven of PAN, PCL and AgNWs with metal-like electrical conductivity was fabricated with a wet-laid and following hot-pressing approach. The superior conductivity of the nonwoven prepared was attributed to the dense AgNW percolation network and the length of the AgNWs.[195] Moreover, it is easy to manufacture multilayer membranes composed of diverse constituents and obtain property as desired. Flexible conductive Janus, Sandwich and multilayer membranes have been widely constructed for electronics applications by employing the wet-laid method.[24, 196-198]

Moreover, the conductive 3D monolithic structure (sponge/aerogel) assembled from short electrospun nanofibers represented an emerging research attraction in the flexible electronics field owing to its super-high porosity, excellent flexibility and structural stability. Inspired by conventional building blocks, such as graphene sheets and carbon nanotubes, to prepare functional aerogels, cut short electrospun nanofibers were reported in 2015 to construct the ultralight sponge (density < 3 mg cm^{-3}) with excellent uptake for hydrophobic liquid and cells growing successfully after hydrophilic modification, indicating a high potential in tissue engineering as a cell scaffold.[199] Since then, a variety of works on nanofibrous sponges have been developed and investigated leading to explosive growth, and especially in recent years attracted a lot of attention in different fields, such as biomedicine, pharmaceuticals, energy, environment and electronics, thanks to the 3D porous structure, ultralow density, high

surface area ratio, prominent flexibility and outstanding thermal properties.[200] Highly compressible, mechanically robust and highly conductive 3D sponge/aerogel can be constructed by using inherent conducting material (CNF or conducting polymer) or combining electrical elements (e.g. AgNWs, graphene, CNT, MXene), and is extensively applied in wearable devices.[115, 201-205] Owing to the large surface area, high porosity, excellent conductivity, high thermal/chemical stability and prominent mechanical properties, CNF sponges have been considered as the most promising candidate for supercapacitors, in which the interconnected porous architecture provides the continuous pathways for ions, greatly shortening the transport distance. Thus, they allow for fast electron transport. Thanks to the excellent conductivity and outstanding mechanical robustness, 3D porous and conducting materials, such as a conductive aerogel/sponge of CNT and graphene composites, have recently been investigated as pressure sensors. Their hierarchical pore structures process a wide range of size distribution from micro to macro scale, which is desirable for building sensors with a wide working range. In a recent study, PI-derived CNF aerogels exhibited high fatigue resistance, remarkable compressible flexibility and fast responsiveness to pressure, and demonstrated a promising application as a piezoresistive strain sensor.[206] In another study, a flexible triboelectric nanogenerator composed of highly porous cellulose nanofiber/polyethyleneimine aerogel film paired with polyvinylidene fluoride nanofiber mats shows remarkable triboelectric outputs, resulted in not only enhancing the mechanical properties but also improved the power density by 14.4 times due to the increase of tribopositivity.[207]

1.5 Application of fibrous flexible electronics

1.5.1 Mechanical sensor

Traditional electronic sensors, mostly based on metallic or semiconductor materials, are usually heavy and rigid, very limited in sensitivity and flexibility, and, thus, unsuitable for monitoring human physical signals. In comparison to traditional electronic sensors,

the emerging flexible wearable sensors have mostly overcome the problems and exhibited a variety of advantages, such as lightweight, prominent flexibility, good biocompatibility and real-time response, and are mostly applied to detect all kinds of human daily activities, such as joint movements, emotions, phonations and respirations, and other types of physiological signals such, as electromyography and electrocardiography.[133, 164, 169, 171, 208, 209]

The working mechanism of a mechanosensor function typically by converting a mechanical deformation into an electrical signal, divided into capacitive, resistive and piezoelectric types. Among them, the resistive type and capacitive type sensors are in favor of static measurements, intrinsically causing inconvenience to detect high-frequency movements, whereas which could be detected by a piezoelectric sensor.[210]

A typical capacitive sensor is constructed in a sandwich structure of a flexible dielectric central layer and with an electrically conductive layer on either side, serving as an electrode to transmit electrons (**Figure 1-4**). This kind of sensor generally has good strain-capacitance linearity, which could be expressed as the following equation:

$$C = \varepsilon_0 \varepsilon_r S / d \ (1),$$

where ε_0 denotes the vacuum dielectric constant, ε_r is the relative dielectric constant of the matrix, S represents the overlap region of the two electrodes, and d is the thickness of the matrix. When an external force is applied to a capacitive sensor, a variation of capacitance induced by mechanical deformation from a spatial change, reflected in the change of S or d, could be transferred into a real-time electrical signal, enabling the detection of external stimuli intensity. The void structure of the nanofiber membrane, an effective way to enhance sensitivity, is becoming more and more favored in capacitive pressure sensors. Thanks to the high porosity of the electrospun nanofiber membrane, when external pressure is applied, the membranes are easy to generate a compressive deformation, which leads to the decrease in the electrode distance of the sensor and increases the equivalent dielectric coefficient at the same time, thus the total capacitance will dramatically change.[211] For instance, a capacitive sensor consisting of electrospun PVDF nanofiber membrane displayed high sensitivity ~0.99 kPa^{-1}, fast response ~29 ms and outstanding cyclic stability.[212] This kind of sensor can be

integrated into a functional sensor array to detect the spatial distribution and the magnitude of tactile pressure, indicating a high potential for application in soft robotics and electronic skin.[31, 213]
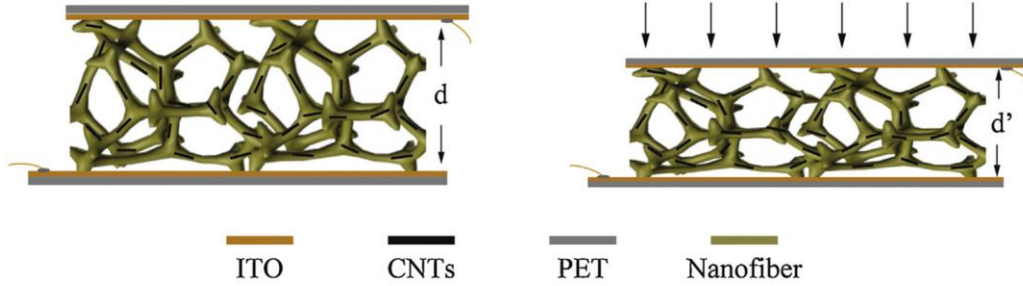
Figure 1-4. The schematic working mechanism of a strain-capacitance sensor. Reprinted with permission.[213] Copyright © 2019 Elsevier

A resistive sensor can convert external stress into an electrical signal, derived from resistance variation induced by structure deformation (**Figure 1-5**). The resistance formula of

$$R = \rho L/A \quad (2),$$

where ρ is the resistivity of the materials, and L and A are the length and the cross-section area of the materials, respectively, expresses the mechanism of a resistive-type sensor. Generally speaking, ρ is a constant at a constant temperature for most of the materials. Material deformations induced from external stress result in a change of L or A, causing the bulk resistance change, which enables the detection and conversion into visualizable electrical signals. The gauge factor (GF) is the ratio of relative change in electrical resistance to mechanical strain, which is a crucial factor to evaluate sensor except for sensitivity, defined as:

$$GF = \frac{\Delta R/R}{\Delta L/L} = \frac{\Delta R/R}{\varepsilon} = 1 + 2\nu + \frac{\Delta \rho/\rho}{\varepsilon} \quad (3),$$

where ΔR, R, ΔL, L, ε, ν, $\Delta \rho$ and ρ are resistance variation, resistance without applying strain, length variation, original length, strain, Poisson's ration, resistivity variation, and original resistivity, respectively, which is determined by the geometric effect of the materials $(1 + 2\nu)$ and the intrinsic factor $(\Delta \rho/\rho /\varepsilon)$. The Poisson's ratio of the polymer is usually between 0.35 and 0.5, so, the geometric contribution to GF

should be between 1.7 and 2. Therefore, a GF value less than 2 may be attributed to the geometric contribution, while a value greater than 2 may be due to the inherent resistivity change and the deformed strain of the composite. A large number of studies are being investigated currently regarding diverse kinds of sensors derived from electrospun nanofiber assemblies, including single fiber, yarn, membrane and 3D structures, which were utilized as strain/pressure sensors to monitor various physical movements, because of their specific advantages such as short response time, high sensitivity and low power consumption. By employing elastic polymer fiber as a substrate, such as the most often used TPU and PDMS, the sensors fabricated have great liner sensitivity and a large GF upon the strain applied. A TPU/NTs/AgNWs/PDMS strain sensor, for example, possessed a large GF of 1.36×10^5 and a wide working range of 38 to 100 %, demonstrating excellent sensing performance.[214] Conductive nanofibrous 3D structures (sponge, aerogel and foam) are generally used for pressure sensors due to their excellent elastic resilience and mechanical properties. They can be constructed directly from conductive fibers, such as carbon fiber, or by blending graphene, for example, carbon nanotube and AgNWs, conducting additives to obtain changeable conductivity upon applied pressure.[115, 215, 216]

A piezoelectric sensor is a device that uses the piezoelectric effect to measure changes in pressure, acceleration, temperature, strain, or force by converting them to an electrical potential. It presents advantages of high sensitivity and fast response to external stress. Once piezoelectric materials undergo stress, the neutrality of the charge in the crystals starts breaking, inducing an electric field across the material boundary. The electricity induced by stress can be reduced to the following function:

$$D_i = \varepsilon_0 \varepsilon_{ij}^{\sigma} E_i + d_{iJ} \sigma_j \quad (4),$$

$$\delta_I = S_{IJ}^E \sigma_J + d_{Ii} E_i \quad (5),$$

D , E , σ , δ , ε_0 , d , ε_σ and S^E represent the electric displacement, the electric field, the stress, the strain, the free-space electric permittivity, the piezoelectric coefficient, the electric relative permittivity and the mechanical compliance matrix, respectively. I, J, i and j are indices. D and E are (3×1) tensors for directional coordination, and σ and δ

are (6 × 1) tensors for stresses or strains. Since d_{31} and d_{33} are generally strong among piezoelectric coefficients, they are the most common elements to explain piezoelectric phenomena. The d_{33} is known as the longitudinal piezoelectric coefficient, which means that the electric polarization is aligned in the direction of the stress applied. The d_{31} is known as the transverse coefficient, which means that the electric polarization is aligned in the direction perpendicular to the stress applied.
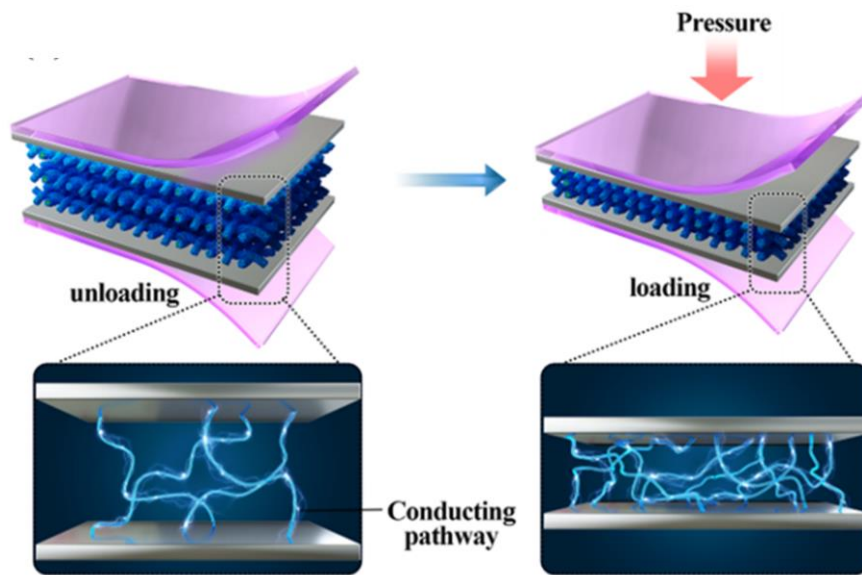
Figure 1-5. The schematic working mechanism of an ultrasensitive piezoresistive pressure sensor. Reprinted with permission.[217] Copyright © 2020, American Chemical Society

Piezoelectric inorganic materials have typically been used for sensor applications because of the strain-dependent charge change. However, they generally lack flexibility and are only suitable for the detection of small deformation less than 5 %, due to the features of piezoelectric materials. Organic polymer piezoelectric materials, such as PVDF and polytetrafluoroethylene, possess not only desirable flexibility, which enables to make up the fragile nature of inorganic materials, but also a simple fabrication process. Electrospun PVDF nanofibers have been intensively explored for piezoelectric sensors. The electrospinning method can generate polarize PVDF into β-phase with the highest polarization rate, avoiding the extra polarization process. Additionally, the high

porosity of nanofiber membranes fabricated by electrospinning makes them more favorable for pressure sensing devices, compared to film-type PVDF. By combining the traditional PET/indium-tin oxide composite electrode, PVDF nanofiber-based flexible piezoelectric sensors can possess high flexibility and sensitivity. The sensors can be utilized to detect quantitative pressure signals and monitor real-time human physical activities (**Figure 1-6**), such as joint bending, vocal vibration, and so on.[218]
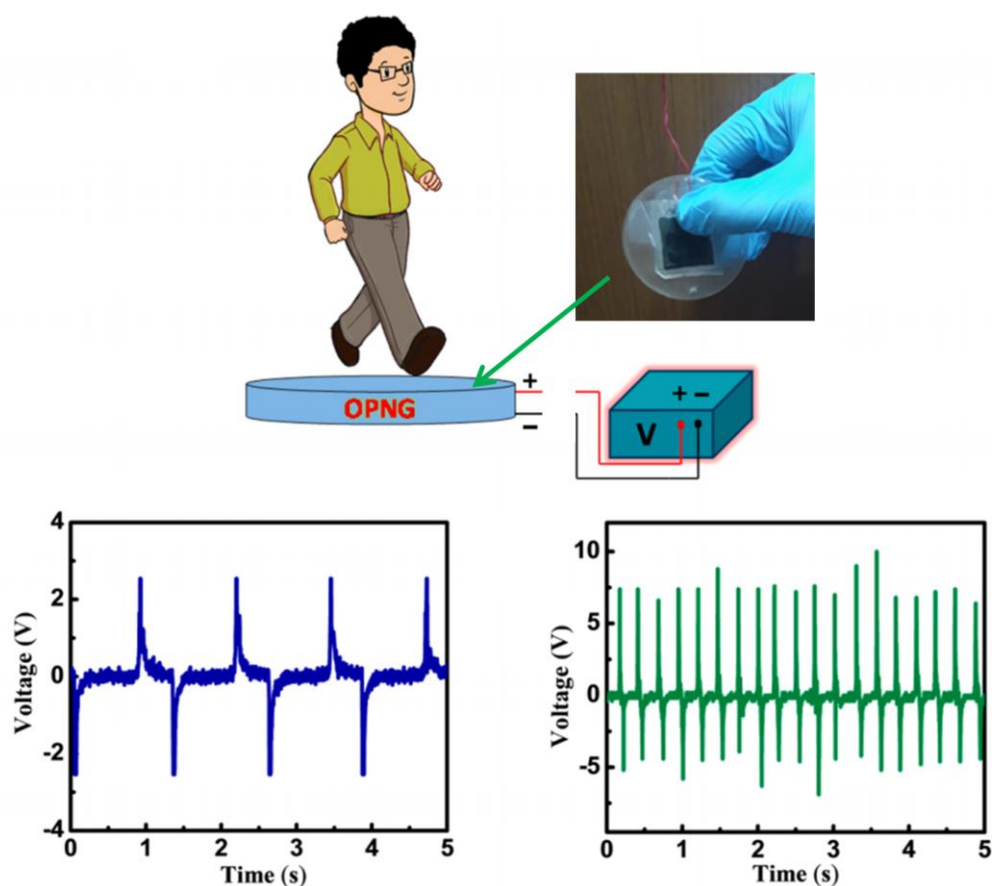
Figure 1-6. An all-organic high-performance piezoelectric sensor with multilayer assembled electrospun nanofiber mats. Reprinted with permission.[219] Copyright © 2018, American Chemical Society

Apart from the capacitive, piezoresistive and piezoelectric sensor, a transistor-based nanofibrous sensor is also demonstrated to be applied for biosignal detection. For example, a nanomesh sensor based on an organic electrochemical transistor (**Figure 1-7**) composed of electrospun nanofibers enables the device to be comfortably laminated

on human skin and simultaneously achieve local amplification. The maximum transconductance of the nanomesh organic electrochemical transistor can be controlled from 0.38 to 0.88 mS, with a fast response time of less than 1 ms, paving a way for on-skin electrodes that acquire high-quality biosignals.[220]
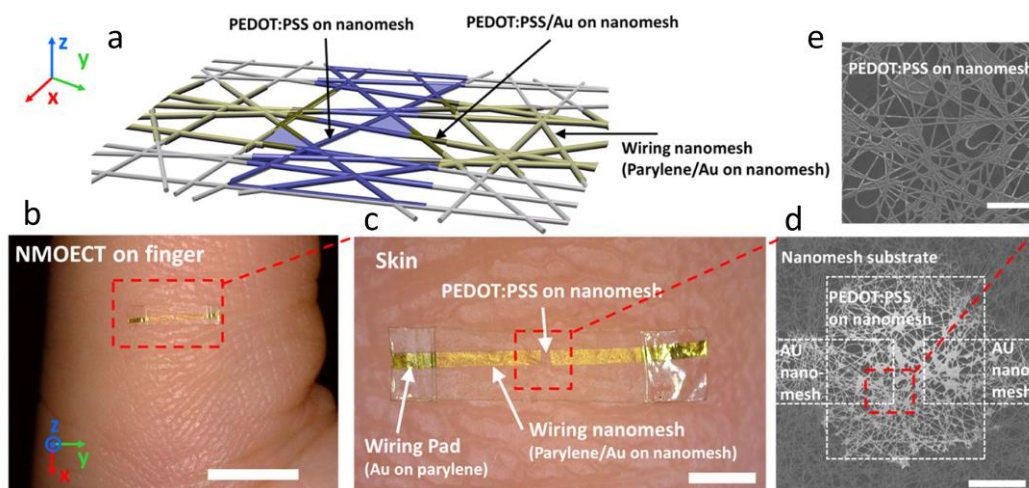
Figure 1-7. (a) Schematic of the nanomesh organic electrochemical transistor. (b) nanomesh organic electrochemical transistor laminated on the skin surface of a finger with a wiring Au pad on 2 μm-thick parylene film (scale bar: 5 mm). (c) Enlarged photo of nanomesh organic electrochemical transistor on the skin surface (scale bar: 1 mm). (d) Scanning electron microscopy (SEM) image of the channel part of the nanomesh organic electrochemical transistor (scale bar: 200 μm). (e) SEM image of PEDOT:PSS on the nanomesh (scale bar: 50 μm). Reprinted with permission[220]. Copyright © 2020 American Chemical Society

Polymer nanofibers have gained considerable attraction for sensors due to their desirable mechanical properties and flexibility, easy processing, lightweight, low cost and excellent sensing performance. Nanofibers for flexible sensing devices possess advantageous features compared to bulk samples. The active sensing components, for example, are typically embedded in the bulk, resulting in heavy and stiff performance, which restricts the flexibility, efficiency and sensitivity of the sensors. Nanofibers provide a high surface area which is beneficial for realizing highly flexible and sensitive sensors.[217, 219] Additionally, the nanofiber-based devices have demonstrated desirable

breathability, washability, durability and even attractive antibacterial property.[197, 221]

1.5.2 Wearable Joule heating device

The conventional thermos heating system consumes a vast amount of energy and is generally not portable due to the heavy weight and a lack of enough flexibility. Wearable Joule heating devices have been intensively investigated for balancing personal thermal management and thermal therapy.[222] The most important key parameter for high-performance Joule heaters is the value of resistance. A low resistance value ensures the heating device is enabled to generate considerable Joule heat to increase the temperature of substrates to a saturated value in economic energy input. Flexibility is also a crucial factor concerning the wearable heating device due to diverse deformations, such as stretching, folding and crumpling deformations, often faced during wearing. In addition, electrical and thermal stability under mechanical deformations is another essential criterion to be applied to next-generation wearable heating devices.[223]

An electrospun fiber membrane has a tunable pore size and porosity and outstanding flexibility, which displays advantageous features for wearable devices. Remarkable achievements based on fiber systems have been made in high-performance wearable joule heating devices so far by composing of conducting filler such as AgNW, graphene, CNT, carbon NP, MXene. The flexible TPU/ polydopamine/AgNW/MXene fibrous film, for example, has excellent Joule heating ability with a temperature up to 80 °C by applying a voltage of 1V, which could be applied for thermal therapy. Apart from the Joule heating function, the flexible TPU/polydopamine/AgNW/MXene fibrous mat displayed outstanding EMI shielding and highly sensitive resistance-deformation responses, without sacrificing its flexibility and permeability. Such a smart and wearable TPU/polydopamine/AgNW/MXene fibrous film is promising for application in high-performance electromagnetic wave protection, electrical therapy and human-machine interaction, especially for the protection of pregnant women.[224] Similarly, multilayered MXene/PLA membrane also achieved high EMI shielding performance

and fast joule heating function.[225]
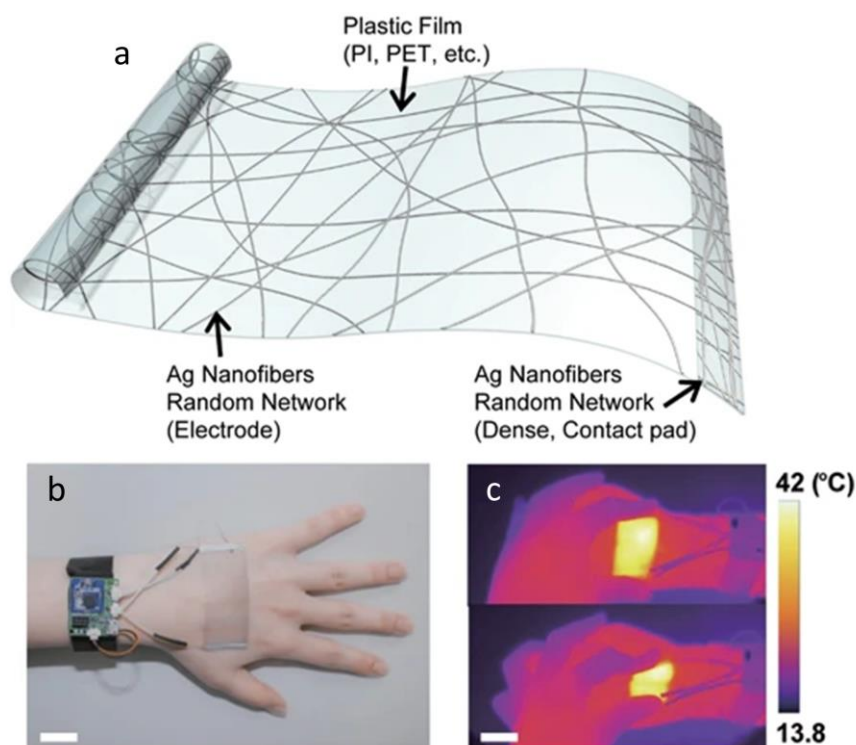
Figure 1-8. (a) Schematic illustration of the stretchable and transparent heater composed of an AgNF random network. (b) A photograph of the stretchable, wearable heater with a wristband-type wireless operation device. The scale bars represent 2 cm. (c) IR images of the stretchable wearable heater integrated with the wireless operating system. The scale bars represent 2 cm. Reprint with permission.[226] Copyright © 2017, The Author(s)

Electrospun nanofibers also serve as electrical conductive elements in wearable Joule heaters. Using electrospun ultra-long Ag nanofibers (AgNFs) constructed transparent heating electrodes (**Figure 1-8**) displayed low sheet resistance of ~ 1.3 Ω sq^{-1} and high optical transmittance of ~ 90%. Thanks to the low resistance, the resulting heater presented a remarkable power efficiency of 0.65 W cm^{-2} (with the temperature reaching 250 °C at a low DC voltage of 4.5 V) and demonstrated an ~10 times better performance than that of a conventional indium tin oxide-based heater.[226] Furthermore, the heater composed of ultra-long Cu nanofibers (CuNFs) via a coaxial electrospinning process demonstrated better performance on both resistance (0.8 Ω sq^{-1}) and transmittance

(~91 %). The CuNF heater generated a higher temperature of around 300 °C than that of an AgNF heater, and displayed a lifetime > 90 min at 800 °C under alternating current, indicating a promising advantage for next-generation wearable electronics.[227]

1.5.3 Flexible conductor

Flexible conductors are a critical constituent in soft electronics since they meet the requirement of undergoing various deformations happening in daily life. Thus, the basic features of a flexible conductor need to retain high conductivity under all kinds of mechanical deformations. Thanks to the outstanding mechanical strength and flexibility of electrospun nanofiber networks, a variety of studies have reported on flexible conductors based on electrospun fibers. The Someya group, for example, reported a simple and effective fabrication process to produce substrate-free on-skin electronics by using water dissolvable PVA nanofibers. The electrospun nanofiber networks with an Au layer of 70 – 100 nm in thickness were fabricated by deposition processing assisted by a shadow mask. By utilizing the treatment of spraying water mist, PVA nanofibers were completely removed and left Au networks attached to the skin, demonstrating a good conformable conductor due to its ultrathin network structure. Thanks to the porous network, the resultant substrate-free Au nanomeshes perform remarkable flexibility and breathability, which improved wearing comfort significantly without inducing rashes and other inflammatory skin reactions. Moreover, the Au nanomesh conductor exhibited excellent stretching durability, surviving under 10,000 cycles of finger bending in ~40 strain. On the other hand, electrospun nanofibers can be utilized as supporting materials. The AgNWs are often employed as a typical 1D conducting material to construct soft electronics because of their prominent inherent conductivity. The NWs/nanofibers composite conductors) present not only remarkable flexibility of the nanofiber membrane but also high conductivity, reaching even metal-level.[195, 228] The resultant nanofiber-based conductor, by using elastic polymer, such as PU fabricating electrospun nanofiber, exhibited outstanding stretchability in a large strain of > 300 %, high conductivity (9190 S cm^{-1}) and good durability (82 % resistance

increase after 1000 cycles of deformation at 70 % tensile strain). Except for AgNW, other conducting additives, such as graphene, carbon nanotube, carbon black, metal nanoparticle and metal NW, can be prepared directly by electrospinning.[229] It was found that the conductivity of the resulting nanofibrous assemblies can be increased by one to several orders of magnitude by removing the polymeric substrate of nanofibers.[230] Moreover, nanofibers derived from conductive polymers, such as PANi/PEO, PPy/PEO, pure PANi and PPy, poly(3- hexyl-thiophene)/PEO and PANi/PEO/CNTs, have been reported as applications for transistors, sensors and energy-relevant devices.

1.5.4 Other applications

Apart from applications mentioned above in the fields of mechanosensor, wearable Joule heating devices, conductors, other applications such as in optoelectronics, transistors, energy harvesting and storage devices[33, 231], organic artificial synapses[232], photodetectors, bio/chemical sensors[233], optical encoded sensors, EMI shielding materials[234] and soft actuators[235], have been investigated. By blending photosensitive semiconducting oxide materials, such as SnO_2, In_2O_3, CdS, CuO, WO_3, ZnTe, ZnS, $ZnGa_2O_4$, WS_2, ZnO and TiO_2–$ZnTiO_3$ and their heterostructures, the polymeric nanofibers enable one to obtain enhanced photoconductivity, which could be used as a flexible photoconductor with a vast range of applications in the ultraviolet and visible light regions in environmental and biological research, finger-print detection system, optical communication and the sensing field.[236-243]

1.6 Dissertation Objective

The aim of this dissertation is to develop advanced electric functional materials based on polymer fibers with advantageous features of lightweight, mechanically flexibility and excellent conductivity. In order to obtain both desirable flexibility and conductivity, novel structures are designed as dual-sided and sandwich-like film-type or 3D porous spongy structures by composing flexible polymer fibers and conductive additives.

Additionally, the certain structure endows the advanced conductive systems not only the excellent electric properties but also other unique mechanical, thermal, or optical properties, which are expected to be applied for emerging flexible electronics and wearable devices.

For this purpose, a dual-sided nonwoven with thermal regulating functionality is promising for personal body-temperature management. As a warm functional textile, the dual-sided nonwoven is expected to regulate temperature from both aspects, reducing body heat loss and compensating heat according to the requirement. PI electrospun nonwoven, providing outstanding mechanically flexibility and robustness, and thermal and chemical stability, is promising to be used as a substrate. AgNW is of high conductivity and ultralow emissivity, which is an ideal additive to construct the conductive system with heat function. Thus, to combine advantageous properties of PI and AgNW, a dual-sided structure will play a crucial role in the system. Additionally, if using elastic substrate (e.g. TPU nanofiber membrane) replaces PI nonwoven, a conductive system will be presented highly stretchable features and accompanied with mechanoresponsive conductivity, which is very interesting for the wearable strain sensor. In order to maintain the stability of the AgNW network during stretching, the encapsulation of a sandwich-like structure will provide desirable support to conductive AgNW networks from both sides, and a strong physical bond with hot-melt polymers will play a significant role to prevent the occurrence of delamination. Such a highly stretchable conductive system simultaneously with desirable mechanoresponsive conductivity can be used as a strain sensor for monitoring physical movements. Apart from the strain sensor, the piezoresistive sensor is also highly demanded using as a wearable device to detect diverse personal activities. Thus, aiming at developing highly compressible sponges with excellent piezoresistivity is a feasible strategy to realize this goal. Meanwhile, an additional heating feature will endow the sensor's multifunctionality, significantly broadening its applications. A strategy to fabricate such a promising sponge is to carbonize polymer nanofiber one. By incorporating GO nanosheets, the carbonized sponge simultaneously presented high compressibility and conductivity, based on which it can be utilized as a pressure sensor with heating

function.

In the subsequent section, a summary of the individual topics pertaining to this research and detailed experiments, analysis, results will be presented.

References

[1] S. Hong, S. Myung, Nat. Nanotechnol. **2007**, 2, 207.

[2] B. Wang, A. Facchetti, Adv. Mater. **2019**, 31, 1901408.

[3] X. Ni, W. Ouyang, H. Jeong, J. T. Kim, A. Tzaveils, A. Mirzazadeh, C. Wu, J. Y. Lee, M. Keller, C. K. Mummidisetty, Proc. Natl. Acad. Sci. U. S. A **2021**, 118.

[4] W. S. Wong, A. Salleo, Flexible electronics: materials and applications, Vol. 11, Springer Science & Business Media, **2009**.

[5] B. Wang, W. Huang, L. Chi, M. Al-Hashimi, T. J. Marks, A. Facchetti, Chem. Rev. **2018**, 118, 5690.

[6] Z. Bao, X. Chen, Wiley Online Library, **2016**.

[7] K. Sim, Z. Rao, H.-J. Kim, A. Thukral, H. Shim, C. Yu, Sci. Adv. **2019**, 5, eaav5749.

[8] C. Yu, C. Masarapu, J. Rong, B. Wei, H. Jiang, Adv. Mater. **2009**, 21, 4793.

[9] H.-J. Kim, K. Sim, A. Thukral, C. Yu, Sci. Adv. **2017**, 3, e1701114.

[10] D. Khim, Y. Xu, K. J. Baeg, M. Kang, W. T. Park, S. H. Lee, I. B. Kim, J. Kim, D. Y. Kim, C. Liu, Adv. Mater. **2016**, 28, 518.

[11] B. D. Choi, J. Park, K. J. Baeg, M. Kang, J. S. Heo, S. Kim, J. Won, S. Yu, K. Ahn, T. H. Lee, Adv. Electron. Mater. **2018**, 4, 1700386.

[12] S. Choi, J.-W. Jo, J. Kim, S. Song, J. Kim, S. K. Park, Y.-H. Kim, ACS Appl. Mater. Interfaces **2017**, 9, 26161.

[13] K. E. Petersen, C. Guarnieri, J. Appl. Phys. **1979**, 50, 6761.

[14] C. Pailler-Mattei, S. Bec, H. Zahouani, Med. Eng. Phys. **2008**, 30, 599.

[15] M. G. Walter, E. L. Warren, J. R. McKone, S. W. Boettcher, Q. Mi, E. A. Santori, N. S. Lewis, Chem. Rev. **2010**, 110, 6446.

[16] M. Zhou, X. W. D. Lou, Y. Xie, Nano Today **2013**, 8, 598.

[17] S. Peng, L. Li, J. K. Y. Lee, L. Tian, M. Srinivasan, S. Adams, S. Ramakrishna, Nano Energy **2016**, 22, 361.

[18] A. P. S. Sawhney, B. Condon, K. V. Singh, S.-S. Pang, G. Li, D. Hui, Text. Res. J. **2008**, 78, 731.

[19] A. K. Yetisen, H. Qu, A. Manbachi, H. Butt, M. R. Dokmeci, J. P. Hinestroza, M. Skorobogatiy, A. Khademhosseini, S. H. Yun, ACS Nano **2016**, 10, 3042.

[20] K. Cherenack, L. Van Pieterson, J. Appl. Phys. **2012**, 112, 091301.

[21] A. Chinnappan, C. Baskar, S. Baskar, G. Ratheesh, S. Ramakrishna, J. Mater. Chem. C **2017**, 5, 12657.

[22] W. Zeng, L. Shu, Q. Li, S. Chen, F. Wang, X. M. Tao, Adv. Mater. **2014**, 26, 5310.

[23] S. Wu, P. Liu, Y. Zhang, H. Zhang, X. Qin, Sens. Actuators B Chem. **2017**, 252, 697.

[24] Z. Ma, S. Kang, J. Ma, L. Shao, A. Wei, C. Liang, J. Gu, B. Yang, D. Dong, L. Wei, ACS Nano **2019**, 13, 7578.

[25] H. Jin, M. O. G. Nayeem, S. Lee, N. Matsuhisa, D. Inoue, T. Yokota, D. Hashizume, T. Someya, ACS Nano **2019**, 13, 7905.

[26] P. Prajongtat, C. Sriprachuabwong, R. Wongkanya, D. Dechtrirat, J. Sudchanham, N. Srisamran, W. Sangthong, P. Chuysinuan, A. Tuantranont, S. Hannongbua, ACS Appl. Mater. Interfaces **2019**, 11, 27677.

[27] J.-Y. Chen, H.-C. Hsieh, Y.-C. Chiu, W.-Y. Lee, C.-C. Hung, C.-C. Chueh, W.-C. Chen, J. Mater. Chem. C **2020**, 8, 873.

[28] J. H. Lee, J. Kim, D. Liu, F. Guo, X. Shen, Q. Zheng, S. Jeon, J. K. Kim, Adv. Funct. Mater. **2019**, 29, 1901623.

[29] L. Huang, J. Li, Y. Li, X. He, Y. Yuan, Nanoscale **2019**, 11, 8616.

[30] E. Ercan, P. Tsai, J. Chen, J. Lam, L. Hsu, C. Chueh, W. Chen, ACS Appl. Mater. Interfaces **2019**, 11, 23605.

[31] W. Yang, N. W. Li, S. Zhao, Z. Yuan, J. Wang, X. Du, B. Wang, R. Cao, X. Li, W. Xu, Adv. Mater. Technol. **2018**, 3, 1700241.

[32] D. N. Heo, H.-J. Kim, Y. J. Lee, M. Heo, S. J. Lee, D. Lee, S. H. Do, S. H. Lee, I. K. Kwon, ACS Nano **2017**, 11, 2961.

[33] B. Yu, H. Yu, H. Wang, Q. Zhang, M. Zhu, Nano Energy **2017**, 34, 69.

[34] Y. Fuh, L. Lien, Nanotechnology **2013**, 24, 055301.

[35] R. Amna, K. Ali, M. I. Malik, S. I. Shamsah.

[36] G. M. Bose, Recherches sur la cause et sur la veritable téorie de l'électricité, Slomac, **1745**.

[37] L. Rayleigh, London, Edinburgh Dublin Philos. Mag. J. Sci. **1882**, 14, 184.

[38] C. V. Boys, The London, Edinburgh, and Dublin Philosophical Magazine and Journal of Science **1887**, 23, 489.

[39] A. Formhals, US Patent **1934**, 1975504.

[40] B. Vonnegut, R. L. Neubauer, J. Colloid Sci. **1952**, 7, 616.

[41] G. I. Taylor, Proc. R. Soc. Lond., A Math. Phys. Sci. **1964**, 280, 383.

[42] P. K. Baumgarten, J. Colloid Interface Sci. **1971**, 36, 71.

[43] A. Greiner, J. H. Wendorff, Angew. Chem. Int. Ed. **2007**, 46, 5670.

[44] H. Fong, I. Chun, D. H. Reneker, Polymer **1999**, 40, 4585.

[45] D. H. Reneker, A. L. Yarin, H. Fong, S. Koombhongse, J. Appl. Phys. **2000**, 87, 4531.

[46] Y. Shin, M. Hohman, M. Brenner, G. Rutledge, Polymer **2001**, 42, 09955.

[47] A. L. Yarin, S. Koombhongse, D. H. Reneker, J. Appl. Phys. **2001**, 89, 3018.

[48] M. M. Hohman, M. Shin, G. Rutledge, M. P. Brenner, Phys. Fluids **2001**, 13, 2201.

[49] M. M. Hohman, M. Shin, G. Rutledge, M. P. Brenner, Phys. Fluids **2001**, 13, 2221.

[50] Y. Shin, M. Hohman, M. P. Brenner, G. Rutledge, Appl. Phys. Lett. **2001**, 78, 1149.

[51] G. Larsen, R. Velarde-Ortiz, K. Minchow, A. Barrero, I. G. Loscertales, J. Am. Chem. Soc. **2003**, 125, 1154.

[52] D. Li, Y. Wang, Y. Xia, Nano Lett. **2003**, 3, 1167.

[53] A. Theron, E. Zussman, A. Yarin, Nanotechnology **2001**, 12, 384.

[54] J. M. Deitzel, J. D. Kleinmeyer, J. K. Hirvonen, N. B. Tan, Polymer **2001**, 42, 8163.

[55] R. Dersch, T. Liu, A. Schaper, A. Greiner, J. H. Wendorff, J. Polym. Sci. A: Polym. Chem. **2003**, 41, 545.

[56] Z. Sun, E. Zussman, A. L. Yarin, J. H. Wendorff, A. Greiner, Adv. Mater. **2003**, 15, 1929.

[57] Polymeric Nanofibers, Copyright, Foreword. **2006**, 918, i-v. DOI: 10.1021/bk-2006-0918.fw001.

[58] D. H. Reneker, A. L. Yarin, Polymer **2008**, 49, 2387.

[59] H. Cho, S.-Y. Min, T.-W. Lee, Macromol. Mater. Eng. **2013**, 298, 475.

[60] J. F. Xu, Y. Z. Chen, D. Wu, L. Z. Wu, C. H. Tung, Q. Z. Yang, Angew. Chem. Int. Ed. **2013**, 125, 9920.

[61] W. Nuansing, E. Georgilis, T. V. de Oliveira, G. Charalambidis, A. Eleta, A. G. Coutsolelos, A. Mitraki, A. M. Bittner, Part. Part. Syst. Charact. **2014**, 31, 88.

[62] M. G. McKee, J. M. Layman, M. P. Cashion, T. E. Long, Science **2006**, 311, 353.

[63] A. Celebioglu, T. Uyar, Langmuir **2011**, 27, 6218.

[64] S.-S. Choi, S. G. Lee, S. S. Im, S. H. Kim, Y. L. Joo, J. Mater. Sci. Lett. **2003**, 22, 891.

[65] J. Geltmeyer, J. De Roo, F. Van den Broeck, J. C. Martins, K. De Buysser, K. De Clerck, J. Sol-Gel Sci. Technol. **2016**, 77, 453.

[66] J. E. Efome, D. Rana, T. Matsuura, C. Q. Lan, J. Mater. Chem. A **2018**, 6, 4550.

[67] C. Zhang, S. Yu, Chem. Soc. Rev. **2014**, 43, 4423.

[68] X. Lu, C. Wang, Y. Wei, Small **2009**, 5, 2349.

[69] C. L. Zhang, K. P. Lv, N. Y. Hu, L. Yu, X. F. Ren, S. L. Liu, S. H. Yu, Small **2012**, 8, 2936.

[70] X. Fan, B. Lv, Y. Xu, H. Huang, Y. Yang, Y. Wang, J. Xiao, C. Song, Solar Energy **2020**, 209, 325.

[71] Y. Jin, D. Yang, D. Kang, X. Jiang, Langmuir **2010**, 26, 1186.

[72] R. Ostermann, J. Cravillon, C. Weidmann, M. Wiebcke, B. M. Smarsly, Chem. Commun. **2011**, 47, 442.

[73] M. Rose, B. Böhringer, M. Jolly, R. Fischer, S. Kaskel, Adv. Eng. Mater. **2011**, 13, 356.

[74] R. Wang, C. Li, Q. Li, S. Zhang, Z. Yan, J. Chromatogr. A **2020**, 1622, 461098.

[75] G. S. Bisht, G. Canton, A. Mirsepassi, L. Kulinsky, S. Oh, D. Dunn-Rankin, M. J. Madou, Nano Lett. **2011**, 11, 1831.

[76] Y. Xin, D. H. Reneker, Polymer **2012**, 53, 4254.

[77] Y. S. Zheng, R. H. Gong, Y. C. Zeng, RSC Adv. **2015**, 5, 48533.

[78] G. Kim, Y. S. Cho, W. D. Kim, Eur. Polym. J. **2006**, 42, 2031.

[79] A. Varesano, R. A. Carletto, G. Mazzuchetti, J. Mater. Process. Technol. **2009**, 209, 5178.

[80] D. H. Sun, C. Chang, S. Li, L. W. Lin, Nano Lett. **2006**, 6, 839.

[81] N. M. Thoppey, J. R. Bochinski, L. I. Clarke, R. E. Gorga, Polymer **2010**, 51, 4928.

[82] J. S. Varabhas, G. G. Chase, D. H. Reneker, Polymer **2008**, 49, 4226.

[83] S. Agarwal, A. Greiner, J. H. Wendorff, Adv. Funct. Mater. **2009**, 19, 2863.

[84] Y. Dror, J. Kuhn, R. Avrahami, E. Zussman, Macromolecules **2008**, 41, 4187.

[85] S. Klein, J. Kuhn, R. Avrahami, S. Tarre, M. Beliavski, M. Green, E. Zussman,

Biomacromolecules **2009**, 10, 1751.

[86] J. P. F. Lagerwall, J. T. McCann, E. Formo, G. Scalia, Y. N. Xia, Chem. Commun. **2008**, 5420.

[87] L. Peng, S. H. Jiang, M. Seuss, A. Fery, G. Lang, T. Scheibel, S. Agarwal, Macromol. Mater. Eng. **2016**, 301, 48.

[88] X. M. Cai, P. Zhu, X. Z. Lu, Y. F. Liu, T. P. Lei, D. H. Sun, J. Mater. Sci. **2017**, 52, 14004.

[89] C. R. Yang, Z. D. Jia, J. N. Liu, Z. H. Xu, Z. C. Guan, L. M. Wang, IEEE Trans. Dielectr. Electr. Insul. **2009**, 16, 785.

[90] M. Sattary, M. Rafienia, M. T. Khorasani, H. Salehi, J. Biomed. Mater. Res. B **2019**, 107, 933.

[91] Y.-Z. Long, X. Yan, X.-X. Wang, J. Zhang, M. Yu, in Electrospinning: nanofabrication and applications, Elsevier, **2019**, 21.

[92] X. Liao, M. Dulle, J. M. D. E. Silva, R. B. Wehrspohn, S. Agarwal, S. Forster, H. Q. Hou, P. Smith, A. Greiner, Science **2019**, 366, 1376.

[93] E. Smit, U. Buttner, R. D. Sanderson, Polymer **2005**, 46, 2419.

[94] W. E. Teo, R. Gopal, R. Ramaseshan, K. Fujihara, S. Ramakrishna, Polymer **2007**, 48, 3400.

[95] L. Wang, Y. B. Wu, B. L. Guo, P. X. Ma, ACS Nano **2015**, 9, 9167.

[96] C. J. Luo, E. Stride, S. Stoyanov, E. Pelan, M. Edirisinghe, J. Polym. Res. **2011**, 18, 2515.

[97] I. Greenfeld, E. Zussman, J. Polym. Sci. B Polym. Phys. **2013**, 51, 1377.

[98] A. Stoiljkovic, S. Agarwal,   Macromol. Mater. Eng. **2008**, 293, 895.

[99] S. Jiang, G. Duan, J. Schöbel, S. Agarwal, A. Greiner, Compos. Sci. Technol. **2013**, 88, 57.

[100] S. Jiang, A. Greiner, S. Agarwal, Compos. Sci. Technol. **2013**, 87, 164.

[101] A. Omidinia-Anarkoli, S. Boesveld, U. Tuvshindorj, J. C. Rose, T. Haraszti, L. De Laporte, Small **2017**, 13, 1702207.

[102] O. Regev, C. S. Reddy, N. Nseir, E. Zussman, Macromol. Mater. Eng. **2013**, 298, 283.

[103] R. Ravichandran, J. R. Venugopal, S. Sundarrajan, S. Mukherjee, R. Sridhar, S. Ramakrishna, Nanotechnology **2012**, 23, 385102.

[104] S. Xu, C. Qin, M. Yu, R. Dong, X. Yan, H. Zhao, W. Han, H. Zhang, Y. Long, Nanoscale **2015**, 7, 12351.

[105] J. Ding, J. Zhang, J. Li, D. Li, C. Xiao, H. Xiao, H. Yang, X. Zhuang, X. Chen, Prog. Polym. Sci. **2019**, 90, 1.

[106] T. Wu, M. Ding, C. Shi, Y. Qiao, P. Wang, R. Qiao, X. Wang, J. Zhong, Chin. Chem. Lett.

2020, 31, 617.

[107] J. Xue, J. Song, Y. Dong, L. Xu, J. Li, H. Zeng, Sci. Bull. **2017**, 62, 143.

[108] D. Tan, C. Jiang, Q. Li, S. Bi, J. Song, J. Mater. Sci.: Mater. Electron. **2020**, 1.

[109] D. J. Finn, M. Lotya, J. N. Coleman, ACS Appl. Mater. Interfaces **2015**, 7, 9254.

[110] P. Yan, E. Brown, Q. Su, J. Li, J. Wang, C. Xu, C. Zhou, D. Lin, Small **2017**, 13, 1701756.

[111] J. Y. Oh, D. Lee, S. H. Hong, ACS Appl. Mater. Interfaces **2018**, 10, 21666.

[112] F. Qian, P. C. Lan, M. C. Freyman, W. Chen, T. Y. Kou, T. Y. Olson, C. Zhu, M. A. Worsley, E. B. Duoss, C. M. Spadaccini, T. Baumann, T. Y. J. Han, Nano Lett. **2017**, 17, 7171.

[113] C. Wu, L. Fang, X. Huang, P. Jiang, ACS Appl. Mater. Interfaces **2014**, 6, 21026.

[114] G. W. Huang, N. Li, Y. Liu, C. B. Qu, Q. P. Feng, H. M. Xiao, ACS Appl. Mater. Interfaces 2019, 11, 15028.

[115] S. H. Jiang, S. Reich, B. Uch, P. Hu, S. Agarwal, A. Greiner, ACS Appl. Mater. Interfaces **2017**, 9, 34286.

[116] J. H. Lee, P. Lee, D. Lee, S. S. Lee, S. H. Ko, Cryst. Growth Des. **2012**, 12, 5598.

[117] B. Li, S. Ye, I. E. Stewart, S. Alvarez, B. J. Wiley, Nano Lett. **2015**, 15, 6722.

[118] H. Zhai, R. Wang, X. Wang, Y. Cheng, L. Shi, J. Sun, Nano Res. **2016**, 9, 3924.

[119] Y. Ahn, Y. Jeong, D. Lee, Y. Lee, ACS Nano **2015**, 9, 3125.

[120] D. J. Joe, S. Kim, J. H. Park, D. Y. Park, H. E. Lee, T. H. Im, I. Choi, R. S. Ruoff, K. J. Lee, Adv. Mater. **2017**, 29, 1606586.

[121] S. Joo, S. Park, C. Moon, H. Kim, ACS Appl. Mater. Interfaces **2015**, 7, 5674.

[122] W. K. Kim, S. Lee, D. H. Lee, I. H. Park, J. S. Bae, T. W. Lee, J. Y. Kim, J. H. Park, Y. C. Cho, C. R. Cho, Sci. Rep. **2015**, 5, 1.

[123] Z. Li, S. Khuje, A. Chivate, Y. Huang, Y. Hu, L. An, Z. Shao, J. Wang, S. Chang, S. Ren, ACS Appl. Electron. Mater. **2020**, 2, 1867.

[124] X. Li, Y. Wang, C. Yin, Z. Yin, J. Mater. Chem. C **2020**, 8, 849.

[125] V. B. Nam, D. Lee, Nanomaterials **2016**, 6, 47.

[126] Q. Zhou, J. Kim, K. Han, S. Oh, S. Umrao, E. J. Chae, I. Oh, Nano Energy **2019**, 59, 120.

[127] A. Sánchez-Iglesias, B. Rivas-Murias, M. Grzelczak, J. Pérez-Juste, L. M. Liz-Marzán, F. Rivadulla, M. A. Correa-Duarte, Nano Lett. **2012**, 12, 6066.

[128] R. Saraf, H. Fan, V. Maheshwari, npj Flex. Electron. **2020**, 4, 1.

[129] C. M. Das, L. Kang, Q. Ouyang, K. T. Yong, InfoMat **2020**, 2, 698.

[130] Z. Wu, Y. Wang, X. Liu, C. Lv, Y. Li, D. Wei, Z. Liu, Adv. Mater. **2019**, 31, 1800716.

[131] K. Fu, Y. Yao, J. Dai, L. Hu, Adv. Mater. **2017**, 29, 1603486.

[132] M. Jian, C. Wang, Q. Wang, H. Wang, K. Xia, Z. Yin, M. Zhang, X. Liang, Y. Zhang, Sci. China Mater. **2017**, 60, 1026.

[133] C. Wang, K. Xia, H. Wang, X. Liang, Z. Yin, Y. Zhang, Adv. Mater. **2019**, 31, 1801072.

[134] Q. Fu, Y. Chen, M. Sorieul, ACS Nano **2020**, 14, 3528.

[135] Y. Gao, F. Guo, P. Cao, J. Liu, D. Li, J. Wu, N. Wang, Y. Su, Y. Zhao, ACS Nano **2020**, 14, 3442.

[136] X. Zang, R. Zhang, Z. Zhen, W. Lai, C. Yang, F. Kang, H. Zhu, Nano Energy **2017**, 40, 224.

[137] Z. Chen, H. Zhuo, Y. Hu, H. Lai, L. Liu, L. Zhong, X. Peng, Adv. Funct. Mater. **2020**, 30, 1910292.

[138] Y. Han, L. Dai, Macromol. Chem. Phys. **2019**, 220, 1800355.

[139] S. Meer, A. Kausar, T. Iqbal, Polym.-Plast. Technol. Mater. **2016**, 55, 1416.

[140] H. Yoon, J. Jang, Adv. Funct. Mater. **2009**, 19, 1567.

[141] J. Y. Oh, S. Kim, H. K. Baik, U. Jeong, Adv. Mater. **2016**, 28, 4455.

[142] T. S. Hansen, K. West, O. Hassager, N. B. Larsen, Adv. Funct .Mater. **2007**, 17, 3069.

[143] P. J. Taroni, G. Santagiuliana, K. Wan, P. Calado, M. Qiu, H. Zhang, N. M. Pugno, M. Palma, N. Stingelin-Stutzman, M. Heeney, Adv. Funct. Mater. **2018**, 28, 1704285.

[144] H. Kai, W. Suda, Y. Ogawa, K. Nagamine, M. Nishizawa, ACS Appl. Mater. Interfaces **2017**, 9, 19513.

[145] C. L. Choong, M. B. Shim, B. S. Lee, S. Jeon, D. S. Ko, T. H. Kang, J. Bae, S. H. Lee, K. E. Byun, J. Im, Adv. Mater. **2014**, 26, 3451.

[146] P. Li, D. Du, L. Guo, Y. Guo, J. Ouyang, J. Mater. Chem. C **2016**, 4, 6525.

[147] R. Zhou, P. Li, Z. Fan, D. Du, J. Ouyang, J. Mater. Chem. C **2017**, 5, 1544.

[148] N. Kim, S. Lienemann, I. Petsagkourakis, D. A. Mengistie, S. Kee, T. Ederth, V. Gueskine, P. Leclère, R. Lazzaroni, X. Crispin, K. Tybrandt, Nat. Commun. **2020**, 11, 1.

[149] E. Chen, W. Xu, J. Chen, J. Warner, Mater. Today Adv. **2020**, 7, 100076.

[150] M. Musztyfaga-Staszuk, Z. Starowicz, P. Panek, R. Socha, K. Gawlińska-Nęcek, "The influence of material parameters on optical and electrical properties of indium-tin oxide (ITO) layer",

presented at Journal of Physics: Conference Series, **2020**.

[151] S. G. Kirtania, M. A. Riheen, S. U. Kim, K. Sekhar, A. Wisniewska, P. K. Sekhar, Micromachines-Basel **2020**, 11, 841.

[152] W. Li, Q. Sun, L. Li, J. Jiu, X.-Y. Liu, M. Kanehara, T. Minari, K. Suganuma, Appl. Mater. Today **2020**, 18, 100451.

[153] D. Tsakona, I. Theodorakos, A. Kalaitzis, I. Zergioti, Appl. Surf. Sci. **2020**, 513, 145912.

[154] Y.-Z. Zhang, J. K. El-Demellawi, Q. Jiang, G. Ge, H. Liang, K. Lee, X. Dong, H. N. Alshareef, Chem. Soc. Rev. **2020**, 49, 7229.

[155] S. Chen, H. Wang, R. Zhao, W. Rao, J. Liu, Matter **2020**, 2, 1446.

[156] Y. Yu, J. Guo, B. Ma, D. Zhang, Y. Zhao, Sci. Bull. **2020**, 65, 1752.

[157] S. Wagner, S. Bauer, MRS Bull. **2012**, 37, 207.

[158] D. Ji, T. Li, W. Hu, H. Fuchs, Adv. Mater. **2019**, 31, 1806070.

[159] A. Malik, B. Kandasubramanian, Polym. Rev. **2018**, 58, 630.

[160] J. A. Spechler, T. W. Koh, J. T. Herb, B. P. Rand, C. B. Arnold, Adv. Funct. Mater. **2015**, 25, 7428.

[161] S. Park, H. Y. Chang, S. Rahimi, A. L. Lee, L. Tao, D. Akinwande, Adv. Electron. Mater. **2018**, 4, 1700043.

[162] A. Gumyusenge, X. Luo, Z. Ke, D. T. Tran, J. Mei, ACS Mater. Lett. **2019**, 1, 154.

[163] Q. Pang, D. Lou, S. Li, G. Wang, B. Qiao, S. Dong, L. Ma, C. Gao, Z. Wu, Adv. Sci. **2020**, 7, 1902673.

[164] D. Qi, K. Zhang, G. Tian, B. Jiang, Y. Huang, Adv. Mater. **2021**, 33, 2003155.

[165] T. A. Pham, T. K. Nguyen, R. K. Vadivelu, T. Dinh, A. Qamar, S. Yadav, Y. Yamauchi, J. A. Rogers, N. T. Nguyen, H. P. Phan, Adv. Funct. Mater. **2020**, 30, 2004655.

[166] P. Hu, A. Greiner, S. Agarwal, J. Polym. Sci. A Polym. Chem. **2019**, 57, 752.

[167] Y. Zhu, J. Hu, K.-W. Yeung, Acta Biomater. **2009**, 5, 3346.

[168] G. Zhu, Z. Zeng, L. Zhang, X. Yan, Comput. Mater. Sci. **2008**, 44, 224.

[169] X. Wang, F. Sun, G. Yin, Y. Wang, B. Liu, M. Dong, Sensors-Basel **2018**, 18, 330.

[170] L. Lu, W. Ding, J. Liu, B. Yang, Nano Energy 2020, 105251.

[171] Q. Sun, B. Qian, K. Uto, J. Chen, X. Liu, T. Minari, Biosens. Bioelectron. **2018**, 119, 237.

[172] X. Wu, Y. Ma, G. Zhang, Y. Chu, J. Du, Y. Zhang, Z. Li, Y. Duan, Z. Fan, J. Huang, Adv.

Funct. Mater. **2015**, 25, 2138.

[173] S. W. Lee, H. J. Lee, J. H. Choi, W. G. Koh, J. M. Myoung, J. H. Hur, J. J. Park, J. H. Cho, U. Jeong, Nano Lett. **2010**, 10, 347.

[174] A. Manuelli, L. Persano, D. Pisignano, Org. Electron. **2014**, 15, 1056.

[175] Y. Wang, T. Yokota, T. Someya, NPG Asia Mater. **2021**, 13, 1.

[176] M. Stoppa, A. Chiolerio, Sensors-Basel **2014**, 14, 11957.

[177] N. Nan, J. He, X. You, X. Sun, Y. Zhou, K. Qi, W. Shao, F. Liu, Y. Chu, B. Ding, Adv. Mater. Technol. **2019**, 4, 1800338.

[178] M. N. Shuakat, T. Lin, J. Nanosci. Nanotechno. **2014**, 14, 1389.

[179] E. Yang, Z. Xu, L. K. Chur, A. Behroozfar, M. Baniasadi, S. Moreno, J. Huang, J. Gilligan, M. Minary-Jolandan, ACS Appl. Mater. Interfaces **2017**, 9, 24220.

[180] K. Qi, Y. Zhou, K. Ou, Y. Dai, X. You, H. Wang, J. He, X. Qin, R. Wang, Carbon **2020**, 170, 464.

[181] A. Miyamoto, S. Lee, N. F. Cooray, S. Lee, M. Mori, N. Matsuhisa, H. Jin, L. Yoda, T. Yokota, A. Itoh, Nat. Nanotechnol. **2017**, 12, 907.

[182] H. Wu, D. Kong, Z. Ruan, P.-C. Hsu, S. Wang, Z. Yu, T. J. Carney, L. Hu, S. Fan, Y. Cui, Nat. Nanotechnol. **2013**, 8, 421.

[183] C. Okutani, T. Yokota, T. Someya, ACS Appl. Nano Mater. **2020**, 3, 1848.

[184] D. C. Kim, H. J. Shim, W. Lee, J. H. Koo, D. H. Kim, Adv. Mater. **2020**, 32, 1902743.

[185] W. Wu, Science and Technology of Adv. Mater. **2019**, 20, 187.

[186] W. Zhong, C. Liu, Q. Liu, L. Piao, H. Jiang, W. Wang, K. Liu, M. Li, G. Sun, D. Wang, ACS Appl. Mater. Interfaces **2018**, 10, 42706.

[187] Z. Jiang, M. O. G. Nayeem, K. Fukuda, S. Ding, H. Jin, T. Yokota, D. Inoue, D. Hashizume, T. Someya, Adv. Mater. **2019**, 31, 1903446.

[188] Z. Zhao, B. Li, L. Xu, Y. Qiao, F. Wang, Q. Xia, Z. Lu, Polymers-Basel 2018, 10, 575.

[189] M. Liu, N. Deng, J. Ju, L. Fan, L. Wang, Z. Li, H. Zhao, G. Yang, W. Kang, J. Yan, Adv. Funct. Mater. **2019**, 29, 1905467.

[190] R. R. Kisannagar, P. Jha, A. Navalkar, S. K. Maji, D. Gupta, ACS omega **2020**, 5, 10260.

[191] M. Fan, J. D. Jimenez, S. N. Shirodkar, J. Wu, S. Chen, L. Song, M. M. Royko, J. Zhang, H. Guo, J. Cui, ACS Catal. **2019**, 9, 10077.

[192] Y. Qi, K. B. Thapa, A. F. Hoadley, Chem. Eng. J. **2011**, 171, 373.

[193] S. Hube, M. Eskafi, K. F. Hrafnkelsdóttir, B. Bjarnadóttir, M. Á. Bjarnadóttir, S. Axelsdóttir, B. Wu, Sci. Total Environ. **2020**, 710, 136375.

[194] S. Noh, H. An, Y. Song, Cellulose **2021**, 28, 3081.

[195] S. Reich, M. Burgard, M. Langner, S. Jiang, X. Wang, S. Agarwal, B. Ding, J. Yu, A. Greiner, npj Flex. Electron. **2018**, 2, 1.

[196] C. Ma, W. Cao, W. Zhang, M. Ma, W. Sun, J. Zhang, F. Chen, Chem. Eng. J. **2021**, 403, 126438.

[197] X. Peng, K. Dong, C. Ye, Y. Jiang, S. Zhai, R. Cheng, D. Liu, X. Gao, J. Wang, Z. L. Wang, Sci. Adv. **2020**, 6, eaba9624.

[198] Y. Ko, D. Kim, U.-J. Kim, J. You, Carbohydr. Polym. **2017**, 173, 383.

[199] G. Duan, S. Jiang, V. Jérôme, J. H. Wendorff, A. Fathi, J. Uhm, V. Altstädt, M. Herling, J. Breu, R. Freitag, S. Agarwal, A. Greiner, Adv. Funct. Mater. **2015**, 25, 2850.

[200] T. Xu, Y. Ding, Z. Liang, H. Sun, F. Zheng, Z. Zhu, Y. Zhao, H. Fong, Prog. Mater. Sci. **2020**, 112, 100656.

[201] J. Huang, J. Zeng, B. Liang, J. Wu, T. Li, Q. Li, F. Feng, Q. Feng, M. J. Rood, Z. Yan, ACS Appl. Mater. Interfaces **2020**, 12, 16822.

[202] X. Wang, P. Liu, Q. Jiang, W. Zhou, J. Xu, J. Liu, Y. Jia, X. Duan, Y. Liu, Y. Du, ACS Appl. Mater. Interfaces **2018**, 11, 2408.

[203] J. Huang, D. Li, M. Zhao, H. Ke, A. Mensah, P. Lv, X. Tian, Q. Wei, Chem. Eng. J. **2019**, 373, 1357.

[204] K. Lu, J. Zhang, Y. Wang, J. Ma, B. Song, H. Ma, ACS Sustain. Chem. Eng. **2017**, 5, 821.

[205] Z. Saadatnia, S. Ghaffarimosanenzadeh, M. M. Chin, H. Naguib, M. R. Popovic, IEEE. Trans. Biomed. Eng. **2020**, 68, 1820.

[206] X. Hou, R. Zhang, D. Fang, Ceram. Int. **2020**, 46, 2122.

[207] H. Mi, X. Jing, Q. Zheng, L. Fang, H. Huang, L. Turng, S. Gong, Nano Energy **2018**, 48, 327.

[208] J. Lee, B. L. Zambrano, J. Woo, K. Yoon, T. Lee, Adv. Mater. **2019**, 32, 1902532.

[209] S. Y. Huang, Y. Liu, Y. Zhao, Z. F. Ren, C. F. Guo, Adv. Funct. Mater. **2019**, 29, 1805924.

[210] G. Tian, W. Deng, Y. Gao, D. Xiong, C. Yan, X. He, T. Yang, L. Jin, X. Chu, H. Zhang, W. Yan, W. Yang, Nano Energy **2019**, 59, 574.

[211] Y. Zhu, Y. Wu, G. Wang, Z. Wang, Q. Tan, L. Zhao, D. Wu, Org. Electron. **2020**, 84, 105759.

[212] H. Zhang, Q. Tang, Y. Chan, AIP Adv. **2012**, 2, 022112.

[213] X. Yang, Y. Wang, X. Qing, Sens. Actuator A Phys. **2019**, 299, 111579.

[214] L. Lin, Y. Choi, T. Chen, H. Kim, K. S. Lee, J. Kang, L. Lyu, J. Gao, Y. Piao, Chem. Eng. J. **2021**, 419, 129513.

[215] L. Wang, M. Zhang, B. Yang, J. Tan, X. Ding, ACS Nano **2020**, 14, 10633.

[216] X. Chen, H. Liu, Y. Zheng, Y. Zhai, X. Liu, C. Liu, L. Mi, Z. Guo, C. Shen, ACS Appl. Mater. Interfaces **2019**, 11, 42594.

[217] H. Pan, G. Z. Xie, W. Q. Pang, S. Wang, Y. Wang, Z. Jiang, X. S. Du, H. L. Tai, ACS Appl. Mater. Interfaces **2020**, 12, 38805.

[218] K. Maity, D. Mandal, ACS Appl. Mater. Interfaces **2018**, 10, 18257.

[219] G. Wang, T. Liu, X. Sun, P. Li, Y. Xu, J. Hua, Y. Yu, S. Li, Y. Dai, X. Song, Sens. Actuator A Phys. **2018**, 280, 319.

[220] J. Wang, S. Lee, T. Yokota, Y. Jimbo, Y. Wang, M. O. G. Nayeem, M. Nishinaka, T. Someya, ACS Appl.Electron. Mater. **2020**, 2, 3601.

[221] X. Guan, B. Xu, M. Wu, T. Jing, Y. Yang, Y. Gao, Nano Energy **2021**, 80, 105549.

[222] M. O. Faruk, A. Ahmed, M. A. Jalil, M. T. Islam, B. Adak, M. M. Hossain, S. Mukhopadhyay, Appl. Mater. Today **2021**, 23, 101025.

[223] P. Li, J. Ma, H. Xu, X. Xue, Y. Liu, J. Mater. Chem. C **2016**, 4, 3581.

[224] W. Zhai, C. Wang, S. Wang, J. Li, Y. Zhao, P. Zhan, K. Dai, G. Zheng, C. Liu, C. Shen, J. Mater. Chem. A **2021**, 9, 7238.

[225] Z. Du, K. Chen, Y. Zhang, Y. Wang, P. He, H.-Y. Mi, Y. Wang, C. Liu, C. Shen, Compos. Commun. **2021**, 26, 100770.

[226] J. Jang, B. G. Hyun, S. Ji, E. Cho, B. W. An, W. H. Cheong, J. U. Park, NPG Asia Mater. **2017**, 9, 432.

[227] S. Ji, J. Park, Y. Jo, Y. B. Kim, J. Jang, S. K. Kim, S. Jeong, J. U. Park, Appl. Surf. Sci. **2019**, 483, 1101.

[228] Z. Jiang, M. O. G. Nayeem, K. Fukuda, S. Ding, H. Jin, T. Yokota, D. Inoue, D. Hashizume, T. Someya, Adv. Mater. **2019**, 31, 1903446.

[229] S. Yao, Y. Zhu, Adv. Mater. **2015**, 27, 1480.

[230] R. Bagherzadeh, M. Gorji, M. S. Bafgi, N. Saveh-Shemshaki, in Electrospun nanofibers, Elsevier, **2017**, 467.

[231] C. Li, Y. Yin, B. Wang, T. Zhou, J. Wang, J. Luo, W. Tang, R. Cao, Z. Yuan, N. Li, ACS Nano **2017**, 11, 10439.

[232] Y. Lee, J. Y. Oh, W. Xu, O. Kim, T. R. Kim, J. Kang, Y. Kim, D. Son, J. B. H. Tok, M. J. Park, Sci. Adv. **2018**, 4, eaat7387.

[233] Y. Liu, M. Hao, Z. Chen, L. Liu, Y. Liu, W. Yang, S. Ramakrishna, Curr. Opin. Biomed. Eng. **2020**, 13, 174.

[234] H. Ji, R. Zhao, N. Zhang, C. Jin, X. Lu, C. Wang, NPG Asia Mater. **2018**, 10, 749.

[235] S. Sharafkhani, M. Kokabi, Compos. B. Eng. **2021**, 109060.

[236] J. Yao, H. Yan, C. M. Lieber, Nat. Nanotechnol. **2013**, 8, 329.

[237] F. X. Liang, J. Z. Wang, Z. P. Li, L. B. Luo, Adv. Opt. Mater. **2017**, 5, 1700081.

[238] C. Y. Nam, A. Stein, Adv. Opt. Mater. **2017**, 5, 1700807.

[239] S. J. Kim, J.-W. Han, B. Kim, M. Meyyappan, ACS sensors **2017**, 2, 1679.

[240] L. Peng, L. Hu, X. Fang, Adv. Mater. **2013**, 25, 5321.

[241] M. Shahid, J. Cheng, T. Li, M. A. Khan, Y. Wang, Y. Hu, M. Zhang, J. Yang, H. S. Aziz, C. Wan, J. Mater. Chem. C **2018**, 6, 6510.

[242] P. Feng, J. Zhang, Q. Wan, T. Wang, J. Appl. Phys. **2007**, 102, 074309.

[243] Z. He, Q. Liu, H. Hou, F. Gao, B. Tang, W. Yang, ACS Appl. Mater. Interfaces **2015**, 7, 10878.

2. An overview of the Dissertation
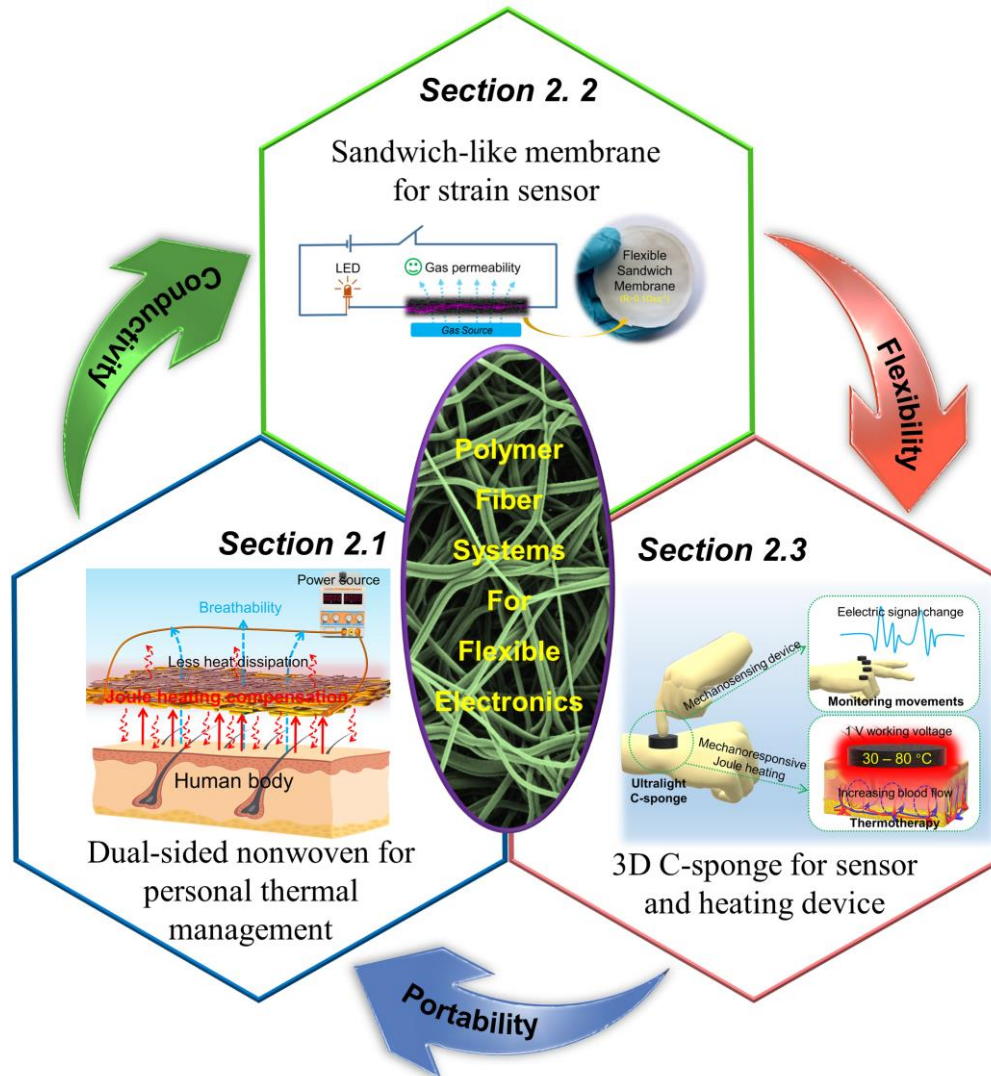
Figure 2-1. Context of this dissertation combining three subjects: (i) IR reflecting dual-sided nonwoven, (ii) stretchable sandwich-like membrane, (iii) mechanoresponsive 3D carbon sponge.

This dissertation contains two publications and one manuscript in **Section 2.1** to **2.3**. The context of this dissertation is exploring flexible conductive systems based on electrospun polymer fibers for flexible electronics, which are summarized in the above **Figure 2-1** and the following sections. The main contents involve the preparation of conductive systems, characterizations of their mechanical, electrical and thermal properties, and explorations of diverse applications for wearable devices.

In **section 2.1,** the flexible dual-sided nonwovens were fabricated with PI nanofiber nonwoven and AgNWs. The dual-sided nonwovens exhibited adjustable electric and optical properties by tuning the amount of AgNWs. A wearable thermal management device consisting of stacked double layer of dual-sided nonwovens demonstrated desirable body warming performance based on the thermal requirement. In addition, in **section 2.2,** the work explored a stretchable conductive system composed of elastics TPU nanofiber substrate and AgNWs with a sandwich-like structure, which indicated a great promise for wearable strain sensors. The last section (**Section 2.3**) aimed to construct ultralight sponges with mechanoresponsive features of electrical and thermal conductivities. The mechanoresponsive sponges were derived from PI/GO composite sponge by a carbonization process, which could significantly improve its electrical conductivity. Thanks to its excellent mechanical and electric properties, the conductive sponges could be applied as an advanced pressure sensor with intriguing warm functionality.

The details of each work will be displayed in the following section from **Section 2.1** to **2.3**.

2.1 Breathable and flexible dual-sided nonwovens with adjustable infrared optical performances for smart textile
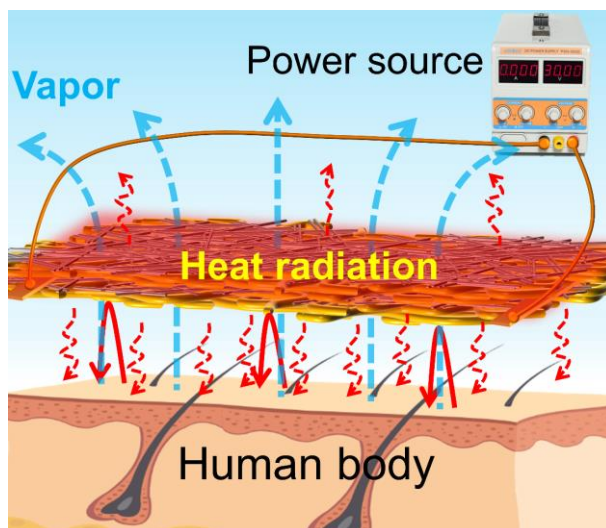
This work has been published in:

Q. Gao, T. Lauster, B. A. F. Kopera, M. Retsch, S. Agarwal, A. Greiner. Breathable and Flexible Dual-sided Nonwovens with Adjustable Infrared Optical Performances for Smart Textile. Adv. Funct. Mater. **2021**, 2108808.

Contribution list to the work:

Qiang Gao conducted the main parts of the work, including preparing the dual-sided nonwovens, characterizations of pore size, air permeability, mechanical property, most of the electrical properties and thermal properties, and discussed results. Qiang Gao also wrote the manuscript. Tobias Lauster measured and discussed emittance, transmittance, and reflectance, effusivity, and passive radiation. Bernd A. F. Kopera conducted some the characterization of AgNW's thermal stability, and IR reflection properties. Prof. Markus Retsch proposed and discussed experiments on radiative transport and thermography and revised the manuscript. Prof. Seema Agarwal gave many suggestions on conducting experiments and characterizations of the dual-sided nonwovens and revised manuscript. Prof. Andreas Greiner proposed and discussed the experiment scheme with Qiang Gao and revised the manuscript.

In this part of the work, a dual-sided nonwoven consisting of PI and AgNWs are designed for thermal management devices. The resultant membranes had dual sides (**Figure 2-2a**): the AgNW network side (silver gray) and the PI nanofiber layer side (yellow) (**Figure 2-2b**). TPU (blue regions in **Figure 2-2c**) physically linked AgNWs into a mesh and bonded them with the PI membrane, as confirmed by energy-dispersive X-ray-scanning electron microscopy (EDX-SEM) (**Figure 2-2d**). The dual-sided membranes were breathable and as strong as the pristine PI membrane (18 MPa in tensile strength, 77 % in strain) without any significant effect of TPU or AgNWs.

The sheet resistance of the dual-sided membranes could be tuned to as low as 0.2 Ω sq^{-1} using appropriate amounts of AgNWs (**Figure 2-2e**). In the circuit with PI/TPU/AgNW-500, there was insignificant variation in luminance of the lightening Light-emitting diode (LED) bulb with the membrane undergoing bending and twisting deformations (**Figure 2-2f**) compared to that of the virgin state. Additionally, the dual side membrane possessed high durability, cyclability to withstand non-tensile deformation and high thermal stability of resistance.

The dual-sided nonwoven demonstrated strong IR reflectance, which depended on the AgNW concentration, whereas the reflectance of PI is constant at ~30%. In the major range of human body radiation, a low emittance (~20%) on the AgNW side was observed, leading to less thermal losses. The pure PI electrospun nonwoven and the PI side of the dual-sided nonwoven showed higher emittance and are consequently expected to emit more radiation than the AgNW side, which was adverse to passive heating. The differences between pure PI and the PI side of the dual-sided nonwoven in the mid IR range (> 10 µm) have apparently no significant influence on the overall heat exchange. Therefore, the PI side facing towards skin (AgNW side facing towards outside) was the desirable wearing orientation.

The dual-sided nonwoven with less amount of AgNW (PI/TPU/AgNW-25) presented a rapid increase of the apparent surface temperature from room temperature to the equilibrium state within 5 seconds. The apparent temperature could even go as high as 230 °C on increasing the current to 0.37 A, indicating an excellent active heating performance.
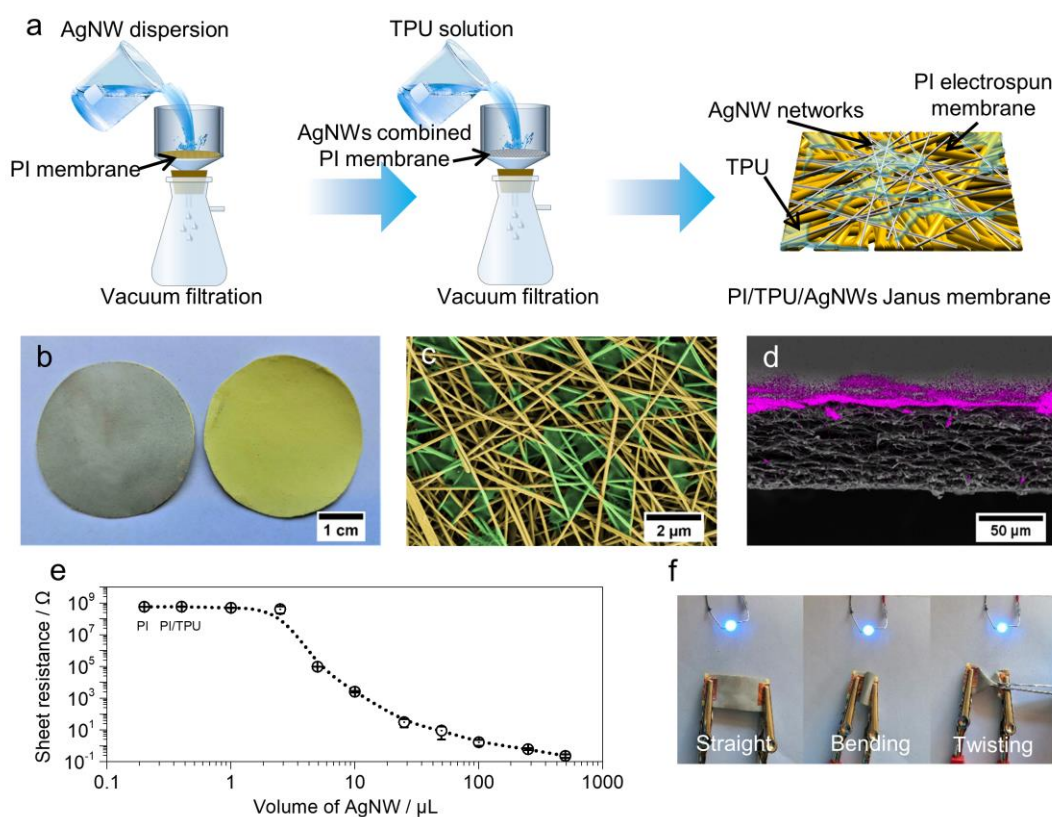
Figure 2-2. Preparation route (a) and (b) digital photographs of the dual-sided membrane (sliver gray: AgNW networks side, yellow: PI side). (c) Photoshop colored SEM image of AgNW networks with TPU: TPU colored in green. The Digital photograph of the AgNW water suspension was shown in the green frame at the left corner. (d) EDX-SEM image of the dual-sided membrane of PI/TPU/AgNW-500. The purple area presented the AgNW networks. (e) Sheet resistance of the dual-sided membranes prepared using different volumes of AgNW dispersion (17 g L^{-1}). PI and PI/TPU are labeled on the graphic without AgNWs for comparison. (f) The luminance of LED bulb under different deformations of the dual-sided membrane. Resistance change of PI/TPU/AgNW-25 and PI/TPU/AgNW-500 on repeated.

In order to take advantage of both active Joule heating and low radiation losses, we had integrated a nonwoven as a heating electrode (PI/TPU/AgNW-25) and another as a radiation insulator (PI/TPU/AgNW-500) in the form of a double layer. PI/TPU/AgNW-25 and PI/TPU/AgNW-500 stacked together act as a thermal management device for

heat compensation (**Figure 2-3a**). The PI side of the double layer was towards the skin. Already by applying 0.1A current the apparent temperature loss due to the low emissivity of the AgNW top layer is compensated (**Figure 2-3b**). As expected, the apparent surface temperature increases even further with a higher DC. This result indicated our thermal management device has a prominent heating function combining passive heating and active electric heating.
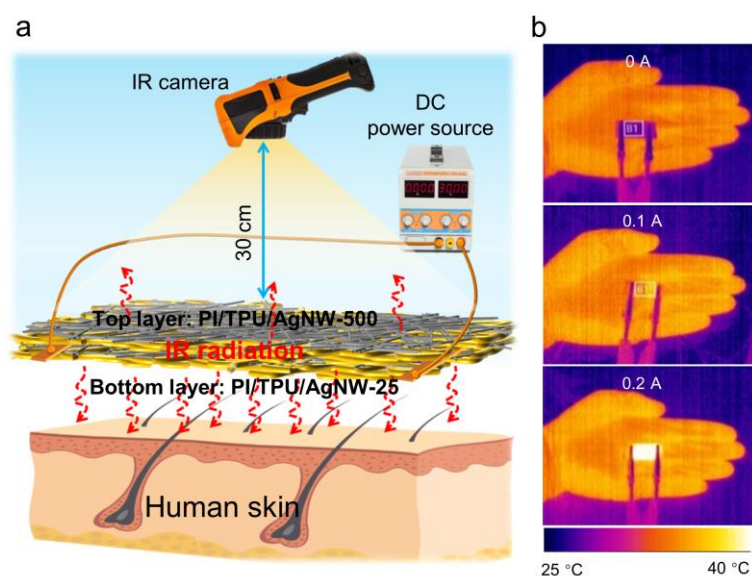
Figure 2-3. (a) Schematic diagram of the smart textile for thermal management. The smart textile was composed of PI/TPU/AgNW-500 (top layer), to reduce thermal emissivity, and PI/TPU/AgNW-25 (bottom layer), to exhibit substantial Joule heating. (b) Thermal images of the thermal management device by the applied different current.

In conclusion, we successfully prepared a breathable and flexible dual-sided nonwoven with tailored electrical and thermal properties that are promising as smart textiles for personal thermal management. The dual-sided nonwoven consisting of PI electrospun nonwoven and AgNW networks, presented significant differences of physical, electrical, and thermal properties on the two sides, which could be tailored by using the amount of AgNW. More AgNW was prone to form dense AgNW networks, which possessed very low electrical resistance of 0.23 Ω sq^{-1} and excellent IR reflectance of more than 80%, far higher than the normal textiles. The dual-sided nonwoven with the

AgNW facing to the outside demonstrated a desirable effect for a contribution to passive warming. It could be integrated into a thermal management device by applying low current, realizing both functions of reducing heat dissipation to the ambient environment and Joule heating to the human body. Besides, the dual-sided nonwoven showed outstanding flexibility under different deformations as well as washing stability without sacrificing electrical resistance. Such a dual-sided nonwoven can be used as a multifunctional flexible conductor and personal thermal management device to keep warm or smart textile escaping IR detection, which is very promising for next-generation wearable devices.

2.2 Breathable and flexible polymer membranes with mechanoresponsive electric resistance
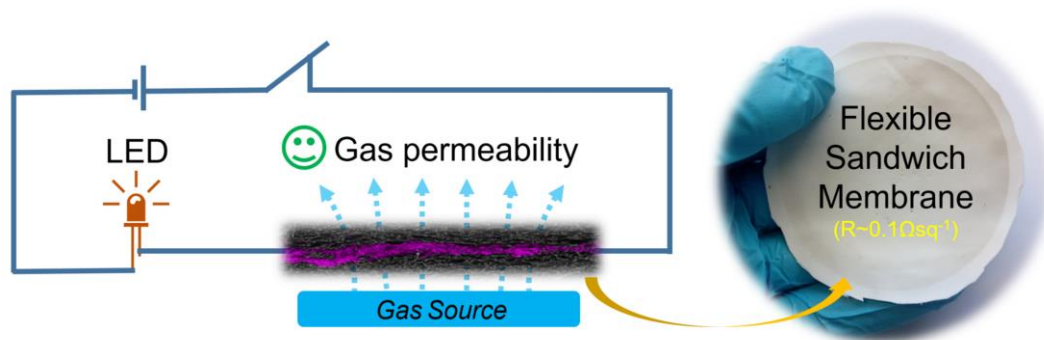
This work has been published in:

Contribution list to the work:

Qiang Gao conducted the main parts of the work, including preparing the sandwich membrane, characterizations of pore size, air permeability, mechanical property, most of the electrical properties, and discussed results. Qiang Gao also wrote the manuscript. Bernd A. F. Kopera conducted thermal diffusivity experiments, anisotropic analysis of stretching membrane and discussed the results. Jian Zhu took SEM images and discussed the results. Xiaojian Liao assisted with the mechanical test of the sample and discussed the results together with Qiang Gao. Prof. Chao Gao revised the manuscript. Prof. Markus Retsch proposed and discussed experiments on thermal diffusivity, anisotropic analysis, stretching thermography and revised the manuscript. Prof. Seema Agarwal provided suggestions on conducting experiments and characterizations of the sandwich membrane and revised manuscript. Prof. Andreas Greiner proposed and discussed the experiment scheme with Qiang Gao and revised the manuscript.

In this section, we aim to fabricate stretchable and breathable electrically conductive membranes composed of electrospun TPU fibrous membrane and AgNWs, which enables be applied for strain sensors to monitor body physical activities. As illustrated in **Figure 2-4a**, first, we prepared TPU nanofiber nonwovens via electrospinning. The TPU nonwovens consist of randomly oriented fibers. We then used the porous TPU membranes as a filter for the filtration of AgNWs mixed with a PCL short-fiber dispersion. After filtration, the AgNWs and short PCL fibers generated a double network-type structure due to percolation. Afterward, we covered the AgNW/ PCL layer with another layer of TPU nonwoven by electrospinning. Finally, we hot-pressed the three-layer stack at 75 °C for 30 min to melt the PCL and increase the adhesion of the layers. PCL short fibers served as the role of glue to provide good adhesion between the AgNW networks and the TPU layers (**Figure 2-4b**). The as-resulted membranes were constructed of two layers of TPU membrane outside and conductive AgNW layer inside, presenting a typical sandwich structure, which was demonstrated by SEM-EDX image (**Figure 2-4c**).

The sandwich membranes with different amount of AgNWs had excellent stretchability, which could be stretched to over 700% (**Figure 2-5a**). They can tolerate considerable strains with a moderate increase in resistance depending upon the amount of AgNWs. The sample with the highest content of AgNWs (TPU-2.0AgNW/PCL-TPU; 8.5 wt%) changed its resistance by only two orders of magnitude at a strain of ≈150%. In contrast, the sample with the fewest AgNWs (TPU-0.25AgNW/ PCL-TPU; 1.2 wt%) showed a comparable increase in resistance already at a strain of only 60%. The network was sparse due to fewer AgNWs in TPU-0.25AgNW/PCL, which led to a higher initial sheet resistance and a stronger increase in resistance during stretching. This resistance change introduced by the cracks generated from stretching deformation, resulted in an island-like fashion (**Figure 2-5b**) which caused a significant increase in resistance. The separated islands and cracks restricted the flow of electricity and in turn created hot spots by joule heating at the bottlenecks. The hotspots shifted with increasing strain and highlight the dynamic changes within the AgNW network upon stretching.
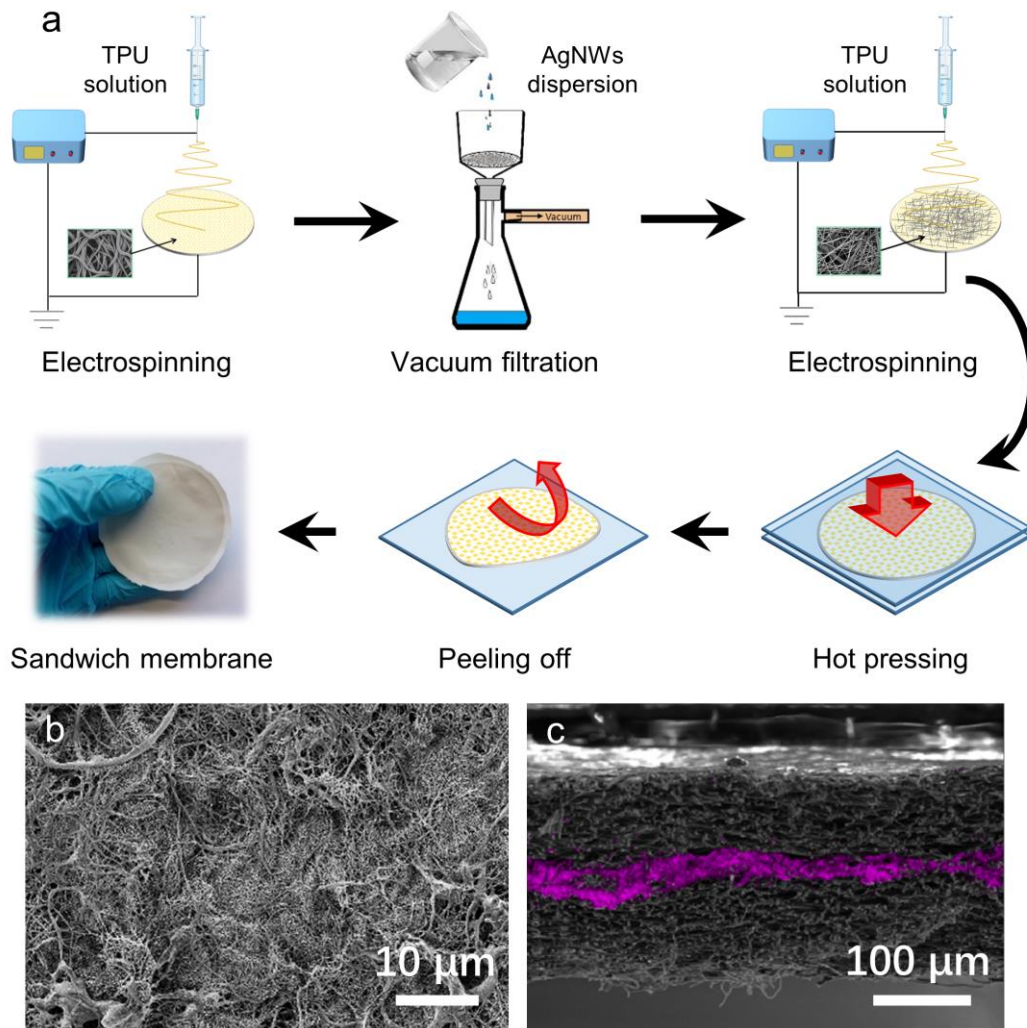
Figure 2-4. Schematic of preparing the TPU-AgNW/PCL-TPU membrane by sandwiching a network of AgNWs between TPU layers. (b) SEM image of the electrospun TPU nonwoven layered with AgNWs and PCL after heating. (c) Cross-section of EDX overlapped SEM image of as-prepared sandwich membrane of TPU-AgNW/PCL-TPU with PCL short fibers.

The sandwich membrane also presented some degree of anisotropy evolves by stretching, which leads to a thermal diffusivity decreases compared to the unstretched state, due to the decrease in electronic thermal conductivity in the AgNW layer. Additionally, an evolution of anisotropic heat spreading was observed in sandwich membrane.

The membranes, even with very high amounts of AgNWs (TPU-2.0AgNW/PCL-TPU), showed excellent stretchability and bending stability. The samples were subjected to

100 cycles of stretching and bending. The RC of TPU-0.25AgNW/PCL-TPU with only 1.2 wt% of AgNWs significantly increased after only 60 stretching cycles, the RC was >20 000 under 50% strain. However, the same sample showed much better bending stability (bending curvature from 0° to 150°) without a significant change in resistance. The RC of TPU-0.25AgNW/PCL-TPU after 100 bending cycles was merely 1.32. The sample TPU-2.0AgNW/PCL-TPU with a dense network of AgNWs showed both excellent bending and stretching stability. No significant change in the RC was observed for bending tests. During strain testing RC increased by only a factor of ≈20 after 100 cycles. An LED was utilized to demonstrate the flexibility of the prepared sandwich membrane under various mechanical loads during working conditions. TPU-0.25AgNW/PCL-TPU was connected to a circuit, as shown in Figure 2-5c, and was bent and twisted. The LED maintained almost the same brightness. However, after 50% strain stretching, the brightness of the LED could hardly be observed. This behavior corroborates the formation of a very high RC of TPU-0.25AgNW/PCL-TPU after stretching. When using a more highly concentrated AgNW network (TPU-2.0AgNW/PCL-TPU) twisting, bending, and stretching (50% strain) are tolerated and the brightness of the LED remained almost unchanged.

In conclusion, we proposed a new strategy to fabricate sandwichlike electrically conductive membranes with very low electric resistance. Our material consists of an AgNW network sandwiched between two porous electrospun TPU nonwovens. PCL short fibers act as glue and provide a strong interface between the three layers. Our membranes showed good bending and stretching stability, high stretchability (breaking elongation more than 700%) and very low initial electric resistance, as low as <0.1 Ω sq−1 depending upon the amount of AgNWs. This composite structure shows potential for use as a strain sensor to monitor body movement. Additionally, the membrane possessed gas permeability and low thermal diffusivity. Furthermore, our material has the potential to be integrated into smart wearable devices to collect body movement signals using a connected personal computer or mobile phone in the future.
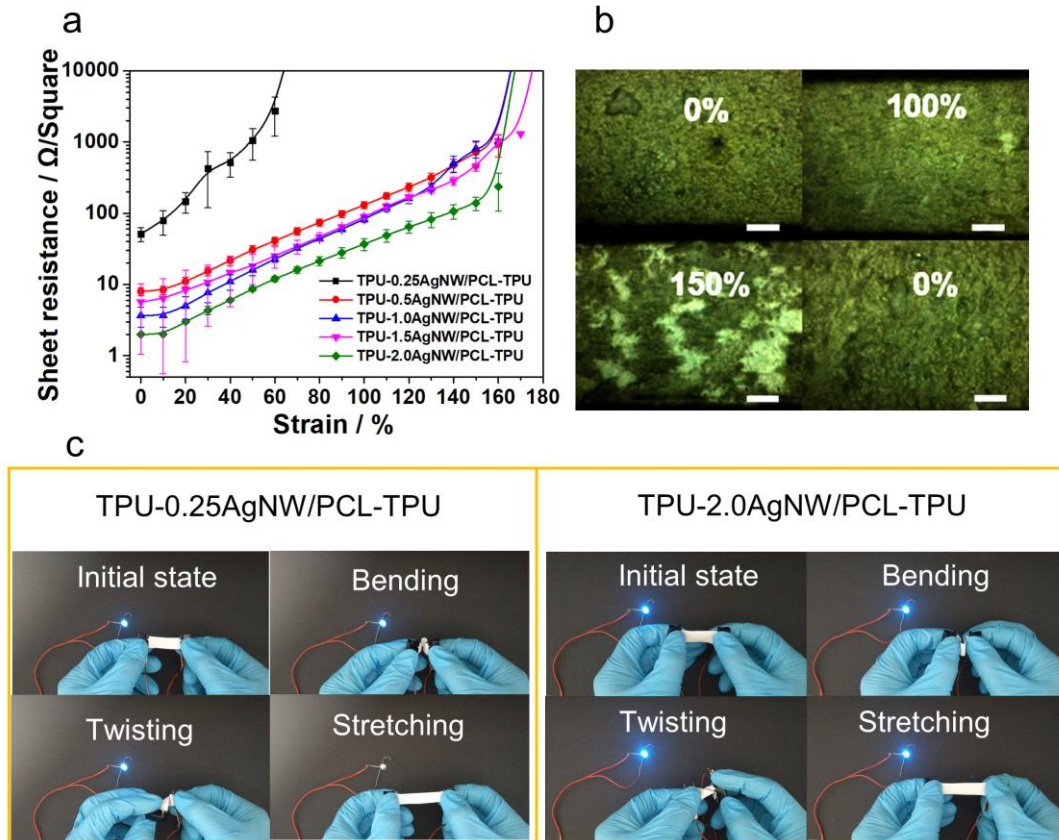
Figure 2-5. (a) Resistance of sandwich membranes with different amounts of AgNWs with different strains. (b) Optical images of TPU-2.0AgNW/PCL under different stains. Note the appearance of white spots at 150% strain due to cracks in the AgNW layer. (scale bar: 500 μm) d) EDX-SEM image of TPU-2.0AgNW/PCL at 100% strain. (scale bar: 50 μm) Ag is indicated in purple. (c) Digital image of LED brightness by different operation of nonwoven TPU-0.25AgNW/PCL-TPU and TPU-2.0AgNW/PCL-TPU.

2.3 Ultralight heat-insulating, electrically conductive carbon fibrous sponges for wearable mechanosensing devices with advanced warming function.
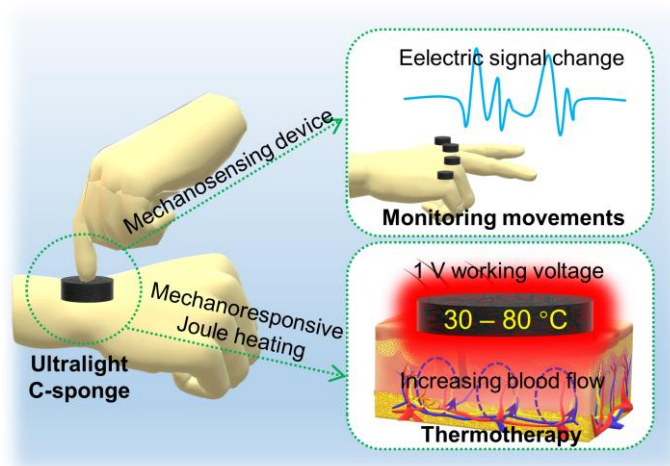
This work has been submitted to **ACS Applied Materials & Interfaces**.

Q. Gao, T. Tran ,X. Liao, S. Rosenfeldt, C. Gao, H. Hou, M. Retsch, S. Agarwal, A. Greiner. Ultralight heat-insulating, electrically conductive carbon fibrous sponges for wearable mechanosensing devices with advanced warming function.

Contribution list to the work:

Qiang Gao conducted the main parts of the work, including preparing the sponges, characterizations of chemical, physical, electrical properties and thermal properties, analysis of results, and drafting the manuscript. Thomas Tran measured the real-time resistance in the sensing application together with Qiang Gao and discuss the results. Dr. Xiaojian Liao conducted the carbonization of sponge, EDS-SEM measurement, discussed results of physical and chemical characterizations and manuscript. Dr. Sabine Rosenfeldt conducted XRD, XPS, SAXS characterizations, discussed the results and manuscript. Prof. Haoqing Hou and Prof. Chao Gao revised the manuscript. Prof. Markus Retsch discussed the sensing part and revised the manuscript. Prof. Seema Agarwal provided many suggestions on characterizations of the work and revised manuscript. Prof. Andreas Greiner proposed and discussed the experiment scheme with Qiang Gao and revised the manuscript.

In this section, a mechanically flexible and robust nanofibrous carbon sponge (NCS) derived from GO coated PI sponge are explored for pressure sensors. We enhance its mechanoresposive conductivity by pyrolyzing treatment with a high temperature. The procedure starts with the preparation of short electrospun PI fibers by mechanical cutting of long as-spun fibers followed by coating with GO, freeze-drying and carbonization. Since the surfaces of GO and PI are both negatively charged, an intermediate step of modifying the surface of PI short fibers with cationic PU is carried out to get a strong interface between PI and GO and subsequently a homogenous GO coating (**Figure 2-6a**). The transmission electron microscopy (TEM) (**Figure 2-6b**) and SEM (**Figure 2-6c**) investigations of the surface layer of GO coated fibers revealed a rough surface due to immobilized GO nanosheets. After thermal treatment, the surface of PIPUGO fibers exhibited even more wrinkles (**Figure 2-6d**). The NCS presented typical black color (**Figure 2-6a**) of carbon materials and showed shrinkage of ~ 14.6% in volume. In addition, the NCS with high porosity of 99.7% showed typical cellular porous structure and homogeneous graphene coating on the surface of fibers.
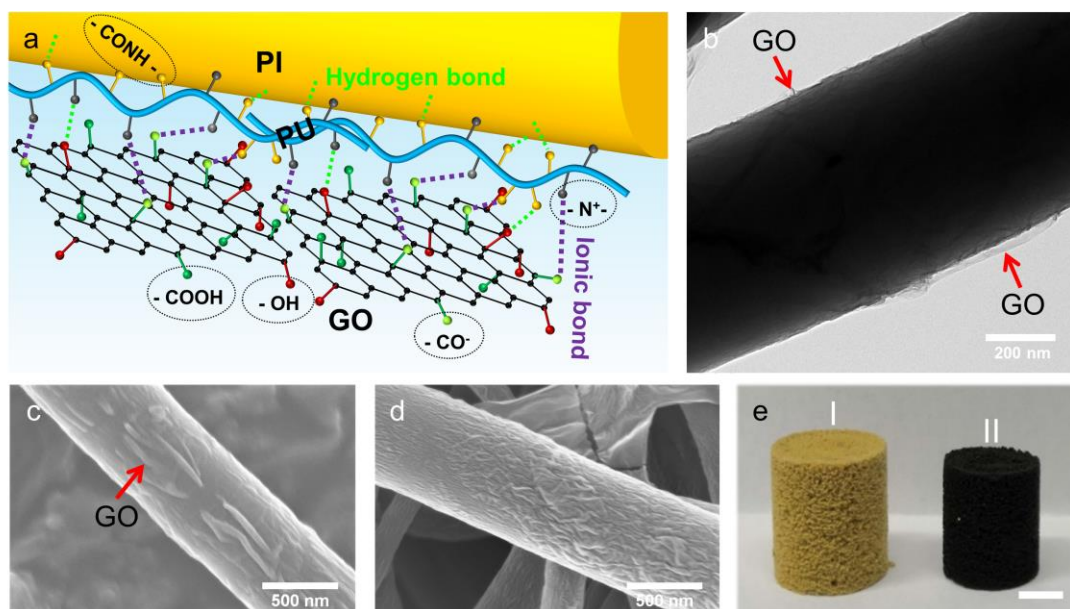
Figure 2-6. (a) The mechanism of surface interactions for the assembly of PIPUGO fibers. (b) TEM and (c) SEM images of PIPUGO fiber. (d) SEM image of PIPUGO fiber after carbonization. (e) The digital images of resulted PIPUGO sponge (f) and NCS (II). Scale bar 1 cm.
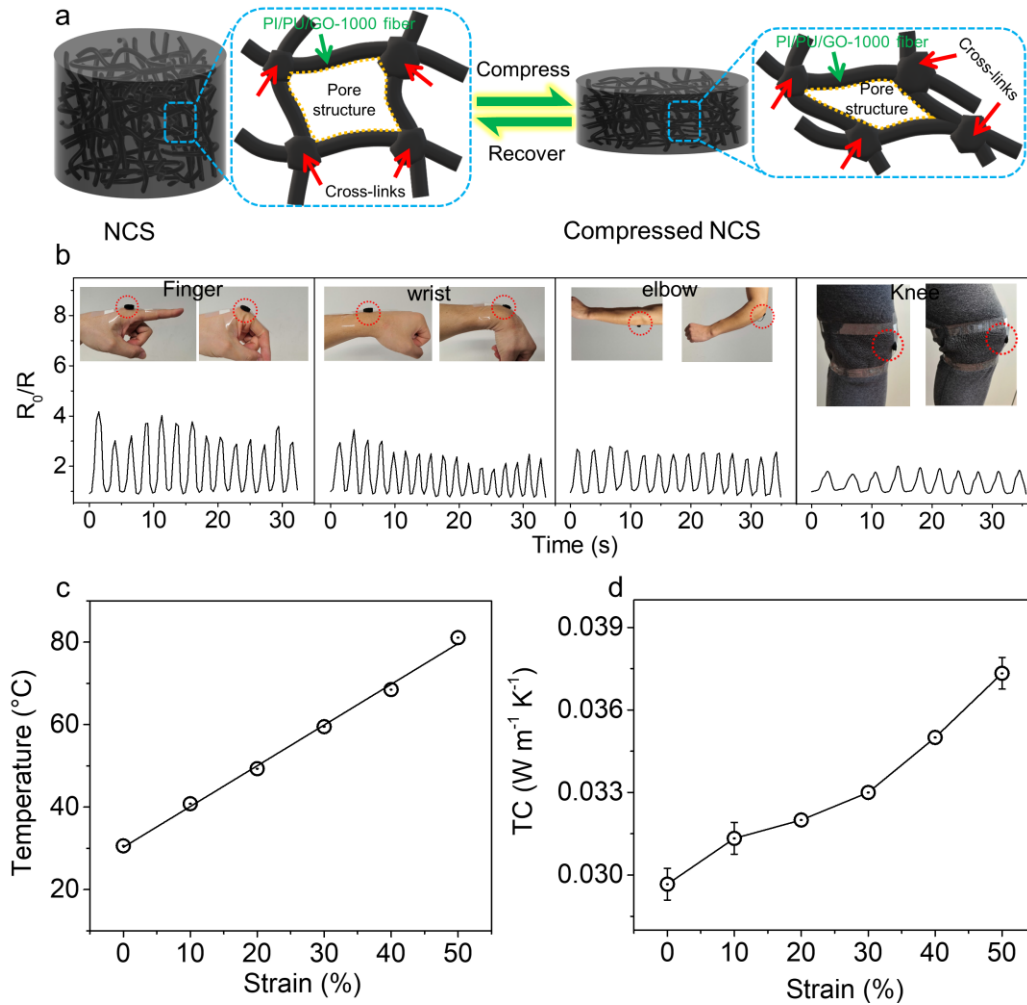
Figure 2-7. (a) Schematic illustration of elastic deformation of NCS. (b) The sensing performance of the NCS sensor for real-time detection of finger, elbow, wrist and knee movements. (c) The mechanoresponsive heating upon different compression strains under 1 V given voltage. (d) The thermal conductivity (TC) of NCS upon different compression strains.

Physically robust and mechanically stable looking sponge was subjected to a multi-compression test with a compression load up to 80%. As depicted in **Figure 2-7a**, when the NCS was compressed, the fiber skeletons are bent by force instead of breaking. When removing the force, the elastic fiber skeletons recover to original shape, resulting in the shape recovery of the NCS. Thanks to the outstanding reversible compressibility and mechanosensitive electrical conductivity, the NCS sponge can be integrated into a

simple wearable pressure sensor (Figure S14a) which could be used to monitor subtle joint movements (**Figure 2-7b**). The NCS sponge sensor was used to monitor multiple bending movements of the index finger, elbow, wrist, and knees, respectively, where it could be remarkably and regularly identified bending (peak) and straight (valley) states of joint movements in the consistent real-time electrical signal, demonstrating NCS sensor a highly potential candidate in wearable sensors. Furthermore, our NCS displayed an advanced mechanoresponsive Joule heating performance upon loading compression. It demonstrated a linear relationship with different loading compression strains under 1 V given voltage and realized a widely tunable temperature range from room temperature to 81 °C by giving a compression strain from 0 to 50% as shown in **Figure 2-7c**. The mechanoresponsive heating behavior of NCS allows heating devices to work in a more energy-saving heating modality. The NCS displays thermal conductivity 0.029-0.037 W m^{-1} K^{-1} depending upon the compressing strain from 0 to 50% (**Figure 2-7c**), which are measured by a HotDisk instrument. This means even though our sponge was even under a high compression state and increased density, it is still a prominent thermal insulating material.

Additionally, both thermal conductivity and electrical conductivity of NCS are adjustable in accordance with density. Changing density from 6.4 mg cm^{-3} to 29.1 mg cm^{-3}, although led to a change of thermal conductivity from 0.027 W m^{-1} K^{-1} to 0.038 W m^{-1} K^{-1}, still maintained a very low value. In comparison the thermal conductivity of some common materials are: natural sheep wool (0.039 W m^{-1} K^{-1}), cotton (0.040 W m^{-1} K^{-1}), commercial fiber insulating board (0.048 W m^{-1} K^{-1}), most of other type commercial insulation materials (0.035-0.160 W m^{-1} K^{-1}) (**Figure 2-8**). Depending on its interesting thermal properties including mechanoresponsive electric Joule heating and outstanding thermal insulation performance, the NCSs suggest a high promise for the application as wearable devices for the thermal management keeping the human body warm. This means our sponge based on the fore-mentioned combination properties, could serve as an ultralight electrical conductor and a high-performance thermal insulator, which could be very promising for wearable electronics. Furthermore,

the intriguing electric heating feature can be used for heat compensation and heat therapy to wearers.
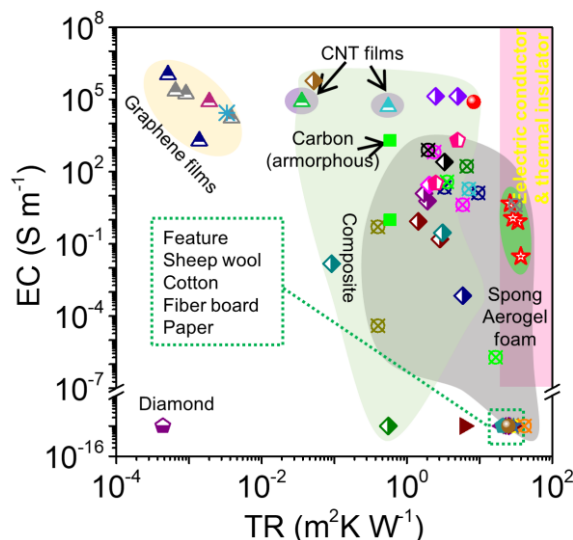
Figure 2-8. Comparison of the electrical conductivity (EC) and thermal resistivity (TR) versus other materials.

In summary, we explore ultralight carbon sponges by carbonizing GO-coated PI composite sponges. The resultant sponges demonstrate uniform GO coatings on fibers, ultralow density, prominent mechanical flexibility, high electrical conductivity, and high thermal insulation, as well as fire-retardant property. Our sponge displays attractive mechanoresponsive electrical and thermal properties. Based on these advantageous characteristics, our sponge demonstrated a novel application for multifunctional wearable sensing systems with an advanced modality of thermal management. Additionally, the excellent thermal stability endows our sponge's fire retardant characteristic, which is a crucial safety factor to wearers.

3. Conclusion and Outlook

The advanced electrically conductive system refers to electrospun polymer fibers, which can interact with the user/environment. The convergence of polymer fibers and flexible electronics has demonstrated to combine the advantages of each technology: the computational feasibility of modern electronics with the wearable, flexible and easy-processable fiber assemblies. In this dissertation, we have explored advanced electrically conductive systems, which are derived from nonconductive but flexible polymer fibers. By designing novel structures, including dual-sided, sandwich-like and 3D spongy types, these conductive systems are endowed discrepant mechanical, optical, thermal and conductive performance, based on which operations with different purposes, such as for thermal management and physical activities monitoring, are successfully demonstrated to be utilized as flexible electronic devices. Thanks to the ultralow density of electrospun fiber assemblies, the obtained conductive systems presented ultralight character, which is greatly beneficial for the improvement of the device's portability. Additionally, the inherent pore structure derived from nanofiber assemblies improves the breathability of systems, significantly improving the wearing comfortability.

Although electrospun fibers have been intensively used in the field of flexible electronics, there are still some challenges involved in improving the device performance. (1) The first challenge is the poor electrospinnability of the conducting polymer. Although flexible electronic devices have been reported consisting of conducting polymeric (e.g. PANi, PPy, PEDOT:PSS, P3HT) nanofibers or conducting composite nanofibers, spinnable conducting polymers are still very limited. Therefore, developing novel conducting polymer and improving the spinning system are highly required to achieve the construction of high-performance nanofibrous flexible devices. (2) Another challenge is the issue of the conductivity degradation of composite fiber. Conducting fibers are generally developed by blending conductive additives, such as

metal NP, NW, graphene or CNT. However, the conductivity of the resulting composited fiber decreases significantly compared to that of pure additive, induced by the blending of a large amount of polymer. Reducing the amount of polymeric component in the fiber can improve the conductivity, but another issue of the significant reduction of mechanical property will come up. Hence, it is crucial to generate new strategies to conquer this problem. (3) In addition, some electrospun materials such as CNFs and inorganic oxide nanofibers, present limited flexibility, resulting in the inferior mechanical deformation ability of the devices. (4) The effects of precise structure patterning and controllability on the device performance are vital to the devices. Thus, it is urgent to tune the assembly and orientation device of the fiber more precisely, in order to achieve a high-performance device. (5) It is very important to develop integrated and portable flexible devices. A combination of multifunctionality is highly desirable regarding the next-generation flexible electronics, which integrate mechanical and temperature sensing, physiological index analyzing, wireless data collecting and processing, and self-powering function. We believe that such a multifunctional device will bring new chances and challenges into our future lives.

4. Acknowledgement

First of all, I would like to thank my mother country **China** and the **China Scholarship Council** for supporting me to study in the group of MC ll.

Second, I would like to express my sincere appreciation here to all those who ever assisted me during my Ph.D. period.

I am deeply grateful to my supervisor **Prof. Dr. Andreas Greiner** for his enthusiasm for my projects, for his support, encouragement and patience. He is the person who leads me to pursue scientific truth, and always points me in the right direction whenever I have confusion in the scientific research. Also as a mentor of life, he taught me how to face difficulties with a smile. when I encountered failure every time, his encouragements always kept me full of confidence to overcome them. His impacts on me are will benefit me for the rest of my life.

I would like to express my sincere gratitude to **Prof. Dr. Seema Agarwal** for her supports in my works from experiment design to manuscript writing. I have benefited greatly from her wealth of knowledge and meticulous editing skills.

I would like to thank **Prof. Dr. Markus Retsch** for the supports and suggestions on thermal characterizations to my work. Through the cooperation with you, I have gained much knowledge and experience in electrical and thermal conduction.

I would like to thank my corporators, **Bernd. A. F. Kopera** for the characterizations and discussions on the thermal property of AgNWs, **Jian Zhu** for the SEM measurements and result discussions on the sandwich membrane, **Xiaojian Liao** for the measurements and discussion on the tensile tests of sandwich membrane and carbonization of carbon sponge, **Tobias Lauster** for characterizations and discussions on IR properties of dual-sided nonwoven, **Dr. Sabine Rosenfeldt** for the characterizations and discussions on graphene oxide coated fibers, and **Thomas Tran** for the measurements and discussions on real-time resistance of carbonized sponge. Sincerely thank to **Prof. Dr. Chao Gao** for the suggestions and revising of the

5. Appendix

Breathable and Flexible Polymer Membranes with Mechanoresponsive Electric Resistance

Qiang Gao, Bernd A. F. Kopera, Jian Zhu, Xiaojian Liao, Chao Gao, Markus Retsch,* Seema Agarwal, and Andreas Greiner*

Flexible low-resistance membranes play an important role in soft electronics as sensors for robotics, body movement monitoring, nanogenerators to collect kinetic energy from body movements, and flexible batteries. Despite great efforts, low-resistance, mechanically stable large-dimensional membranes that tolerate very high deformability without sacrificing resistance produce low joule heating and allow passage of gases for human comfort are still being sought. Here, one of the solutions is provided by sandwiching a network of silver nanowires (AgNWs) between two highly porous electrospun thermoplastic polyurethane (TPU) membranes. The membranes are mechanically robust (both for bending and stretching) with a strong interface and large strain before breakage (more than 700%). The sheet resistance is as low as <0.1 ($\pm$0.01) Ω sq^{-1}, and changed to only 1.6 ($\pm$0.43) Ω sq^{-1} upon stretching to 100% strain. The combination of polymer elasticity and the AgNW network structure provides a reversible change in resistance beyond 100% strain. A detailed thermographic analysis is employed to in situ image and characterize the AgNW network morphology during various stretched conditions. It is believed that this flexible, sandwich-like, electrically conductive membrane is a good candidate for smart wearable devices and soft robots.

1. Introduction

Traditional electronics are typically composed of intrinsically heavy and rigid materials, like silicon, metals, and glass, that have extremely limited flexibility, stretchability, bendability, twistability, and impact resistance. There is great need for flexible and deformable circuits and electrodes with low electric resistance that maintain performance even at strained state because of the current rapid development of lightweight, wearable, and flexible electronic devices.[1] Efforts to construct flexible circuits and electrodes with low resistance focused on elastomeric electrically conductive materials. Examples include electrically conductive sponges,[2] hydrogels,[3] nonwovens,[4] films,[5] and fibers.[6] These materials are promising for energy production and storage,[7] actuators,[8] sensors,[9] electronic skin,[10] and soft robotics.[11] However, obtaining flexible conductors with both high strain properties and low resistance is a challenge for design and production of flexible electronic devices.[12] Further, porosity is an important requirement in case electronic devices are meant for contact with skin. Air permeability is very important for the comfort of wearable devices. Achieving a combination of flexibility, elasticity, high conductivity, in porous membranes with good mechanical integrity is a continued search.

Presently, typical flexible electrodes are composed of an elastic substrate as the elastomer to support bending, stretching, and twisting. The most commonly used materials

Q. Gao, J. Zhu, X. Liao, Prof. S. Agarwal, Prof. A. Greiner
Macromolecular Chemistry and Bavarian Polymer Institute
University of Bayreuth
Universitätsstrasse 30, 95440 Bayreuth, Germany
E-mail: greiner@uni-bayreuth.de

B. A. F. Kopera, Prof. M. Retsch
Department of Chemistry
Physical Chemistry I and Bavarian Polymer Institute
University of Bayreuth
Universitätsstrasse 30, 95440 Bayreuth, Germany
E-mail: markus.retsch@uni-bayreuth.de

(iD) The ORCID identification number(s) for the author(s) of this article can be found under https://doi.org/10.1002/adfm.201907555.

Prof. C. Gao
MOE Key Laboratory of Macromolecular Synthesis and Functionalization
Department of Polymer Science and Engineering
Institute of Applied Mechanics
State Key Laboratory of Fluid Power and Mechatronic Systems
Zhejiang University
Hangzhou 310027, P. R. China

Prof. C. Gao
Hangzhou Gaoxi Technology Co., Ltd.
Hangzhou 310027, P. R. China

are: polydimethylsiloxane (PDMS),[13] thermoplastic polyurethane (TPU),[14] electrically conductive polymers,[15] carbon materials,[16] metal nanoparticles,[17] and metal nanowires.[18] Technically, low-resistance electrodes provide the advantages of less energy loss and joule heating. Silver is an excellent material for electrodes and is often used for flexible electrodes with low resistance.[19] In our previous work, we prepared electrospun polymer membranes with a metal-like conductivity of 7.5×10^5 S m^{-1} using a very low content of silver nanowires (AgNWs: 3.35 vol%) as an additive.[4] However, this kind of electrically conductive membrane is bendable but not sufficiently stretchable.

To prepare flexible membranes, printing fabrication techniques have been developed by transferring electrically conductive materials from a working substrate to another target substrate, such as PDMS, TPU, and polyethylene terephthalate (PET).[20] Additionally, printing fabrication techniques provide a simple and versatile way to design and print patterns on substrate materials using computer control.[14,21] In addition, microfluidic processing,[22] microchannel wetting patterning,[23] direct laser patterning,[24] shadow mask patterning,[25] and photolithographic[26] methods have also been developed to fabricate flexible conductors. Other methods, such as filling of a AgNW network prepared by spray drying of a AgNW dispersion with PDMS was also used for making stretchable, conductive electrodes.[13b] Nevertheless, the stretchable conductors prepared with these methods are all airtight due to their nonporous elastic substrate.

Alternatively, electrospinning is a promising technique for fabricating porous substrates with high conductivity, flexibility, and air permeability. The good electrospinnability of many different polymer types also provides the advantage of tuning the membrane mechanical characteristics. For example, electrospun polyamide nanofiber nonwovens embedded with AgNW networks showed 50% stretchability and a sheet resistance of 8.2 Ω sq^{-1}.[27] Electrospun polyurethane nonwoven porous substrate coated with AgNW provided highly stretchable membrane (more than 300%) with high conductivity.[28]

Here, we present a flexible and breathable polymer membrane with bending/stretching stability and very low electrical resistance as a new electrode material. Also, we provide important fundamental studies regarding analysis on island formation, evolution of anisotropy and hot-spots, and thermal transport in such structures. Our study shows 1) a simple preparation method for making such membranes which is applicable to large-dimension samples. We use a network of AgNWs as conductive layer sandwiched between two porous TPU fibrous nonwovens made by electrospinning. We improved the interface stability with polycaprolactone (PCL) hot glue in the form of short fibers dispersed in between the AgNW network. 2) Our membranes show a sheet resistance as low as <0.1 Ω sq^{-1}. The resistance does not significantly increase upon deformation (twisting, bending and stretching to approximately 100% strain). 3) We also show a reversible change in the resistance upon stretching or bending with more than 100% strain for several cycles. The AgNW networks reversibly breaks and reforms during stretching and releasing, respectively. 4) Our membranes are breathable. This allows the exchange of gases, which is important for human comfort. 5) Our membranes are thermal insulators comparable to porous polymers, despite their electrical conductivity. We think that our membranes are a promising material for electrodes in smart textiles and other wearable devices.

2. Results and Discussion

The concept for the preparation of flexible and breathable electrically conductive membranes is illustrated in **Figure 1**. First, we prepared TPU nanofiber nonwovens via
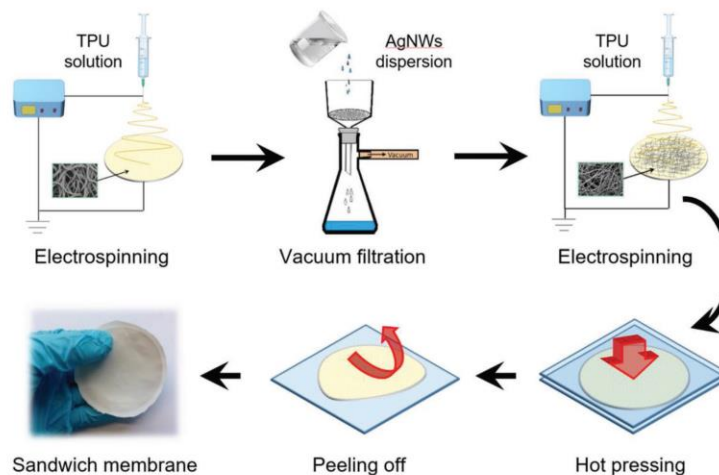
Figure 1. Schematic of preparing the TPU-AgNW/PCL-TPU membrane by sandwiching a network of AgNWs between TPU layers.
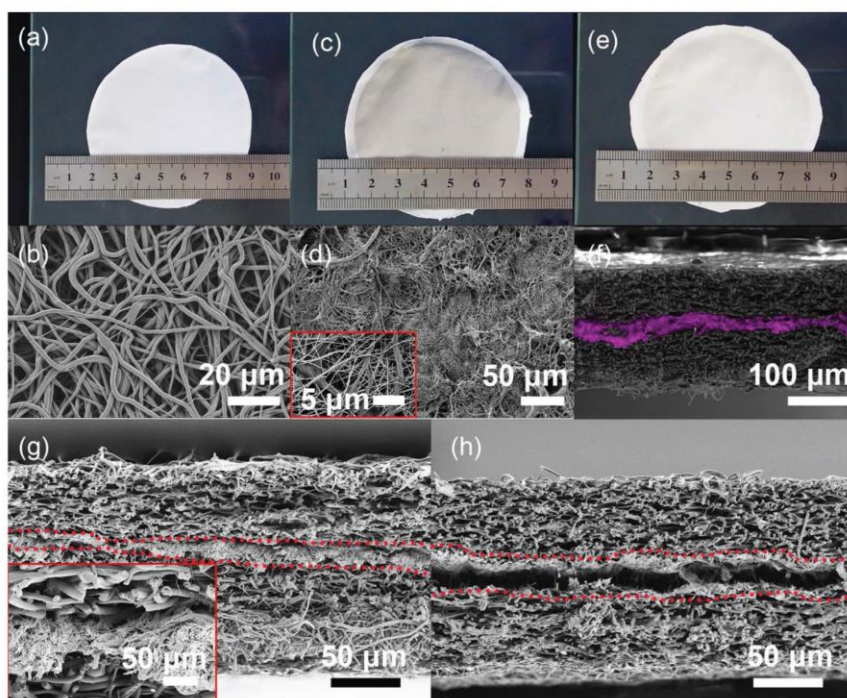
Figure 2. Photograph a) and SEM image b) of the electrospun TPU nonwoven. Photograph c) and SEM image d) of the electrospun TPU nonwoven layered with AgNWs and PCL after heating. Photograph of as-prepared sandwich membrane of TPU-AgNW/PCL-TPU e). Cross-section of EDX overlapped SEM image of as-prepared sandwich membrane of TPU-AgNW/PCL-TPU with PCL short fibers f). Cross-section of TPU-AgNW/PCL-TPU g) and TPU-AgNW -TPU h).

electrospinning. We then used the porous TPU membranes as a filter for the filtration of AgNWs (17 mg mL^{-1}, 126 ± 10 nm in diameter and 18 ± 4 µm in length, Figure S1, Supporting Information) mixed with a PCL short-fiber dispersion (1 mg mL^{-1}, average aspect ratio ≈1000, Figure S2, Supporting Information). The TPU nonwovens consist of randomly oriented fibers (the 2D order parameter is around 0.1) with an average diameter of 1.6 ± 0.5 µm (**Figure 2**a,b). After filtration, the AgNWs and short PCL fibers generated a double network-type structure due to percolation (Figure 2c,d). Afterward, we covered the AgNW/PCL layer with another layer of TPU nonwoven by electrospinning. Finally, we hot pressed the three-layer stack at 75 °C for 30 min to melt the PCL and increase the adhesion of the layers (Figure 2e). The resulting three-layer membranes are designated as TPU-AgNW/PCL-TPU. We checked the presence of an AgNW layer sandwiched between the two TPU layers with PCL short fibers by EDX (Figure 2f). The cross-sectional SEM images of TPU-AgNW/PCL-TPU and TPU-AgNW-TPU (without the use of PCL short fibers for comparison) are shown in Figure 2g,h, respectively. The PCL short-fiber dispersion acts as a glue between the AgNW network and the TPU. The importance of providing a good adhesion between the fiber support

and the conducting nanowires was also investigated by Jiang et. al.[28] Omitting the PCL left us with a loose interface between the layers. Figure S3, Supporting Information, shows the morphology of the middle layer composed only of PCL short fibers after hot pressing at 75 °C for 30 min. Patches of molten fibers can be observed.

The pore size distribution (Figure S4, Supporting Information) of the sandwich membrane without AgNWs is mainly distributed at 2.8 µm with 80% porosity. Upon formation of the AgNW network layer, the average pore size was 1.5–0.9 µm. Additionally, the thickness of the sandwich membrane increased slightly with increasing volume of the AgNW solution, from 0.18 ± 0.4 to 0.27 ± 0.02 mm, as shown in Figure S5, Supporting Information.

Different amounts of the AgNW dispersion were used to investigate the influence of the AgNW concentration on the air permeability and electrical properties. The relevant parameters are illustrated in Table 1. The sheet resistance was as high as 6.1 ± 0.3 × 10^8 Ω sq^{-1} without an AgNW layer. The sheet resistance decreased to as low as 0.09 Ω sq^{-1} upon increasing the amount of AgNWs because of the formation of a dense network of AgNWs. Even the use of a small amount of AgNWs

Table 1. The relevant parameters of flexible sandwich-like electrically conductive membranes with different contents of AgNWs.

Sample	TPU spinning solution (16 wt%) [mL]	PCL dispersion (1 g L^{-1}) [mL]	AgNW dispersion (17 mg mL^{-1}) [mL]	Density [gm^{-2}]	Content of AgNWs [wt%]	Sheet resistance of the AgNW layer [Ω sq^{-1}]
TPU-PCL-TPU	1	10	0	–	–	$6.1 \pm 0.3 \times 10^8$
TPU-0.1AgNW/ PCL-TPU	1	10	0.1	0.51	0.5 ± 0.6	$2.4 \pm 3.1 \times 10^6$
TPU-0.25AgNW/ PCL-TPU	1	10	0.25	1.28	1.2 ± 0.5	1.14 ± 0.15
TPU-0.5AgNW/ PCL-TPU	1	10	0.5	2.56	2.0 ± 0.6	0.39 ± 0.07
TPU-1.0AgNW/ PCL-TPU	1	10	1.0	5.12	3.5 ± 0.4	0.20 ± 0.02
TPU-1.5AgNW/ PCL-TPU	1	10	1.5	7.68	7.9 ± 1.2	0.16 ± 0.04
TPU-2.0AgNW/ PCL-TPU	1	10	2.0	10.24	8.5 ± 1.7	0.09 ± 0.002

– represents no AgNW in the sample.

(1.2 wt%) significantly decreased the resistance to $\approx$1 Ω sq^{-1}. Further reduction in the amount of AgNW to $\approx$0.5 wt% led to a sharp increase in the sheet resistance ($2.4 \pm 3.1 \times 10^6$ Ω sq^{-1}). This indicates that the amount of AgNW required for making a network by percolation is somewhere between 0.5 and 1.2 wt%. In general, the sheet resistance of TPU-AgNW/PCL-TPU remains almost unchanged at 100 °C in air for more than 60h (Figure S6, Supporting Information).

The TPU-AgNW/PCL-TPU membranes also possess good gas permeability (Figure S7, Supporting Information), as demonstrated by the penetration of carbon dioxide (CO_2) gas, visualized by the pink base solution containing phenolphthalein indicator (Video S1, Supporting Information).

The sandwich membranes exhibited stress at break of more than 8 MPa. The TPU without AgNWs had a breaking stress of $\approx$10 MPa. We observed excellent stretchability for the TPU-AgNW/PCL-TPU membranes. The membranes with different amounts of AgNWs can be stretched to over 700% (**Figure 3**a). The membranes showed 10% and 30% creep after stretching for 100 cycles to 50% and 100% strain, respectively (Figure S8, Supporting Information). We measured the resistance as a function of % strain (Figure 3b). TPU-AgNW/PCL-TPU can tolerate considerable strains with a moderate increase in resistance depending upon the amount of AgNWs. The sample with the highest content of AgNWs (TPU-2.0AgNW/PCL-TPU; 8.5 wt%) changed its resistance by only two orders of magnitude at a strain of $\approx$150%. In contrast, the sample with the fewest AgNWs (TPU-0.25AgNW/ PCL-TPU; 1.2 wt%) showed a comparable increase in resistance already at a strain of only 60%. The network was sparse due to fewer AgNWs in TPU-0.25AgNW/PCL, which led to a higher initial sheet resistance and stronger increase in resistance during stretching.

Figure 3c shows the morphologies of the AgNW layer after 0%, 100%, and 150% stretching and recovering to 0% again for the TPU-2.0AgNW/PCL sample (8.5 wt% AgNWs). When the membrane was stretched up to 100%, hardly any cracks could be observed in the AgNW layer. However, upon further stretching to approximately 150%, large cracks (bright area) occurred, causing a significant increase in resistance. The cracks visualize that the AgNW breaks up in an island-like fashion. The formation of island-like structures is confirmed by EDX measurement (Figure 3d). The separated islands and cracks restricted the flow of electricity and in turn created hot spots (Figure S9, Supporting Information) by joule heating at the bottle necks. Such hotspots can be imaged by infrared thermography when applying a DC current (Figure 3e). The hotspots shift with increasing strain and highlight the dynamic changes within the AgNW network upon stretching (see Video S2, Supporting Information). Depending on the overall resistance of the composite sample and local bottle necks this can lead to substantial Joule heating resulting in a fatal failure of the sandwich structure at high strains. For low power applications and in the light of practical strains for the case of wearable electronics our sandwich structure will operate in a safe window with low Joule heating.

The morphological changes of the AgNW network upon stretching cannot be directly assessed, since they are embedded between two layers of TPU fibers. We, therefore, employ direction dependent lock-in thermography to gain a better insight on the composite morphology. Using a line laser as a heat source, we are able to probe the overall thermal diffusivity in such a composite sample along different orientations relative to the stretching direction. We see in **Figure 4**a–c that the TPU fibers align expectedly parallel to the stretching direction. Image analysis of these laser scanning microscopy images reveal that the fiber orientation is already complete at a strain of $\approx$100%.

The 2D order parameter (S_{2D}) measures how well the fibers are aligned. The order parameter is given by

$$S_{2D} = \frac{2}{N} \cdot \left[\sum_{i=1}^{N} \left(\cos(\alpha_i - \bar{\alpha}) \right)^2 \right] - 1 \tag{1}$$

where N is the number of stretched fiber orientations in the SEM image, α_i is the angle between the fiber and the horizontal

1907555 (4 of 9)
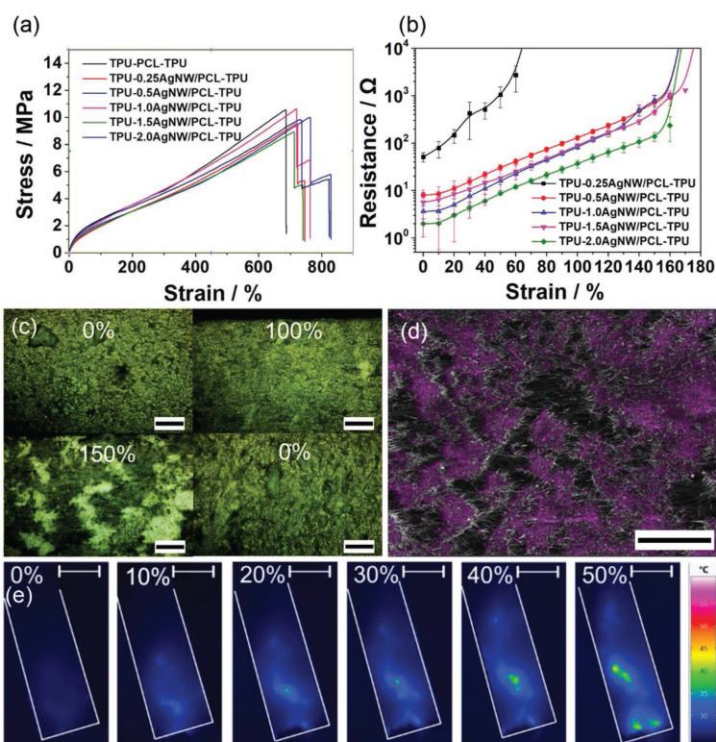
Figure 3. a) Stress–strain curves of sandwich membranes with different amounts of AgNWs. b) Resistance of sandwich membranes with different amounts of AgNWs with different strains. c) Optical images of TPU-2.0AgNW/PCL under different stains. Note the appearance of white spots at 150% strain due to cracks in the AgNW layer. (scale bar: 500 µm) d) EDX-SEM image of TPU-2.0AgNW/PCL at 100% strain. (scale bar: 50 µm) Ag is indicated in purple. e) Thermography images of the TPU sandwich sample upon stretching. White lines indicate the film boundary. A constant current of 2 mA passes through the sample. Note the appearance and shift of hotspots due to local bottlenecks for the electric current created by the cracks in the AgNW layer (scale bars: 3 mm).

axis, and $(\bar{\alpha})$ is the average angle.[29] The 2D order parameter of pure TPU remains constant at a value close to one after 100% strain (Figure 4d). For pure TPU the thermal diffusivity increases along the stretching direction and decreases perpendicular to it (Figure 4e,f). Since TPU is a thermal insulator the absolute thermal diffusivity remains at a low level. The evolution of anisotropy can be explained by the geometric changes, where the fibers start to align, forming an anisotropic fiber network (Figure S10). Heat travels along these oriented fibers faster than perpendicular to it, resulting in a high anisotropy ratio (Figure 4g). The geometric alignment can be accompanied by a molecular orientation of the polymer chains within the fibers, leading to an additional increase in the thermal anisotropy.[30] The thermal diffusivity at 0% strain is higher for the AgNW-TPU sample (TPU-2.0AgNW/PCL-TPU) than for the pure TPU support structure. This can be understood by the additional thermal transport via electronic conduction through the AgNW network. The angular dispersion is rather shallow demonstrating an isotropic temperature spreading in the unstretched and disordered fiber network. Stretching of the fiber network immediately introduces anisotropy to the thermal diffusivity. For AgNW-TPU also some degree of anisotropy evolves (Figure 4h,i), but the thermal diffusivity overall decreases compared to the unstretched state (Figure S11, Supporting Information). This can be understood by a decrease in electronic thermal conductivity in the AgNW layer. The overall thermal diffusivity remains, nevertheless, higher compared to pure TPU. Simultaneously, also for AgNW-TPU samples, we find an evolution of anisotropic heat spreading (Figure 4g). Overall, stretching of the AgNW-TPU sample leads to a smaller amount of anisotropy compared to the pure TPU network structure (Figure 4g). This corroborates our previous findings that the AgNW network is torn into isolated island structures upon stretching. Thermal transport within these island-like structures happens in an isotropic fashion, which shows that the anisotropic orientation of the TPU fiber network is only partially transferred to the AgNW network and counteracted by the evolution of gaps between such islands parallel to the
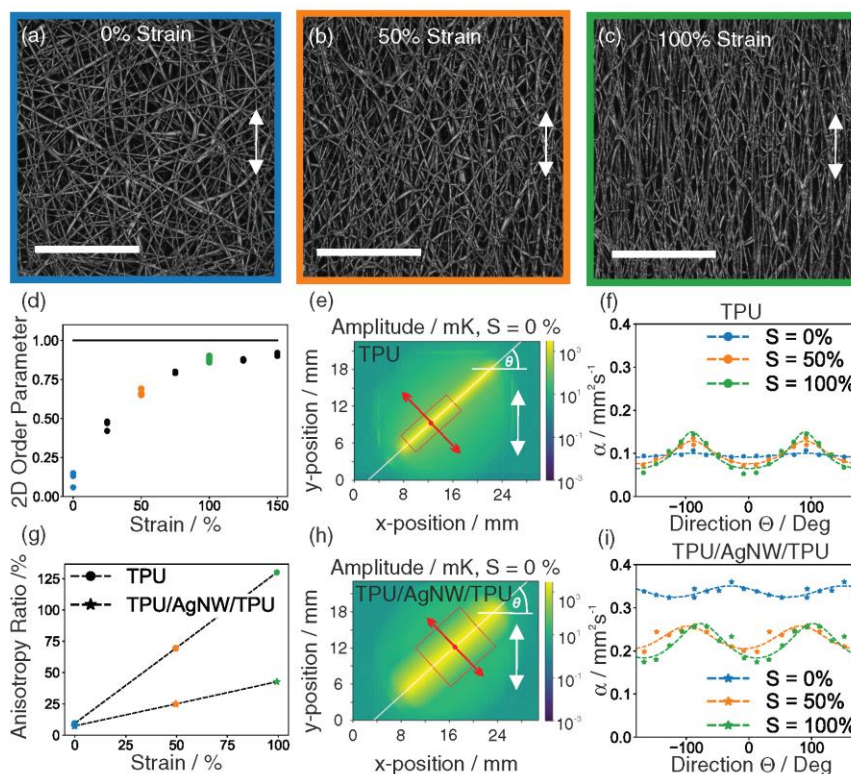
Figure 4. a–c) Laser scanning microscopy images of TPU fibers on the surface of a TPU nonwoven (scale bars: 50 µm). The fibers align in the stretching direction (white arrows) with increasing strain, S. d) The 2D order parameter for the fiber orientation, derived from laser scanning microscopy images, increases from 0.1 to 0.9 with increasing strain. e) Temperature amplitude as a function of position on the surface of a pure TPU. f) Thermal diffusivity as a function of direction (0° is horizontal) and strain for a pure TPU (f). The TPU nonwovens are stretched vertically (+/− 90° direction). Anisotropy ratios for the thermal diffusivity. g) The pure TPU shows a stronger anisotropy than the TPU-2.0AgNW/PCL-TPU. h) Temperature amplitude as a function of position on the surface of TPU-2.0AgNW/PCL-TPU film with 0% strain. i) Thermal diffusivity as a function of direction (0° is horizontal) and strain for TPU-2.0AgNW/PCL-TPU film. The films are stretched vertically (+/− 90° direction).

stretching direction. We corroborate this interpretation with additional orientation analysis of AgNW-TPU samples upon stretching, summarized in Figures S12 and S13, Supporting Information.

We now focus on the reversibility of the stretching/compression process and its implications for electromobility measurements. The membranes, even with very high amounts of AgNWs (TPU-2.0AgNW/PCL-TPU), showed excellent stretchability and bending stability. The samples were subjected to 100 cycles of stretching (**Figure** 5a) and bending (Figure 5b). The resistance change can be described by

$$RC = R/R_0 \qquad (2)$$

where R is the time dependent resistance and R_0 is the initial resistance. Both R and R_0 were measured after stretching and bending tests to prove the stability after deformation.

The RC of TPU-0.25AgNW/PCL-TPU with only 1.2 wt% of AgNWs significantly increased after only 60 stretching cycles, the RC was >20 000 under 50% strain. However, the same sample showed a much better bending stability (bending curvature from 0° to 150°) without a significant change in resistance. The RC of TPU-0.25AgNW/PCL-TPU after 100 bending cycles was merely 1.32. The sample TPU-2.0AgNW/PCL-TPU with a dense network of AgNWs showed both excellent bending and stretching stability. No significant change in the RC was observed for bending tests. During strain testing RC increased by only a factor of ≈20 after 100 cycles. It is important to note that our method of fabrication is particularly suitable to adjust the AgNW concentration in a simple manner. This can even be achieved locally by filtration through a mask. In Figure S14, Supporting Information, we demonstrate, that the local variation of the AgNW concentrations leads to locally confined heating powers. Hence the AgNW
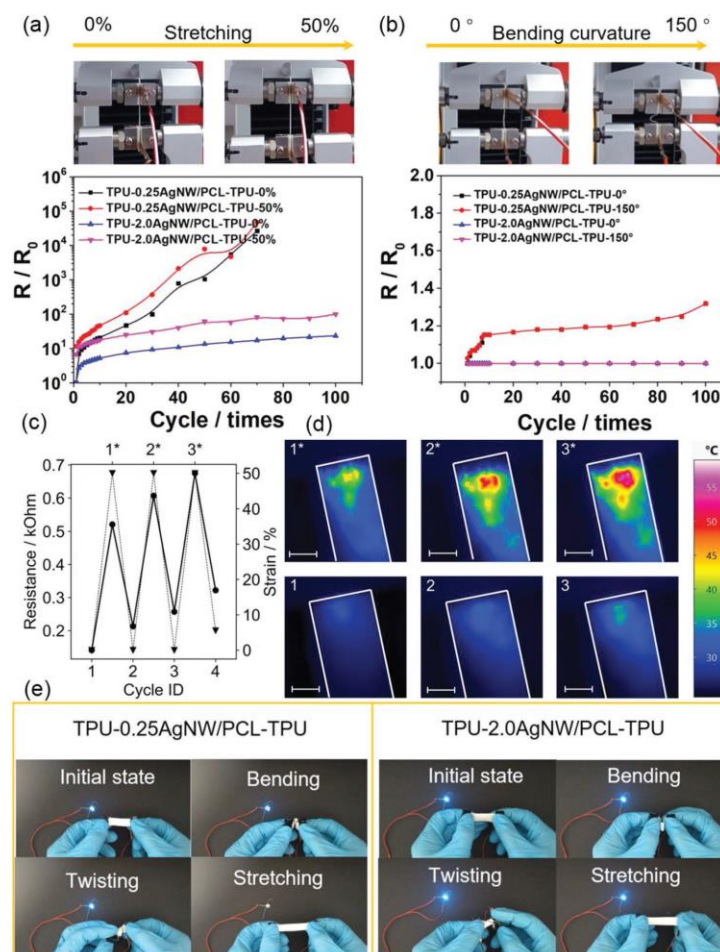
Figure 5. a) Resistance change after 100-cycle stretching test (50% strain). b) Resistance change ratio after 100-cycle bending test (bending curvature from 0° to 150°). Noticing that the bending angle of samples was close to 150° when distance between two clips decreased to 50%. c) Electric resistance (dots) and strain (triangles) during the cycling for the thermographic imaging. d) Thermographic images of a TPU-1.0AgNW/PCL-TPU film during cycling to 50% strain. (scale bars: 5 mm); a constant current of 10 mA passes through the film. The hotspots occur mainly in the stretched state and at different positions from cycle to cycle. e) Digital image of LED brightness by different operation of nonwoven TPU-0.25AgNW/PCL-TPU and TPU-2.0AgNW/PCL-TPU.

concentration, sheet resistance, and response to stretching or bending can be laterally adjusted and optimized for a given application.

We also investigated the changes to the AgNW upon repeated stretching and un-stretching with thermography. This measurement was conducted using a sample of intermediate AgNW concentration (TPU-1.0AgNW/PCL-TPU, 3.5 wt%). Upon stretching (50% strain) we measured an increase in electrical resistance, which translated into hot spot areas.

Consistent with our previous analysis such islands of AgNW network (Figure 3d) almost completely disappear upon release of the strain. In the following stretching cycles these hot-spots reform and increase in number and evolved heat. With this intermediate AgNW concentration, a disconnection between the well conducting AgNW islands happens easier and the re-formation of the intact network becomes less complete, in contrast to the better performing samples with a higher amount of AgNWs.

An LED was utilized to demonstrate the flexibility of the prepared sandwich membrane under various mechanical loads during working conditions. TPU-0.25AgNW/PCL-TPU was connected to a circuit, as shown in Figure 5e, and was bent and twisted. The LED maintained almost the same brightness. However, after 50% strain stretching, the brightness of the LED could hardly be observed. This behavior corroborates the formation of a very high RC of TPU-0.25AgNW/PCL-TPU after stretching. When using a more highly concentrated AgNW network (TPU-2.0AgNW/PCL-TPU) twisting, bending, and stretching (50% strain) are tolerated and the brightness of the LED remained almost unchanged. In addition, detailed information is shown in Video S3, Supporting Information.

The use of TPU-2.0AgNW/PCL-TPU as resistive-type strain sensor[31] in a preliminary test for monitoring finger and wrist bending and unbending movements for several times (Figure S15, Supporting Information) worked very well. The sensitivity and precision would be further investigated and other application areas will also be explored.

3. Conclusion

In conclusion, we proposed a new strategy to fabricate sandwich-like electrically conductive membranes with very low electric resistance. Our material consists of an AgNW network sandwiched between two porous electrospun TPU nonwovens. PCL short fibers act as glue and provide a strong interface between the three layers. Our membranes show good bending and stretching stability, high stretchability (breaking elongation more than 700%) and very low initial electric resistance, as low as $<0.1\ \Omega\ sq^{-1}$ depending upon the amount of AgNWs. This composite structure shows potential for use as a strain sensor to monitor body movement. Additionally, the membrane possesses gas permeability and low thermal diffusivity. Furthermore, our material has the potential to be integrated into smart wearable devices to collect body movement signals using a connected PC or mobile phone in the future.

4. Experimental Section

Materials: In this study, TPU (Desmopann DP 2590, Bayer Materials Science, M_n 88 900, M_w 145 000), PCL (Capa 6800, M_w 120 000, Perstorp UK Ltd.), poly(vinylpyrrolidone) (PVP K30, M_w 40 000, Sigma-Aldrich), ethylene glycol (p.a. ≥99.5%, Fluka), silver nitrate (AgNO₃, p.a. 99.9999%, Sigma-Aldrich), iron chloride (FeCl₃, p.a. 98.0%, Sigma-Aldrich), sodium chloride (NaCl, p.a. 99.0%), and dimethylformamide (DMF, p.a. 99.8%) were used as obtained. Other solvents were distilled before use. The AgNWs were synthesized using a previous method.[4]

Analytical Instruments and Methods: A Zeiss LEO 1530 (Jena, Germany; Schottky field-emission cathode) was used for SEM characterization of the AgNWs and their corresponding networks. EDX was performed using a Zeiss Ultra Plus (Jena, Germany; acceleration voltage of 10 kV). TEM measurements were performed using an elastic bright-field transmission electron microscope (TEM, Zeiss 922 Omega EFTEM) at a voltage of 200 kV. ImageJ software was used to determine the AgNW diameter. An average of 100 AgNWs was taken for the diameter calculation.

The AgNW content was determined from thermogravimetric analysis (TGA Libra F1, Netzsch, Selb, Germany). A heating rate of 20 °C min⁻¹ was used. The measurements were performed in synthetic air.

Pore size measurements were performed with a PSM 165/H (Dresden, Germany) to determine the pore size. Topor was used as the standard test liquid (surface tension = 16.0 mN m⁻¹). The sample holder had a diameter of 11 mm, and a flow rate of up to 70 L min⁻¹ was applied. At least three measurements were carried out for each sample, and an average was taken.

The gas permeability test was performed with a homemade unit as described in our previous work in reference 3. The membrane was fixed at the bottleneck with the cap. A rubber tube (airtight) was used to connect to another glass bottle containing solid carbon dioxide. The glass bottle fixing the nonwovens at the bottleneck was immersed in a phenolphthalein/limewater mixture. The carbon dioxide permeated through the membrane and discolored the aqueous basic solution containing phenolphthalein indicator.

Tensile tests were carried out (sample length 2 cm, width 2 mm) using a tensile tester (ZwickiLine Z0.5; BT1-FR0.5TN. D14; Zwick/Roell, Germany). The following parameters were used: clamping length 1 cm, crosshead speed 10 mm min⁻¹, temperature 20 °C and pretension 0.01 N mm⁻¹. The thickness of the samples was measured with a screw micrometer. The 100-cycle stretching test with 50% and 100% strain was also measured with the abovementioned measuring conditions.

Sheet resistance measurements (four-point measurements) were performed using a Keithley 2420 high-current source meter coupled with a Signatone SYS-301. The sheet resistance was measured ten times for each sample.

A tensile tester (ZwickiLine Z0.5; BT1-FR0.5TN. D14; Zwick/Roell, Germany) was employed to control the stretching distance and bending degree, and a digital multimeter (EMOS Multimeter EM391) connected to measure the sample with a bronze conductor was employed to measure the stretching resistance and bending resistance. The size of the sample and the measuring parameters used here were the same as those used in the tensile test.

Thermography imaging was performed with an Infratec VarioCAM HD research IR camera (7.5–14 μm). The spatial resolution is 29 μm at closest proximity. All measurements were performed in air. The resistance was measured simultaneously with a Keithley 2400 Sourcemeter. The Sourcemeter acted as a constant current source during the four wire resistance measurements. A home built stretching apparatus was used to elongate the samples. The strain was determined from the length change.

Thermal diffusivity was measured with our own, self-built Lock-In thermography setup.[32] Briefly, the films are mounted on a stretchable holder inside a vacuum chamber. An intensity modulated line laser is focused onto the back side of the sample. The intensity modulation creates temperature oscillations inside the thin film. We then detect the surface temperature with a Infratec VarioCAM HD research IR camera. The samples were coated with 25 nm of carbon on both sides to enhance laser absorption and IR emission. The IRBIS active online software from the IR Camera detects amplitude and phase of the temperature fluctuations on the sample surface. The thermal diffusivity is extracted from the material by fitting the linearized amplitude and phase signal, which spreads perpendicular to the line laser excitation.

Optical microscopy was performed on a LEXT Olympus OLS 5000 confocal laser scanning microscope. A 100x magnification lens with a working distance of 300 μm was used. Image analysis was conducted with the Matlab code published by Persson et al.[29]

Preparation of TPU Nonwoven and PCL Short Fibers: Electrospinning of 16 wt% TPU in DMF/THF (80/20 wt%) was carried out to obtain TPU nonwovens with randomly oriented fibers. A round 325 mesh stain-less sieve (70 mm in diameter) at an electrode distance of 15 cm was used as the collector. Other spinning conditions were as follows: positive voltage = 15 kV; temperature = 25 °C; relative humidity = 35%. For spinning PCL, a 15 wt% solution in a mixture of THF/DMF (70/30 wt%) was used. Other electrospinning conditions were the same as those used for TPU spinning. The dispersion (1 g L⁻¹) of short PCL nanofibers was obtained as reported previously by us.[3]

Preparation of Sandwich TPU-AgNW/PCL-TPU Membranes: The preparation procedure for the sandwich membranes is shown

schematically in Figure 1. First, a TPU nonwoven prepared according to the procedure described above via electrospinning was used as a filter. Then, a dispersion of AgNWs and PCL short fibers was filtered. The AgNWs and PCL short fibers formed a conductive layer on top of the TPU nanofiber nonwoven. The fibers were dried under vacuum for 10 min at a pressure of 0.1 mbar. Later, another layer of TPU nanofibers was electrospun on top of the nonwoven with AgNWs and PCL short fibers to construct a flexible, sandwich-like, electrically conductive nonwoven. To induce thermal annealing, the achieved sandwich-like, electrically conductive nonwovens were pressed between two glass plates and heated at a temperature of 75 °C for 30 min to melt the PCL fibers and bond the two layers of TPU nonwovens and AgNWs together.

Supporting Information

Supporting Information is available from the Wiley Online Library or from the author.

Acknowledgements

Conflict of Interest

The authors declare no conflict of interest.

Keywords

[1] a) E. J. Markvicka, M. D. Bartlett, X. N. Huang, C. Majidi, *Nat. Mater.* 2018, *17*, 618; b) Y. J. Hong, H. Jeong, K. W. Cho, N. Lu, D. H. Kim, *Adv. Funct. Mater.* 2019, *29*, 1808247; c) S. Y. Huang, Y. Liu, Y. Zhao, Z. F. Ren, C. F. Guo, *Adv. Funct. Mater.* 2019, *29*, 1805924.
[2] S. H. Jiang, S. Reich, B. Uch, P. Hu, S. Agarwal, A. Greiner, *ACS Appl. Mater. Interfaces* 2017, *9*, 34286.
[3] Y. Zhou, C. J. Wan, Y. S. Yang, H. Yang, S. C. Wang, Z. D. Dai, K. J. Ji, H. Jiang, X. D. Chen, Y. Long, *Adv. Funct. Mater.* 2019, *29*, 1806220.
[4] S. Reich, M. Burgard, M. Langner, S. Jiang, X. Wang, S. Agarwal, B. Ding, J. Yu, A. Greiner, *npj Flexible Electron.* 2018, *2*, 5.
[5] Y. Q. Zeng, T. Li, Y. G. Yao, T. Y. Li, L. B. Hu, A. Marconnet, *Adv. Funct. Mater.* 2019, *29*, 1901388.
[6] a) W. Weng, P. N. Chen, S. S. He, X. M. Sun, H. S. Peng, *Angew. Chem., Int. Ed.* 2016, *55*, 6140; b) S. Lee, S. Shin, S. Lee, J. Seo, J. Lee, S. Son, H. J. Cho, H. Algadi, S. Al-Sayari, D. E. Kim, T. Lee,

Adv. Funct. Mater. 2015, *25*, 3114; c) J. Lee, B. L. Zambrano, J. Woo, K. Yoon, T. Lee, *Adv. Mater.* 2019, 1902532.
[7] R. Cao, X. J. Pu, X. Y. Du, W. Yang, J. N. Wang, H. Y. Guo, S. Y. Zhao, Z. Q. Yuan, C. Zhang, C. J. Li, Z. L. Wang, *ACS Nano* 2018, *12*, 5190.
[8] M. Amjadi, M. Sitti, *Adv. Sci.* 2018, *5*, 1800239.
[9] R. P. Tong, G. X. Chen, D. H. Pan, H. S. Qi, R. A. Li, J. F. Tian, F. C. Lu, M. H. He, *Biomacromolecules* 2019, *20*, 2096.
[10] a) A. Chortos, J. Liu, Z. Bao, *Nat. Mater.* 2016, *15*, 937; b) S. H. Wang, J. Y. Oh, J. Xu, H. Tran, Z. Bao, *Acc. Chem. Res.* 2018, *51*, 1033; c) Y. Lee, J. Park, A. Choe, S. Cho, J. Kim, H. Ko, *Adv. Funct. Mater.* 2019, 1904523.
[11] C. Majidi, *Adv. Mater. Technol.* 2019, *4*, 1800477.
[12] G. Chen, N. Matsuhisa, Z. Y. Liu, D. P. Qi, P. Q. Cai, Y. Jiang, C. J. Wan, Y. J. Cui, W. R. Leow, Z. J. Liu, S. X. Gong, K. Q. Zhang, Y. Cheng, X. D. Chen, *Adv. Mater.* 2018, *30*, 1800129.
[13] a) T. H. Kim, C. S. Lee, S. Kim, J. Hur, S. Lee, K. W. Shin, Y. Z. Yoon, M. K. Choi, J. Yang, D. H. Kim, T. Hyeon, S. Park, S. Hwang, *ACS Nano* 2017, *11*, 5992; b) H. S. Liu, B. C. Pan, G. S. Liou, *Nanoscale* 2017, *9*, 2633.
[14] A. D. Valentine, T. A. Busbee, J. W. Boley, J. R. Raney, A. Chortos, A. Kotikian, J. D. Berrigan, M. F. Durstock, J. A. Lewis, *Adv. Mater.* 2017, *29*, 1703817.
[15] H. H. Shi, N. Khalili, T. Morrison, H. E. Naguib, *ACS Appl. Mater. Interfaces* 2018, *10*, 19037.
[16] a) N. Karim, S. Afroj, S. R. Tan, P. He, A. Fernando, C. Carr, K. S. Novoselov, *ACS Nano* 2017, *11*, 12266; b) C. Zhu, A. Chortos, Y. Wang, R. Pfattner, T. Lei, A. C. Hinckley, I. Pochorovski, X. Yan, J. W. F. To, J. Y. Oh, J. B. H. Tok, Z. Bao, B. Murmann, *Nat. Electron.* 2018, *1*, 183.
[17] M. Tavakoli, M. H. Malakooti, H. Paisana, Y. Ohm, D. G. Marques, P. A. Lopes, A. P. Piedade, A. T. de Almeida, C. Majidi, *Adv. Mater.* 2018, *30*, 1801852.
[18] H. Lee, M. Kim, I. Kim, H. Lee, *Adv. Mater.* 2016, *28*, 4541.
[19] P. C. Hsu, X. Liu, C. Liu, X. Xie, H. R. Lee, A. J. Welch, T. Zhao, Y. Cui, *Nano Lett.* 2015, *15*, 365.
[20] S. J. Benight, C. Wang, J. B. H. Tok, Z. Bao, *Prog. Polym. Sci.* 2013, *38*, 1961.
[21] K. Arapov, E. Rubingh, R. Abbel, J. Laven, G. de With, H. Friedrich, *Adv. Funct. Mater.* 2016, *26*, 586.
[22] S. Kustra, H. Wu, S. Basu, G. K. Rohde, C. J. Bettinger, *Small* 2012, *8*, 3746.
[23] B. R. Yang, W. Cao, G. S. Liu, H. J. Chen, Y. Y. Noh, T. Minari, H. C. Hsiao, C. Y. Lee, H. P. Shieh, C. Liu, *ACS Appl. Mater. Interfaces* 2015, *7*, 21433.
[24] J. W. Yoon, W. S. Chang, S. H. Cho, *Opt. Lasers Eng.* 2015, *73*, 40.
[25] F. Xu, Y. Zhu, *Adv. Mater.* 2012, *24*, 5117.
[26] V. Martinez, F. Stauffer, M. O. Adagunodo, C. Forro, J. Voros, A. Larmagnac, *ACS Appl. Mater. Interfaces* 2015, *7*, 13467.
[27] Y. J. Fan, X. Li, S. Y. Kuang, Y. Kuang, L. Zhang, Y. H. Chen, L. Liu, K. Zhang, S. W. Ma, F. Liang, T. Wu, Z. L. Wang, G. Zhu, *ACS Nano* 2018, *12*, 9326.
[28] Z. Jiang, M. O. G. Nayeem, K. Fukuda, S. Ding, H. Jin, T. Yokota, D. Inoue, D. Hashizume, T. Someya, *Adv. Mater.* 2019, *31*, 1903446.
[29] N. E. Persson, M. A. McBride, M. A. Grover, E. Reichmanis, *Chem. Mater.* 2017, *29*, 3.
[30] J. Liu, R. Yang, *Phys. Rev. B* 2010, *81*, 174122.
[31] a) J.-H. Kim, S.-R. Kim, H.-J. Kil, Y.-C. Kim, J.-W. Park, *Nano Lett.* 2018, *18*, 4531; b) S. Chen, S. Zeng, S. Liu, H. Liu, R. Zheng, K. L. White, A. T. Smith, L. Liu, L. Sun, *Chem. Mater.* 2019, *31*, 8708.
[32] a) A. Philipp, N. W. Pech-May, B. A. F. Kopera, A. M. Lechner, S. Rosenfeldt, M. Retsch, *Anal. Chem.* 2019, *91*, 8476; b) H. M. Akram, H. Maqsood, H. Rashid, *Rev. Sci. Instrum.* 2009, *80*, 075103.

ADVANCED FUNCTIONAL MATERIALS

Supporting Information

Breathable and Flexible Polymer Membranes
with Mechanoresponsive Electric Resistance

*Qiang Gao, Bernd A. F. Kopera, Jian Zhu, Xiaojian Liao,
Chao Gao, Markus Retsch,* Seema Agarwal, and Andreas
Greiner**

WILEY-VCH

Supporting Information

Breathable and flexible polymer membranes with mechanoresponsive electric resistance

Qiang Gao,[1] Bernd A. F. Kopera,[2] Jian Zhu,[1] Xiaojian Liao,[1] Chao Gao,[3] Markus Retsch[2]*, Seema Agarwal,[1] Andreas Greiner[1] *

[1]Q. Gao, J. Zhu, X. Liao, S. Prof. Agarwal, Prof. A. Greiner
Macromolecular Chemistry and Bavarian Polymer Institute
University of Bayreuth
Universitätsstrasse 30, 95440 Bayreuth, Germany
E-mail: greiner@uni-bayreuth.de

[2]Bernd A. F. Kopera, Markus Retsch
Department of Chemistry, Physical Chemistry I
University of Bayreuth
Universitätsstrasse 30, 95440 Bayreuth, Germany
E-mail: markus.retsch@uni-bayreuth.de

[3]Chao Gao
[a] MOE Key Laboratory of Macromolecular Synthesis and Functionalization, Department of
Polymer Science and Engineering, [b] Institute of Applied Mechanics, [c] State Key Laboratory
of Fluid Power and Mechatronic Systems, Zhejiang University, Hangzhou 310027, China.
[d] Hangzhou Gaoxi Technology Co., Ltd., Hangzhou 310027, P. R. China

1

WILEY-VCH

Supplementary figures:
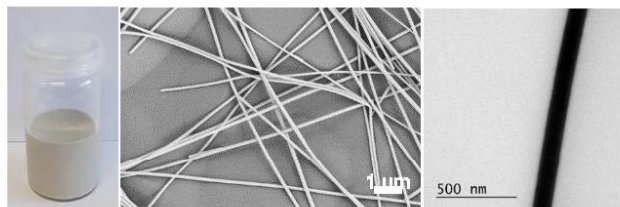
Figure S1. Digital image of the AgNW dispersion (17 mg/mL) (left), SEM (middle) and TEM (right) images of AgNWs.
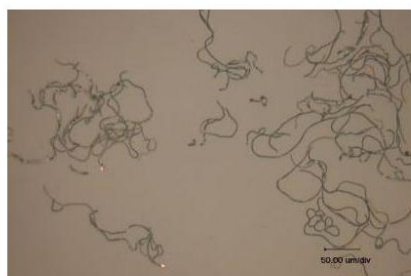
Figure S2. Optical microscopy image of short PCL fibers.
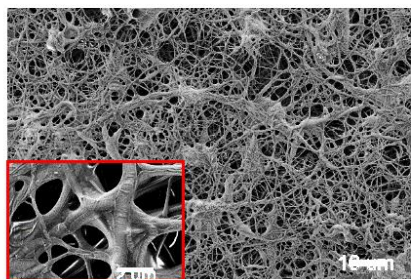
Figure S3. SEM image of TPU- PCL-TPU.

2
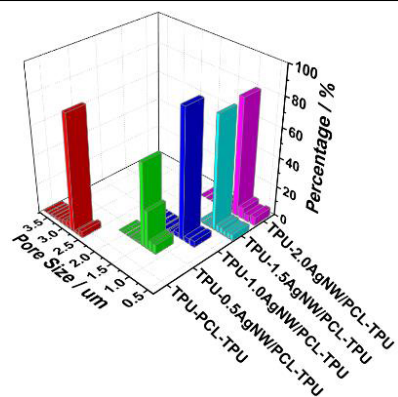
Figure S4. Pore size distribution of the sandwich membranes with different amounts of AgNWs.
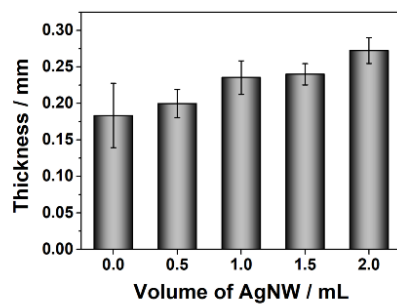
Figure S5. Thickness of sandwich membranes with different amounts of AgNWs.
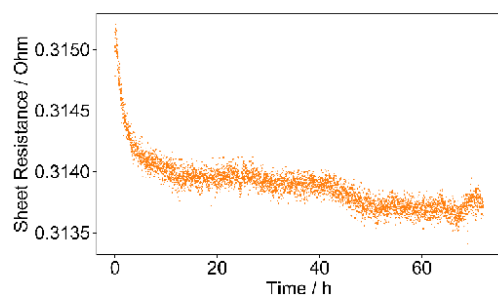
Figure S6. Sheet resistance stability of AgNW in air at 100 °C. The AgNW were ~10 µm in length.

3
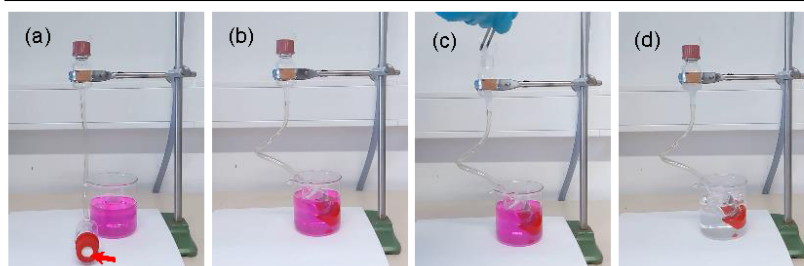
Figure S7. Digital images of the color change of an aqueous basic solution with phenolphthalein indicator; sandwich membrane (indicated by a red arrow) and aqueous basic solution with phenolphthalein indicator (a); the color of the aqueous basic solution with phenolphthalein indicator before (b), in (c) and after (d) adding dry ice.
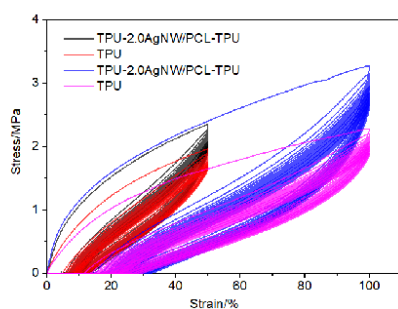
Figure S8. Stress-strain curves of TPU-2.0AgNW/PCL-TPU (100 cycles). TPU-2.0AgNW/PCL-TPU (black): 50% strain; TPU (red): 50% strain; TPU-2.0AgNW/PCL-TPU (blue): 100% strain; TPU (pink): 100% strain.

4

Mechanism of hotspot formation:

After stretching island parts are composed of dense AgNWs and bridge parts are composed of sparse AgNWs form. This is schematically illustrated in Figure S9 and proven analytically by SEM and EDX measurement in Figure 3d. Areas of smaller resistance R1 and far larger resistance R2 form, which coincide with areas of high and low AgNW concentration, respectively. The total resistance of the system is determined by the resistance of bridge parts, which has been reported by Someya et al.(10.1002/adma.201903446). Hence hotspots appear on the bridge parts, according to the joule heating power, P, given by

$$P = R \cdot I^2$$

where R is the electric resistance and I the DC current. TPU is an electric insulator. Therefore, all the current flows through the AgNW network. We used a current source and applied a *constant* current during our measurements. The local heating power, and to some extent, the temperature, is then proportional to the local resistance. The resistance depends on the AgNW cross sectional area perpendicular to the current. Hotspots are therefore indicative of local constrictions (bottlenecks) in the AgNW network.
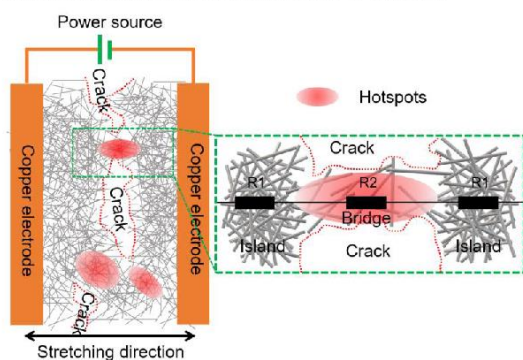
Figure S9. Schematic diagram showing formation of hotspots on stretching. (R1<<R2)

5
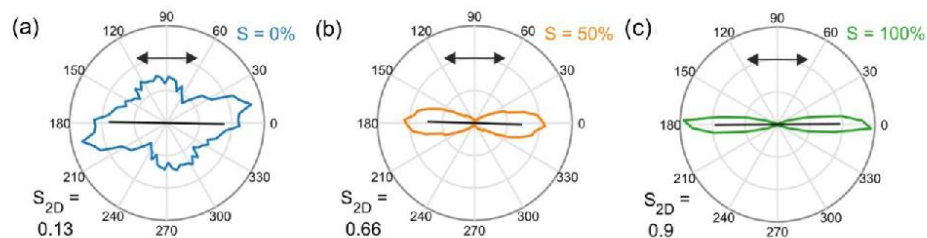
Figure S10. Polar orientation maps for the TPU surface fibers derived from optical microscopy images in different strain of 0% (a), 50% (b) and 100% (c).
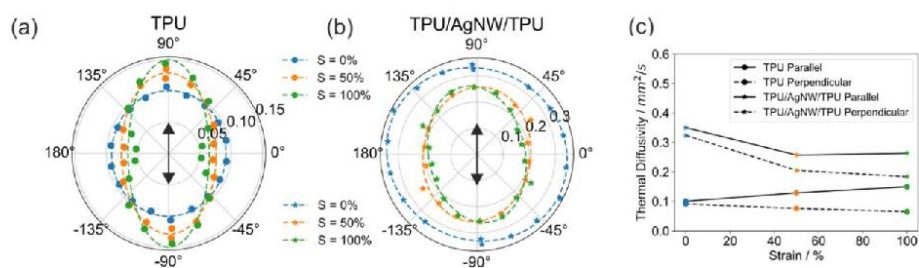
Figure S11. (a, b) Thermal diffusivity as a function of direction for pure TPU and the TPU/ AgNW /TPU sandwich membrane. Black arrows indicate the stretching direction. Dashed lines are ellipses fitted to the data. (c) Thermal diffusivity parallel and perpendicular to the stretching direction as a function of strain.

6
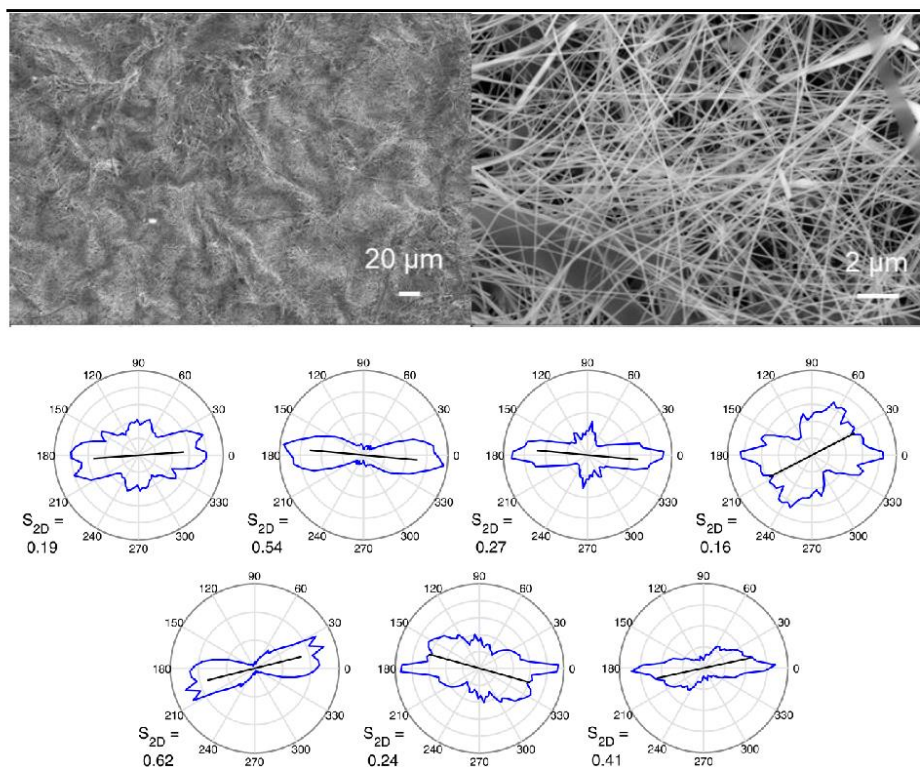
Figure S12. SEM images (top) of AgNWs mesh without stretching (0% strain) and orientation plots from different areas (bottom). The order parameter varies between 0.16 and 0.62. Each polar plot was calculated from a different SEM image. The average of S_{2D} is <0.4, presenting merely partial alignment at 0% strain.

7
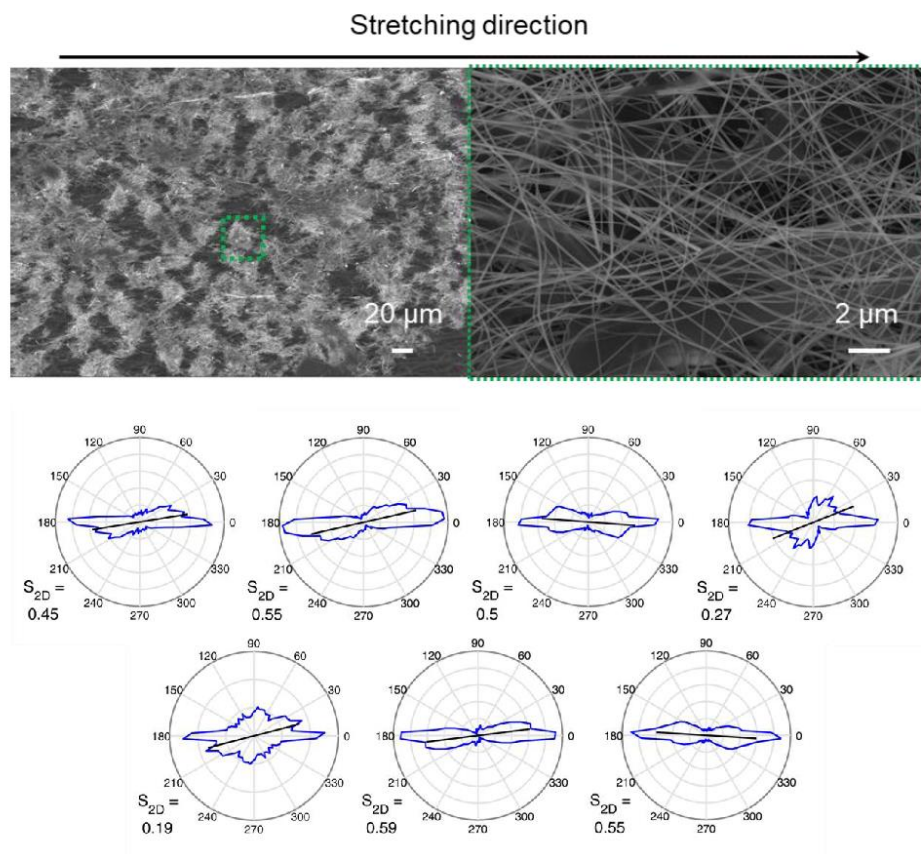
Figure S13. SEM images (top) of AgNWs mesh under 100% strain and orientation plots from different areas (bottom). The order parameter varies between 0.19 and 0.59. Each plot was calculated from a different AgNW island. The average of S_{2D} is ~0.4, at 100% strain, which is close to the order parameter at 0% strain, demonstrating that stretching has no significant influence on the alignment of AgNWs.

8
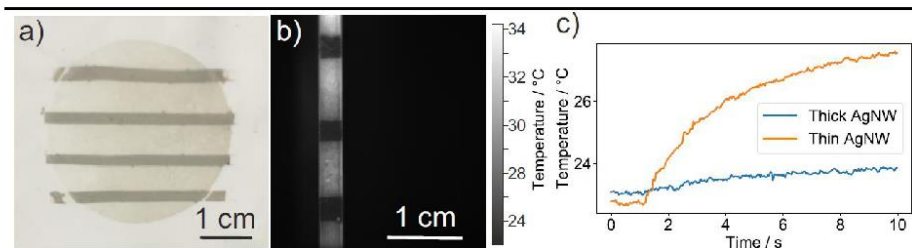
Figure S14. a) Dedicated adjustment of the electrical resistance by local filtration of AgNW dispersion of various concentrations. b) The lateral change in resistance of a thin strip from the sample in (a) is imaged by thermography. A constant current is run through the sample from top to bottom. c) Surface temperature change vs. time. The areas of low AgNW content (wide, bright stripes) become significantly warmer than the dark areas with high AgNW content.

WILEY-VCH
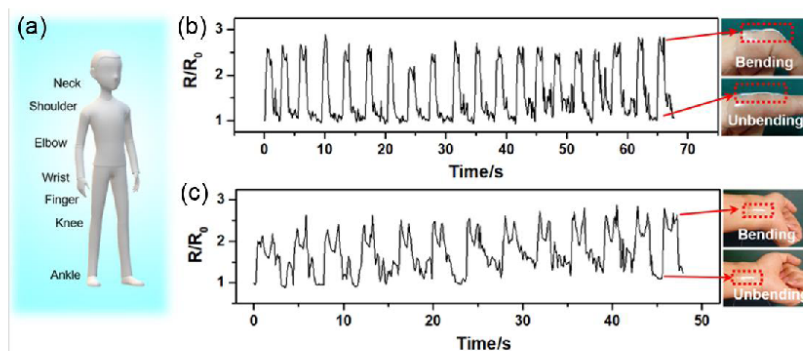
Figure S15. Sandwich membrane utilizing as a strain sensor for monitoring the movement of potential body parts (a); Sheet resistance change ratio for monitoring the movement of finger (b) and wrist (c).

Supplementary Videos:

Video S1. Penetrating experiment of carbon dioxide (CO2) gas-8X speed

Video S2. The hotspots shift with increasing strain upon stretching-4X speed (The constant current of 3 mA was used in this video.)

Video S3. Luminance change of the LED under the bending twisting and stretching deformation-4X speed

10

RESEARCH ARTICLE

Breathable and Flexible Dual-Sided Nonwovens with Adjustable Infrared Optical Performances for Smart Textile

Qiang Gao, Tobias Lauster, Bernd A. F. Kopera, Markus Retsch,* Seema Agarwal,* and Andreas Greiner*

Maintaining constant body temperature is the most basic function of textiles. However, traditional fabrics irradiate a massive amount of thermal energy to the ambient environment due to the high emissivity of the materials used for textiles. This phenomenon weakens the thermal function, causing vast thermal energy loss by dissipation as infrared (IR) irradiation. To improve thermal comfort and reduce extra energy consumption, smart thermal management textiles must maintain constant body temperature by regulating IR irradiation from the human body or by compensating heat losses by joule heating. Here, a smart dual-sided nonwovens' preparation procedure and properties for use as a textile with this combination of properties are shown. The nonwoven combines a high porosity with high IR reflectance and low IR emittance. The nonwoven is adjustable from reflective to emissive when turned inside out. It is consequently permeable to air and vapor and simultaneously mitigates thermal heat losses with radiation. In addition, low sheet resistance and superior flexibility make it possible to use them in flexible electronics and wearable devices. It can be further equipped with a porous Joule heating layer adding active control to the personal thermal comfort.

Q. Gao, S. Agarwal, A. Greiner
Department of Chemistry
Macromolecular Chemistry II and Bavarian Polymer Institute
University of Bayreuth
Universitätsstrasse 30, 95440 Bayreuth, Germany
E-mail: agarwal@uni-bayreuth.de; greiner@uni-bayreuth.de
T. Lauster, B. A. F. Kopera, M. Retsch
Department of Chemistry
Physical Chemistry I
University of Bayreuth
Universitätsstrasse 30, 95440 Bayreuth, Germany
E-mail: markus.retsch@uni-bayreuth.de
M. Retsch
Bavarian Center for Battery Technology (BayBatt)
Bavarian Polymer Institute, and Bayreuth
Center for Colloids and Interfaces
University of Bayreuth
Universitätsstrasse 30, 95440 Bayreuth, Germany

The ORCID identification number(s) for the author(s) of this article can be found under https://doi.org/10.1002/adfm.202108808.

1. Introduction

Thousands of years ago, our ancestors used all kinds of plants to cover the body to keep it warm. In recent centuries, silk, cotton, hemp, and other natural materials were applied in the traditional textile field to realize clothing warmer and more comfortable. Textiles are revolutionized by synthetic materials such as polyesters and nylons, and incorporating smart functionalities has become a trend and research objective. The smart functionalities are introduced for monitoring body movements, detection of metabolic indexes, or energy storage.[1] For instance, solar cell integrated textile is promising for energy storage and charging portable electronic devices.[2] Initially, the textile's essential function is to keep warm and reduce body energy loss for surviving in the frigid natural environment. Traditional textiles concentrate more on lowering body heat transfer into the air surrounding via convection and conduction. However, it fails to insulate body thermal emission due to the high emissivity of ordinary cloth. If heating and insulation could be managed based on human requirements, a huge amount of energy could be saved[3] and personal thermal comfort increased. Hence, personal thermal management devices, wearable like typical textiles and capable of significantly reducing body heat loss or raising the textile temperature according to personal desire, has been developing to improve body thermal comfort control in new strategies and solutions. By regulating heat exchange (infrared (IR) radiation flow) from the human body to its surroundings, developing advanced materials with body thermal irradiation control has attracted considerable attention.[4] IR transparent radiative,[5] emissive radiative,[6] solar-reflecting radiative cooling textiles, and conductive cooling textiles with enhanced thermal conductivity[7] have been widely reported to keep cool in warm surroundings by heat exchange between human body and environment.[3] On the contrary, when in cold climate, textiles with warming purpose are highly demanded to significantly reduce heat loss into the surroundings. This is technically achieved by thermal insulating materials, such as porous aerogel fiber,[8] or IR reflecting materials via incorporating metal particles and metal wires.[6b,9] To compensate for heat dissipation through IR radiation, textiles with electro heating function are highly desired to realize

the aims of harvesting energy from the human body to maintain body temperature constant, especially for those people living in harsh regions.[10]

High-performance polymers like polyimide (PI) have excellent mechanical properties, high chemical resistance and excellent thermal stability. They are often applied as filters, mechanical parts, insulation and passivation films, and medical tubing. Short electrospun fibers constructed polymeric sponge is an excellent thermal insulator with very high thermal resistance thanks to its super-high porosity.[11] Nevertheless, when some electrically conductive materials such as graphene and carbon nanotube,[12] electrically conductive polymer,[13] and metal nanowire[14] were incorporated, these polymeric materials could change their electrical property from non-conductive to conductive, even highly conductive, which often used to prepare wearable devices, such as sensor and triboelectric nanogenerator.[15] Recently, silver nanowire (AgNW) has been established as a promising electrically conductive material applied to prepare various kinds of electronic devices such as smart sensors[16] for monitoring physiological indexes, transparent touch screens,[17] and nanogenerator for energy-harvesting and storage.[18] Additionally, AgNW is also known for its ultralow IR emissivity, thanks to the low emissivity of bulk silver (≈ 0.02). A recently developed AgNWs coated textile showed much higher IR reflectance of $\approx 40\%$ compared to uncoated textile ($\approx 1\%$) and provided 21% more thermal insulation due to the reduction of radiation loss.[9] In comparison, herein, we present the preparation procedure and detailed characterization of an electrically conductive dual-sided PI/AgNW nonwoven with lightweight, highly flexible, air permeable, washable, IR-reflecting, and tailored heating properties. The IR reflecting properties are different on two different sides so that it can be used for multipurpose. The prepared PI/AgNW nonwoven is appropriate for flexible electronics and smart wearable devices and for other applications like for example sensor devices and energy devices for future use.

2. Result and Discussion

The dual-sided nonwovens were prepared, as shown in **Figure 1**. First, the PI electrospun nonwoven (thickness 48.0 ± 2.5 μm, area 10 cm^2, Figure S1a, Supporting Information) was placed on a sand core funnel, and then AgNW dispersion (different amounts of 17 g L^{-1} dispersion) was filtered through the PI nonwoven under vacuum assistance. During this process, AgNW networks were formed on top of the PI nonwoven (Figure S1b, Supporting Information). The average diameters of PI fibers and AgNWs were 0.30 ± 0.07 and 0.10 ± 0.03 μm, respectively (Figure S1c, Supporting Information). A thermoplastic polyurethane (TPU) solution was filtered through the PI/AgNW nonwoven under light vacuum with the intention to bond AgNW networks strongly onto the PI nonwoven by residual TPU acting as glue between the two. The as-prepared nonwovens have dual sides: the AgNW network side (silver gray) and the PI nanofiber layer side (yellow) (Figure 1b). The TPU (blue regions in Figure 1c) is entangled with AgNWs and attached to the PI nonwoven, as confirmed by energy-dispersive X-ray-scanning electron microscopy (EDX-SEM) (Figure 1d). The dual-sided nonwovens are designated as PI/TPU/AgNW-X, where X denotes the volume of AgNW dispersion (17 g L^{-1}) in μL used

for the preparation of nonwovens. PI/TPU/AgNW-25 and PI/TPU-AgNW-500 nonwovens have a thickness of 56.7 ± 1.0 and 57.7 ± 3.1 μm (Figure S2a, Supporting Information), respectively. The pore size (Figure 1e) of PI/TPU was centered around 1.7 μm. The dual-sided nonwoven with fewer AgNWs (PI/TPU/AgNW-25) showed a sparse AgNW network, which insignificantly affected the nonwoven's pore size (≈ 1.7 μm). However, the sample PI/TPU/AgNW-500 showed a decrease in pore size to 0.7 μm due to the denser layer of AgNW networks. All nonwovens were air permeable as the pore structure was retained during the preparation process using a light vacuum for the filtration of TPU and AgNWs (Figure 1f). PI/TPU, PI/TPU/AgNW-25 and PI/TPU/AgNW-500 showed air permeability of 5.2 ± 0.5, 4.3 ± 0.6, and 2.7 ± 0.6 mm s^{-1} respectively, whereas pure PI nonwoven has a permeability of 20.3 ± 0.5 mm s^{-1}. The nonwovens also presented good moisture permeability (Figure S2b, Supporting Information) (≈ 65 mg cm^{-2} day^{-1} for PI/TPU/AgNW-500), which is close to the value of pure PI electrospun nonwoven (≈ 82 mg cm^{-2} day^{-1}). Both sides of the PI nonwovens were hydrophobic with high contact angles (≈ 140 °, Figure S2c, Supporting Information). Although pure AgNWs are very hydrophilic, the AgNW network side of dual-sided nonwovens also showed very high contact angles (145.5 ± 0.1 and 144.9 ± 0.5 degrees for PI/TPU/AgNW-25 and PI/TPU/AgNW-500, respectively) due to the homogeneously dispersed TPU in the network (Figure S3, Supporting Information). The dual-sided nonwovens were as strong as the pristine PI nonwoven (18 MPa in tensile strength, 77% in strain) without any significant effect of TPU or AgNWs (Figure 1g).

As both PI nonwoven and TPU are electrically insulating materials, the electrical property of the dual-sided nonwoven is significantly influenced by the amount of AgNW due to the low resistivity (1.6×10^{-8} Ω m) of silver. The polymeric nonwovens (PI and PI/TPU) showed very high electrical resistance (sheet resistance: $>10^8$ Ω sq^{-1}). The sheet resistance of the dual-sided nonwovens could be tuned to as low as 0.2 Ω sq^{-1} using appropriate amounts of AgNWs. The resistance decreased with the increasing quantity of AgNW (**Figure 2**a and Table S1, Supporting Information) with a discontinuous jump between PI/TPU/AgNW-2.5 and PI/TPU/AgNW-5 from $\approx 5 \times 10^8$ to $\approx 10^5$ Ω sq^{-1}. Denser AgNW networks resulting from more AgNWs, as demonstrated by SEM images (Figure S6, Supporting Information), contributed to high conductivity, resulting in decreased sheet resistance.

The nonwovens are mechanically flexible. In the circuit with PI/TPU/AgNW-500, there was insignificant variation in luminance of the lightening light-emitting diode (LED) bulb with the nonwoven undergoing bending and twisting deformations (Figure 2b) compared to that of the virgin state. These types of bending and twisting deformations are often faced by wearable, flexible devices in everyday life. Additionally, the PI/TPU/AgNW-500 exhibited outstanding electromechanical properties. In particular, the electrical resistance shows a negligible variation ($R/R_0 = 1$, R and R_0 denoting resistance after and before test respectively) even after 100-time repeatable bending (bending angle: $\approx 140°$) (Figure 2c and Figure S7, Supporting Information), indicating high durability and cyclability to withstand non-tensile deformation. When the sample was stretched to about 65% (Figure 2d), there was only a small increase in the resistance of PI/TPU/AgNW-500 from 2 to 40 Ω. In contrast, a higher resistance change was observed for dual-sided
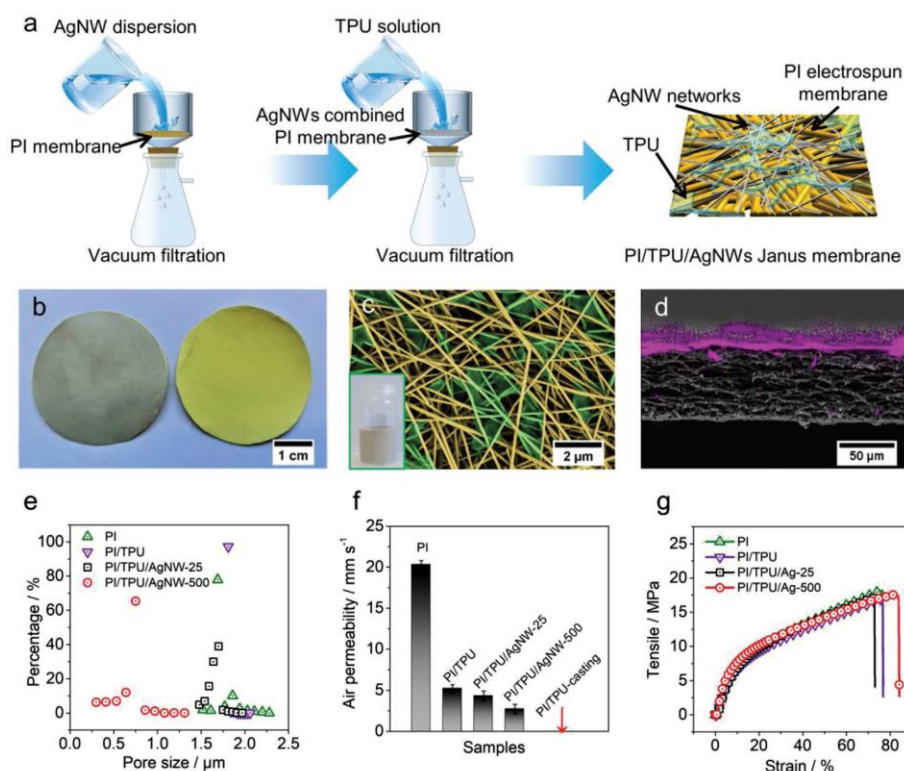
Figure 1. Preparation route a) and b) digital photographs of the dual-sided nonwoven (sliver gray: AgNW networks side, yellow: PI side). c) Photoshop colored SEM image (original image seen in Figure S4, Supporting Information) of AgNW networks with TPU:TPU colored in green. The digital photograph of the AgNW water suspension is shown in the green frame at the left corner. d) EDX-SEM image of the dual-sided nonwoven PI/TPU/AgNW-500. The purple area presented the AgNW networks. e) Pore size distributions of PI electrospun nonwoven, PI electrospun nonwoven with TPU, PI/TPU/AgNW-25, and PI/TPU/AgNW-500. f) Air permeability of PI electrospun nonwoven, PI electrospun nonwoven with TPU, PI/TPU/AgNW-25, PI/TPU/AgNW-500, and PI/TPU-casting. The sample PI/TPU-casting is prepared by casting 2 mL 8 wt% TPU solution on PI electrospun nonwoven (SEM image in Figure S5, Supporting Information). g) Mechanical properties of PI electrospun nonwoven, PI electrospun nonwoven with TPU, PI/TPU/AgNW-25, and PI/TPU/AgNW-500.

nonwovens with fewer AgNWs (PI/TPU/AgNW-25) under similar conditions. It showed a change from ≈700 to ≈8000 Ω merely within 10% strain deformation. In PI/TPU/AgNW-25 with fewer AgNWs, stretching just over 10% leads to a break in electrical percolation due to the fracture of AgNW networks leading to the loss of conductivity. The dense network of AgNWs in PI/TPU/AgNW-500 is responsible for tolerating a large deformation without losing performance, despite the network fractures, the electrical connectivity is maintained by interconnected cracked structures. (Figures S8 and S9, Supporting Information).

We also assessed the resistance stability at different temperatures (Figure 2e,f). During the first heat processing, a reduction of resistance with temperature up to 100 °C was observed,

which we attribute to the thermal annealing of AgNWs and the resulting efficient contact of AgNWs at their junctions. In the second heating cycle, the resistance of both dual-sided nonwovens (PI/TPU/AgNW-500 and PI/TPU/AgNW-25) increased linearly with temperature increasing from room temperature to 160 °C, showing the metal-like behavior of electron transport as expected. The dual-sided nonwoven, PI/TPU/AgNW-500 even maintained a stable resistance for 1200 min at 250 °C (Figure 2g). PI/TPU/AgNW-500 also showed an excellent adhesion stability of AgNWs on PI nonwoven as seen in a washing test in soap water at 45 °C for 10 h in total (2 h for five times) (Figure 2h). PI/TPU/AgNW-500 maintained its low resistance after washing.
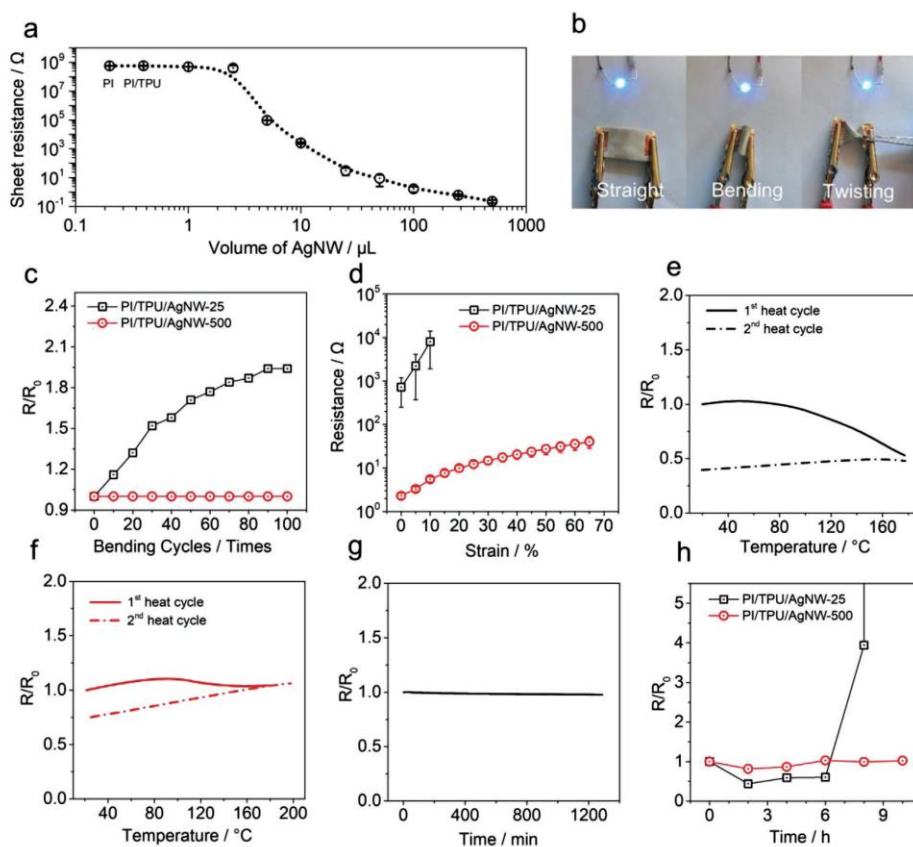
Figure 2. a) Sheet resistance of the dual-sided nonwovens prepared using different volumes of AgNW dispersion (17 g L^{-1}). PI and PI/TPU are labeled on the graphic without AgNWs for comparison. b) The luminance of LED bulb under different deformations of the dual-sided nonwoven. Resistance change of PI/TPU/AgNW-25 and PI/TPU/AgNW-500 on repeated c) bending cycles and d) different strain. e) The change of resistance of PI/TPU/AgNW-25 and f) PI/TPU/AgNW-500 upon temperature change. g) The change of resistance of PI/TPU/AgNW-500 at different time. h) The change of resistance of the dual-sided nonwoven after washing under different washing environments.

The PI/TPU/AgNW-500 demonstrated strong IR reflectance. The IR reflection performance of the samples was investigated by a setup, as depicted in **Figure 3**a and Figure S10, Supporting Information. The PI/TPU/AgNW-500 as a mirror in the mid IR range and, consequently, reflects thermal energy from a hot or cold source. This leads to a significant apparent temperature difference compared to PI (Figure 3b). Note that the exact determination of the absolute surface temperature of highly reflecting surfaces is very hard to conduct. We stress this fundamental issue in thermography by reporting an apparent temperature, which is merely a measure for the temperature of the surrounding environment than of the sample surface itself.

The IR reflectance of the dual-sided nonwoven depends on the AgNW concentration (Figure 3c), whereas the reflectance of PI side is constant at ≈30%. We then characterized the optical properties of PI/TPU/AgNW-500 and pure PI electrospun nonwoven in more detail, including reflectance, absorptance, and transmittance spectra (Figure 3d,f). The PI/TPU/AgNW-500 show ultralow IR transmittance of 0.2% regardless of their orientation, which is expected to provide passive heating by hindering the thermal exchange between the human body and the ambient environment.[19] A very significant difference in absorptance and reflectance of the two sides of the nonwovens, AgNW side, and PI side, was observed. The dual-sided
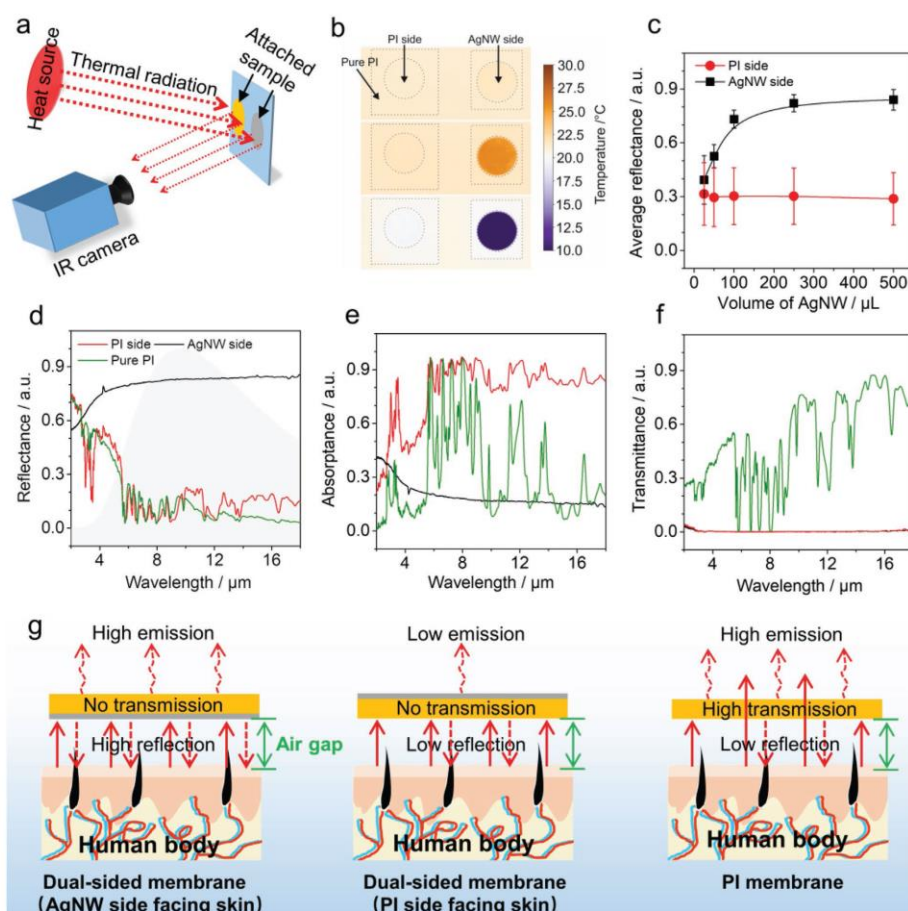
Figure 3. a) The schematic diagram of the setup for the measurement of IR reflection performance. b) Thermal images of IR reflection by dual-sided nonwoven (PI/TPU/AgNW-500). The AgNWs exhibited large apparent temperature difference compared to PI side. The first row: without hot/cold source; the second row: with hot source; the third row: with cold source. (Apparent temperature is defined as the temperature detected by IR camera without any correction) c) Average reflectance of a batch of dual-sided nonwovens with different amounts of AgNWs on the AgNW networks side and PI side. d) IR reflectance, e) absorptance, and f) transmittance of PI/TPU/AgNW-500 from another batch on the AgNW networks side and PI side. Gray area describes the major range of human body radiation. g) A schematic diagram of IR reflection by dual-sided nonwoven.

nonwoven exhibited low absorptance (19.5%) and high reflectance (80.3%) on the AgNWs side, and a high absorptance (78.5%) and low reflectance (21.1%) on the PI side. Compared to other AgNW coated textile, our nonwoven displayed a better IR reflection performance (Table S2, Supporting Information). We attribute this to the preparation procedure and the choice of AgNWs of appropriate length that allowed formation of flat and dense AgNW networks, reflecting most of IR irradiation as specular reflection and a minor portion as diffuse reflection.

On the contrary, PI electrospun nonwovens (reflectance: 17.9%; absorptance: 30.6%; transmittance: 51.5%) and other polymeric materials, such as conventional textile, paper, and polystyrene foam, show poor IR reflectance.[20]

Continuous IR radiation loss from the human body into the ambient surroundings is the central reason for body heat loss. Materials with high emissivity have been demonstrated to dissipate more heat from objects to the ambient environment.[21] A textile for on-demand thermal management needs to maintain

the thermal comfort of the body in different environments, regulating temperature as required. The dual-sided nonwoven introduced here, can be worn in two orientations. This will change the mutual radiative energy exchange between skin, fabric, and environment, as the emittance strongly depends on the fabric orientation. According to Kirchhoff's law absorption equals emission. Furthermore, emittance E can be calculated by:

$$E = 1 - R - T \qquad (1)$$

where R and T denote reflectance and transmittance, respectively. In the major range of human body radiation, a low emittance ($\approx$20%) on the AgNW side was observed (Figure S11, Supporting Information). In contrast, the PI side presented a quite high emittance of >75% on an average. Figure 3g summarizes the different radiative contributions that will affect the entire system skin, fabric, and environment. One can expect that the AgNW layer will lead to less thermal losses, either since the energy exchange skin-nonwoven (AgNW facing skin) or nonwoven-environment (AgNW facing environment) will be reduced. The optimum orientation will, however, also be influenced by heat conduction at the bottom side and thermal convection at the top surface.

To judge the optimum orientation of the dual-sided nonwoven for a passive warming application, we designed an experiment that closely resembles all contributions (radiative, conductive, and convective) to the heat exchange in this multibody system. We characterize the overall heat loss of a pure PI electrospun nonwoven compared to PI/TPU/AgNW-500 with a setup as depicted in **Figure** 4a. A black coated copper plate resembles the high emission of skin and is set to a temperature of 35 °C. A small heater controlled and measured the required power until a steady-state temperature was reached as shown in Figure 4b. The nonwoven was loosely placed on the copper plate to mimic wearing of a textile. The surrounding dome acts as the ambient environment with a high emissivity/absorptivity at a temperature of $\approx$22 °C. The required power for the steady-state condition for the two orientations of the dual-sided nonwoven, the pure PI, and a graphite coated reference are displayed as a function of dome temperature (ambient) in Figure 4c. For both, pure PI samples and the PI side of the PI/TPU/AgNW-500 facing the dome more power is needed to maintain a skin temperature of 35 °C compared to the AgNW side facing outward. This indicates that the PI side loses more heat by radiative heat transfer to the environment than the AgNW side. This is in agreement with the collected optical data presented in Figure 3d–f. The pure PI electrospun nonwoven and the PI side of the PI/TPU/AgNW-500 show higher absorptance and are consequently expected to emit more radiation than the AgNW side (Figure 4d). The differences between pure PI and the PI side of PI/TPU/AgNW-500 in the mid IR range (>10 μm) have apparently no significant influence on the overall heat exchange. Furthermore, blocking of direct IR transmission by the AgNW layer facing towards the skin and a concomitant reduced radiative heat exchange between skin and fabric seems to have no measurable effect. The power consumption is the same for pure PI and the dual-sided nonwoven in this configuration. Consequently, for a contribution to passive warming only the dual-sided nonwoven with the

AgNW facing to the outside will have an effect. Additionally, the PI electrospun nonwoven displayed a low thermal effusivity (88.1 W s$^{1/2}$ m^{-2} K^{-1}), which is comparatively low relative to other normal textiles (Figure 4e). Therefore, upon touching the skin the PI material will feel warm, suggesting that PI side facing towards skin (AgNW side facing towards outside) is the desirable wearing orientation.

A smart textile for thermal management needs to perform two functions: confining and providing heat to the human body for comfort. Thus, electric heating (active heating) usually is a popular and feasible way to offer extra thermal energy for warming a body. We, consequently, characterized the electrical heating performance of our dual-sided nonwovens by applying different direct currents. Electrical power (P) was distributed to the nonwoven by Joule heating according to Equation (2)

$$P = I^2 R \qquad (2)$$

where I is applied current, and R is resistance. We used an IR camera to detect the apparent surface temperature of the sample after applying different electrical currents, which is illustrated in **Figure** 5a. The dual-sided nonwoven PI/TPU/AgNW-25 presented a rapid increase of the apparent surface temperature from room temperature to the equilibrium state within 5 s (Figure 5b and thermal images in Figure S12, Supporting Information). The apparent temperature could even go as high as 230 °C (Figure 5b) on increasing the current to 0.37 A. On the other hand, PI/TPU/AgNW-500 merely produced any Joule heat even at high direct current (DC) currents (0.37 A), exhibiting surface temperature close to room temperature. Note, that these apparent temperatures are not corrected to the low emissivity of the AgNW surface and, consequently, should only be taken for a relative estimation of the temperature changes upon electrical heating.

In order to take advantage of both active Joule heating and low radiation losses, we have integrated a nonwoven as a heating electrode (PI/TPU/AgNW-25) and another as a radiation insulator (PI/TPU/AgNW-500) in the form of a double layer (Figure S13, Supporting Information). PI/TPU/AgNW-25 and PI/TPU/AgNW-500 stacked together act as a thermal management device for heat compensation (Figure 5c). The PI side of the double layer was towards the skin. The apparent temperature of the palm was around 37 °C. The temperature profile of the as-designed thermal management device is provided in Figure 5d. Already by applying 0.1 A current the apparent temperature loss due to the low emissivity of the AgNW top layer is compensated. As expected, the apparent surface temperature increases even further with a higher DC current. This result indicates our thermal management device has a prominent heating function combining passive heating and active electric heating.

3. Conclusion

In conclusion, we have successfully prepared a breathable and flexible dual-sided nonwoven with tailored electrical and thermal properties that are promising as smart textiles for personal thermal management. The dual-sided nonwoven consisting of PI electrospun nonwoven and AgNW networks,
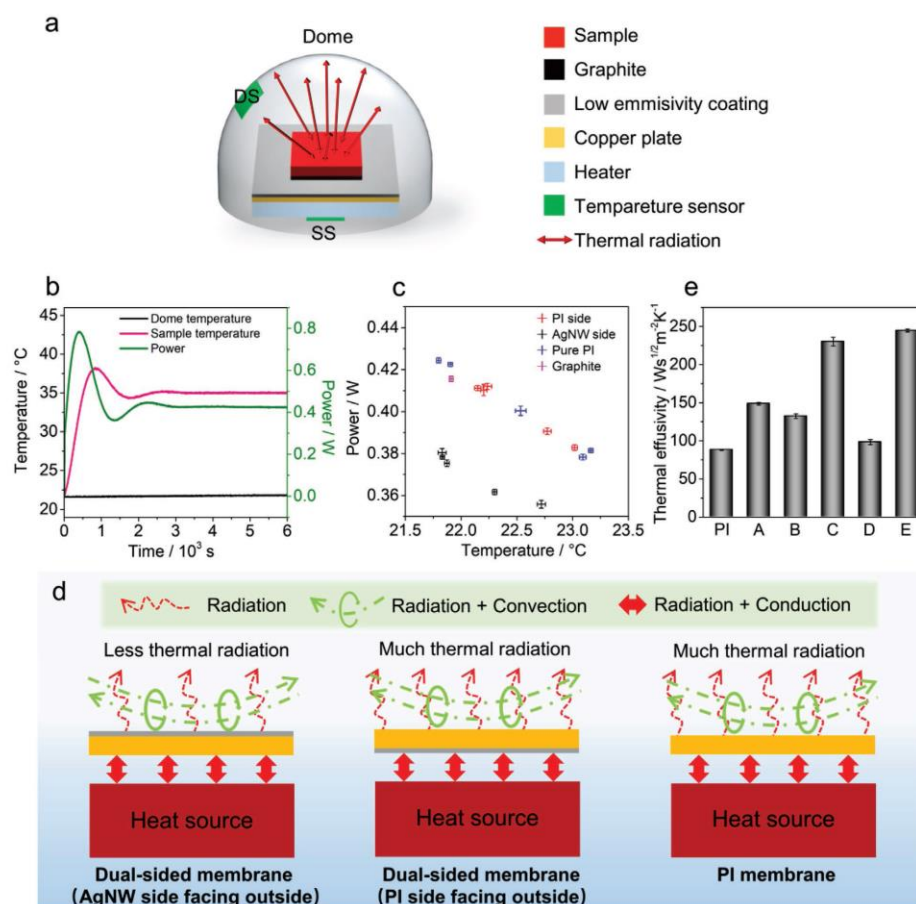
Figure 4. a) A schematic diagram of the setup for measuring radiatively dissipated energy. (SS: system sensor; DS: dome sensor) b) Evolution of dome temperature, sample temperature, and power supplied to the heater over time. c) Radiatively dissipated power for pure PI nonwoven, the respective sides of PI/TPU/AgNW-500, and a graphite reference as function of dome temperature (ambient). d) Schematic diagram of the thermal energy dissipation from PI/TPU/AgNW-500 and pure PI electrospun nonwoven. e) The effusivity of PI electrospun nonwoven and normal fabrics.[20] (PI: 35 layers of electrospun nonwoven, 10 g m^{-2} in each layer; A: 100% polyester, interlock knit fabric, 240 g m^{-2}; B: 100% polyester, interlock knit fabric, one side brushed, 255 g m^{-2}; C: 100% cotton, woven cotton duck fabric; D: 100% cotton, woven flannel fabric, 122 g m^{-2}; E: 100% cotton, woven poplin fabric, 180).

presented significant differences of physical, electrical, and thermal properties on the two sides, which could be tailored by using the amount of AgNW. More AgNW is prone to form dense AgNW networks, which possessed very low electrical resistance of 0.23 Ω sq^{-1} and excellent IR reflectance of more than 80%, far higher than the normal textiles. The dual-sided nonwoven with the AgNW facing to the outside demonstrated a

desirable effect for a contribution to passive warming. It could be integrated into a thermal management device by applying low current, realizing both functions of reducing heat dissipation to the ambient environment and Joule heating to the human body. Besides, the dual-sided nonwoven showed outstanding flexibility under different deformations as well as washing stability without sacrificing electrical resistance. Such

2108808 (7 of 10)

Figure 5. a) Schematic diagram of the smart textile for thermal management. The smart textile is composed of PI/TPU/AgNW-500 (top layer), to reduce thermal emissivity, and PI/TPU/AgNW-25 (bottom layer), to exhibit substantial Joule heating. b) Apparent surface temperature of PI/TPU/AgNW-25 heated by produced Joule heating with different current. (Black and red color represent PI/TPU/AgNW-25 and PI/TPU/AgNW-500 respectively.) c) Apparent surface temperature and d) corresponding thermal images of the thermal management device by the applied different current.

a dual-sided nonwoven can be used as a multifunctional flexible conductor and personal thermal management device to keep warm or smart textile escaping IR detection, which is very promising for next-generation wearable devices.

4. Experimental Section

Materials: PI electrospun nonwoven was kindly provided by Jiangxi Xiancai nanofiber Technology Co., Ltd. TPU (Desmopann DP 2590, Bayer Materials Science, Mn 88 900, Mw 145 000), ethylene glycol (p.a. ≥99.5%, Fluka), poly(vinylpyrrolidone) (PVP K30, Mw 40 000, Sigma-Aldrich), silver nitrate (AgNO$_3$, p.a. 99.9%, Sigma-Aldrich), iron chloride (FeCl$_3$, p.a. 98.0%, Sigma-Aldrich), sodium chloride (NaCl, p.a. 99.0%, Sigma-Aldrich), tetrahydrofuran (THF, distilled) were used as obtained. Other solvents were distilled before use. The AgNWs were synthesized by a solvent thermal method.[14b,c]

The preparation of dual-sided nonwoven: A piece of PI electrospun nonwoven (5 cm × 5 cm) was placed on a sand core funnel, followed by filtering AgNW aqueous dispersion through the PI nonwoven under vacuum assistance to obtain the PI/AgNW network. The used amount of AgNW is shown in Table S1, Supporting Information. Next, the dual-sided nonwoven was fabricated by filtering a TPU solution (2 mL, 8 wt%, in THF) through the PI/AgNW network under light vacuum to physically bond AgNWs strongly onto the PI nonwoven. At last, the resulted sample was naturally dried in the fume hood for 24 h. The relevant parameters used during different steps are tabulated in Table S3, Supporting Information.

The scanning electron microscopy (SEM) (Zeiss LEO1530, Jena, Germany) was employed for observing PI nanofibers and AgNW networks. Energy-dispersive X-ray spectroscopy (EDX) was performed by using a Zeiss Ultra Plas (Jena, Germany; 10 kV acceleration voltage).

Pore size distribution measurements were used to investigate pore size of the samples (Toper as standard test liquid with surface tension of 16.0 mN m^{-1}). The air permeability of the samples was measured by the Air Permeability Tester (FX 3300 LabAir IV, Switzerland) with the test area of 5 cm^2 under the pressure of 98 Pa. Each sample was measured five times at least, and the average value was taken. Tensile tester (Zwick/Roell BT1-FR 0.5TN-D14, Germany) was employed to characterize the mechanical property of samples. The samples (2 cm in length, 2 mm in width) were stretched at a speed of 10 mm min^{-1} (20 °C, pretension 0.01 N mm^{-1}). The thickness of samples was determined by a screw micrometer.

The washing test was performed by dipping the samples into 45 °C soap water (1 mL Manisoft detergent dissolved into 50 mL DI water) respectively with 100 rpm min^{-1} stirring for washing. The resistance of PI/TPU/AgNW-500 upon temperature and time was conducted with van der Pauw method. Sheet resistance was measured (Four-point measurements) with Keithley 2420 High-Current Source Meter coupled with Signatone SYS-301. Stretching resistance of different strain and cycling bending tests were performed by a tensile tester (Zwick/Roell BT1-FR 0.5TN-D14, Germany) to monitor stretching distance and bending degrees. An EMOS Multimeter (EM391) was connected by a copper conductor to detect the electrical resistance change of samples in different strain and bending cycles.

The IR reflection images were recorded by placing the samples in a cardbox enclosure. Images with a closed box and a hot or cold source above the camera were recorded (VarioCAM HD research 875/30 mm, Infratec) as shown in Figure 3a,b.

FTIR-spectroscopy measurements were conducted with an IR-spectrometer (Vertex 70, Bruker) in combination with a gold-coated integrating sphere accessory (A562, Bruker). The reflectance and transmittance were measured at the respective ports of the sphere. As reference a diffuse gold standard was used. The absorptance/emittance was calculated as Equation (1).

The radiative energy loss of the nonwoven was approximated with a steady-state heat transfer experiment. A circular sample piece with a

diameter of 3 mm was measured in a self-build setup. The sample was placed on a copper plate that was coated with graphite at the sample area and reflective aluminum foil at the outside, respectively. The copper plate was placed on a feedback-controlled heater and the power used to keep the sample at 35 °C (skin temperature) was recorded. The temperature sensor for the feedback control was in contact with the heater to record the sample temperature. The entire heater setup was placed within a block of expanded polystyrene to reduce heat losses by conduction to the surrounding. The heater block was placed below a graphite-coated aluminum dome with a diameter of 75 cm. The dome acts as a heat sink and was kept at ambient temperature during the experiment, which was monitored with a second temperature sensor. For a typical measurement, the sample was placed on the heater and the sample temperature, the dome temperature, and the heater power were monitored every 5 s until a steady state was reached. For each sample, the power and temperature data of 30 min in steady-state were averaged.

The thermal effusivity of the pure PI fabric was determined with a modified transient plane source instrument as described in the ASTM-D7984 standard.[22] Nonwoven pieces with a size of 5 × 5 cm are stacked to reach a sufficient overall thickness for the measurement. To eliminate the influence of any preferred orientation each layer was positioned with a rotation of 30° with respect to the previous layer. For the measurement, a thermal conductivity analyzer (TCi C-Therm, Canada) with a circular probe area of 1.75 cm² was used. During the measurement, a pressure of 10 N was applied to the stack to ensure good contact.

Different constant electrical currents of 0.05, 0.08, 0.13, 0.17, 0.35, and 0.37 A are applied by a DF-3010 DC power supply to investigate joule heating effect (1 cm × 3 cm, connected with copper cable). A TrueIR camera (Keysight U5856A) was employed to record the temperature of samples, and time-dependent joule heating was depicted by the Origin software.

The detailed preparation procedure of the thermal management device is shown in Figure S13, Supporting Information. The DF-3010 DC power supply was employed to provide constant currents. An IR camera was used to detected surface temperature as shown in Figure 5a.

Supporting Information

Supporting Information is available from the Wiley Online Library or from the author.

Conflict of Interest

The authors declare no conflict of interest.

Data Availability Statement

The data that supports the findings of this study are available in the supplementary material of this article.

[1] a) W. Weng, P. N. Chen, S. S. He, X. M. Sun, H. S. Peng, *Chem. Int. Ed.* **2016**, *55*, 6140; b) S. Liu, K. Ma, B. Yang, H. Li, X. Tao, *Adv. Funct. Mater.* **2021**, *31*, 2007254.

[2] a) X. Pu, W. X. Song, M. M. Liu, C. W. Sun, C. H. Du, C. Y. Jiang, X. Huang, D. C. Zou, W. G. Hu, Z. L. Wang, *Adv. Energy Mater.* **2016**, *6*, 1601048; b) C. Li, M. M. Islam, J. Moore, J. Sleppy, C. Morrison, K. Konstantinov, S. X. Dou, C. Renduchintala, J. Thomas, *Nat. Commun.* **2016**, *7*, 13319.

[3] Y. C. Peng, Y. Cui, *Joule* **2020**, *4*, 724.

[4] a) R. Hu, Y. D. Liu, S. Shin, S. Y. Huang, X. C. Ren, W. C. Shu, J. J. Cheng, G. M. Tao, W. L. Xu, R. K. Chen, X. B. Luo, *Adv. Energy Mater.* **2020**, *10*, 1903921; b) D. Y. Miao, X. F. Wang, J. Y. Yu, B. Ding, *Adv. Funct. Mater.* **2021**, *31*, 2008705.

[5] a) P. C. Hsu, A. Y. Song, P. B. Catrysse, C. Liu, Y. C. Peng, J. Xie, S. H. Fan, Y. Cui, *Science* **2016**, *353*, 1019; b) Y. C. Peng, J. Chen, A. Y. Song, P. B. Catrysse, P. C. Hsu, L. L. Cai, B. F. Liu, Y. Y. Zhu, G. M. Zhou, D. S. Wu, H. R. Lee, S. H. Fan, Y. Cui, *Nat. Sustain.* **2018**, 105.

[6] a) P. C. Hsu, C. Liu, A. Y. Song, Z. Zhang, Y. C. Peng, J. Xie, K. Liu, C. L. Wu, P. B. Catrysse, L. L. Cai, S. Zhai, A. Majumdar, S. H. Fan, Y. Cui, *Sci. Adv.* **2017**, *3*, 1700895; b) L. L. Cai, A. Y. Song, P. L. Wu, P. C. Hsu, Y. C. Peng, J. Chen, C. Liu, P. B. Catrysse, Y. Y. Liu, A. K. Yang, C. X. Zhou, C. Y. Zhou, S. H. Fan, Y. Cui, *Nat. Commun.* **2017**, *8*, 496.

[7] Y. Lu, X. D. Xiao, J. Fu, C. M. Huan, S. Qi, Y. J. Zhan, Y. Q. Zhu, G. Xu, *Chem. Eng. J.* **2019**, *355*, 532.

[8] Y. Cui, H. X. Gong, Y. J. Wang, D. W. Li, H. Bai, *Adv. Mater.* **2018**, *30*, 1706807.

[9] P. C. Hsu, X. G. Liu, C. Liu, X. Xie, H. R. Lee, A. J. Welch, T. Zhao, Y. Cui, *Nano Lett.* **2015**, *15*, 365.

[10] A. Hazarika, B. K. Deka, D. Kim, H. E. Jeong, Y. B. Park, H. W. Park, *Nano Lett.* **2018**, *18*, 6731.

[11] S. H. Jiang, J. Y. Cheong, J. S. Nam, I. D. Kim, S. Agarwal, A. Greiner, *ACS Appl. Mater. Interfaces* **2020**, *12*, 19006.

[12] a) F. Zhang, Y. Y. Feng, M. M. Qin, L. Gao, Z. Y. Li, F. L. Zhao, Z. X. Zhang, F. Lv, W. Feng, *Adv. Funct. Mater.* **2019**, *29*, 1901383; b) H. L. Li, S. C. Dai, J. Miao, X. Wu, N. Chandrasekharan, H. X. Qiu, J. H. Yang, *Carbon* **2018**, *126*, 319.

[13] Y. Wang, W. Wang, X. D. Ding, D. Yu, *Chem. Eng. J.* **2020**, *380*, 122553.

[14] a) S. H. Jiang, S. Reich, B. Uch, P. Hu, S. Agarwal, A. Greiner, *ACS Appl. Mater. Interfaces* **2017**, *9*, 34286; b) Q. Gao, B. A. F. Kopera, J. Zhu, X. J. Liao, C. Gao, M. Retsch, S. Agarwal, A. Greiner, *Adv. Funct. Mater.* **2020**, *30*, 1907555; c) S. Reich, M. Burgard, M. Langner, S. H. Jiang, X. Q. Wang, S. Agarwal, B. Ding, J. Y. Yu, A. Greiner, *npj Flexible Electron.* **2018**, *2*, 5.

[15] a) J. W. Lee, S. Jung, T. W. Lee, J. Jo, H. Y. Chae, K. Choi, J. J. Kim, J. H. Lee, C. Yang, J. M. Baik, *Adv. Energy Mater.* **2019**, *9*, 1901987; b) L. Dhakar, P. Pitchappa, F. E. H. Tay, C. Lee, *Nano Energy* **2016**, *19*, 532; c) J. Chen, Z. L. Wang, *Joule* **2017**, *1*, 480.

[16] a) F. C. Li, Y. Liu, X. L. Shi, H. P. Li, C. H. Wang, Q. Zhang, R. J. Ma, J. J. Liang, *Nano Lett.* **2020**, *20*, 6176; b) H. J. Kim, K. Sim, A. Thukral, C. J. Yu, *Sci. Adv.* **2017**, *3*, e1701114; c) J. Kim, M. Kim, M. S. Lee, K. Kim, S. Ji, Y. T. Kim, J. Park, K. Na, K. H. Bae, H. K. Kim, F. Bien, C. Y. Lee, J. U. Park, *Nat. Commun.* **2017**, *8*, 14997; d) S. S. Yao,

P. Ren, R. Q. Song, Y. X. Liu, Q. J. Huang, J. Y. Dong, B. T. O'Connor, Y. Zhu, *Adv. Mater.* **2020**, *32*, 1902343; e) J. K. Han, J. K. Yang, W. W. Gao, H. Bai, *Adv. Funct. Mater.* **2021**, *31*, 2010155.

[17] S. Cho, S. Kang, A. Pandya, R. Shanker, Z. Khan, Y. Lee, J. Park, S. L. Craig, H. Ko, *ACS Nano* **2017**, *11*, 4346.

[18] a) X. W. Liang, T. Zhao, W. Jiang, X. C. Yu, Y. G. Hu, P. L. Zhu, H. R. Zheng, R. Sun, C. P. Wong, *Nano Energy* **2019**, *59*, 508; b) F. Liang, X. J. Zhao, H. Y. Li, Y. J. Fan, J. W. Cao, Z. L. Wang, G. Zhu, *Nano Energy* **2020**, *69*, 104414; c) Z. Li, Q. Zheng, Z. L. Wang, Z. Li, *Research (Wash D C)* **2020**, *2020*, 8710686.

[19] a) L. L. Cai, A. Y. Song, W. Li, P. C. Hsu, D. C. Lin, P. B. Catrysse, Y. Y. Liu, Y. C. Peng, J. Chen, H. X. Wang, J. W. Xu, A. K. Yang, S. H. Fan, Y. Cui, *Adv. Mater.* **2018**, *30*, 1802152; b) X. A. Zhang,

S. Yu, B. Xu, M. Li, Z. Peng, Y. Wang, S. Deng, X. Wu, Z. Wu, M. Ouyang, *Science* **2019**, *363*, 619.

[20] a) Y. Lian, H. Yu, M. Wang, X. Yang, Z. Li, F. Yang, Y. Wang, H. Tai, Y. Liao, J. Wu, *J. Mater. Chem. C* **2020**, *8*, 8399; b) X. Yue, T. Zhang, D. Yang, F. Qiu, Z. Li, G. Wei, Y. Qiao, *J. Colloid Interface Sci.* **2019**, *535*, 363.

[21] T. Li, Y. Zhai, S. M. He, W. T. Gan, Z. Y. Wei, M. Heidarinejad, D. Dalgo, R. Y. Mi, X. P. Zhao, J. W. Song, J. Q. Dai, C. J. Chen, A. Aili, A. Vellore, A. Martini, R. G. Yang, J. Srebric, X. B. Yin, L. B. Hu, *Science* **2019**, *364*, 760.

[22] ASTM D7984-16, *Standard Test Method for Measurement of Thermal Effusivity of Fabrics Using a Modified Transient Plane Source (MTPS) Instrument*, ASTM International, West Conshohocken, PA **2016**.

108

WILEY-VCH

Supporting Information

Breathable and flexible dual-sided nonwovens with different infrared optical performances for smart textile

Qiang Gao,[1] Tobias Lauster,[2] Bernd A. F. Kopera,[2] Markus Retsch,[2,3]* Seema Agarwal,[1]* Andreas Greiner[1]*

[1]Q. Gao, S. Agarwal, A. Greiner
Department of Chemistry, Macromolecular Chemistry II and Bavarian Polymer Institute
University of Bayreuth
Universitätsstrasse 30, 95440 Bayreuth, Germany
E-mail: markus.retsch@uni-bayreuth.de; agarwal@uni-bayreuth.de; greiner@uni-bayreuth.de

[2] T. Lauster, B. A. F. Kopera, M. Retsch
Department of Chemistry, Physical Chemistry I
University of Bayreuth
Universitätsstrasse 30, 95440 Bayreuth, Germany

[3] M. Retsch
Bavarian Center for Battery Technology (BayBatt), Bavarian Polymer Institute, and Bayreuth
Center for Colloids and Interfaces
University of Bayreuth
Universitätsstrasse 30, 95440 Bayreuth, Germany

WILEY-VCH

Supplementary figures:
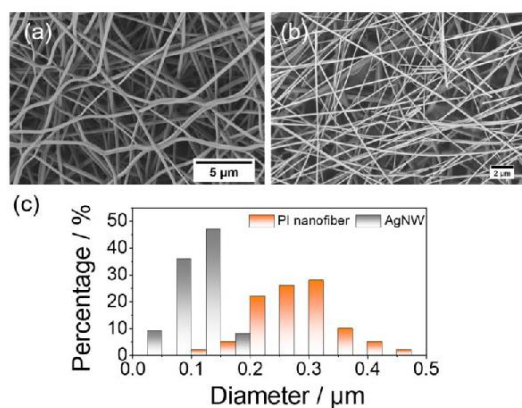
Figure S1 (a) SEM image of PI electrospun nanofiber. (b) SEM image of AgNW mesh prepared by the wet-laid method. (c) Diameter distribution of PI nanofiber and AgNW measured with ImageJ software (100 measurements were selected randomly).
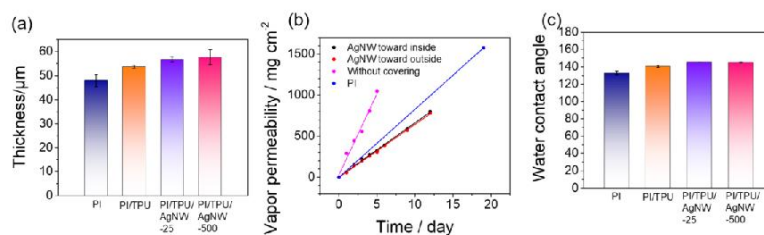
Figure S2 (a) Thickness of PI nonwoven, PI/TPU nonwoven, PI/TPU/AgNW-25, and PI/TPU/AgNW-500. (b) Vapor permeability of the dual-sided nonwoven of PI/TPU/AgNW-500. (c) Water contact angles of PI nonwoven, PI/TPU nonwoven, PI/TPU/AgNW-25, and PI/TPU/AgNW-500.

2

Figure S3 Optical images of water contact angle on nonwovens. PI, PI/TPU, PI/TPU/AgNW-25, and PI/TPU/AgNW-500 were hydrophobic, on which water drop could keep the shape. PI /AgNW-25 and PI /AgNW-500 were hydrophilic, through which water drop could penetrate easily.
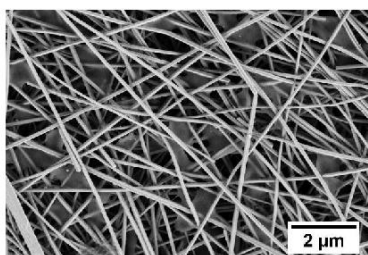
Figure S4 Original SEM image of AgNW networks with TPU.
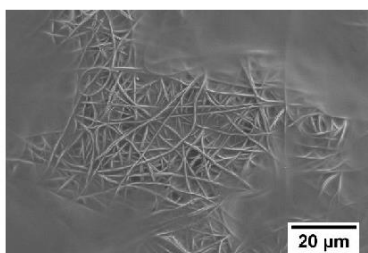
Figure S5 SEM image of TPU casted PI electrospun nonwoven.

3
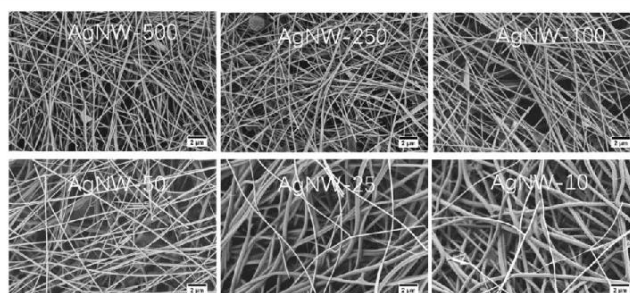
Figure S6 SEM image of the dual-sided nonwoven with different amounts of AgNW.
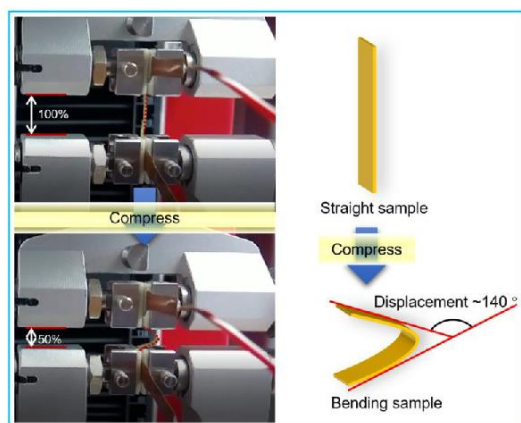
Figure S7 Measurement of 100-time bending test and schematic displacement of dual-sided nonwoven during compressing test.

4
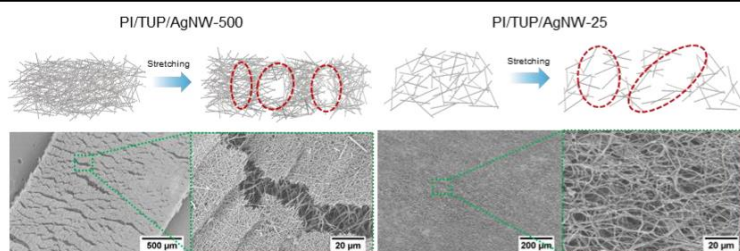
Figure S8 Schematic diagram (up) and SEM image (down) of cracks on AgNW mesh by stretching. Cracks on the AgNW networks of PI/TPU/AgNW-500 appeared by stretching, but AgNW still composed interconnected mesh structure. However, less AgNW cannot maintain the integrated AgNW mesh of PI/TPU/AgNW-25 when stretching, caused to electrical resistance dramatically increase.
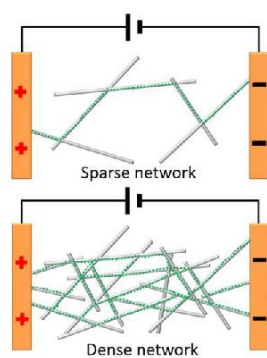
Figure S9 The mechanism of resistance stability of dense AgNW networks.

5

WILEY-VCH
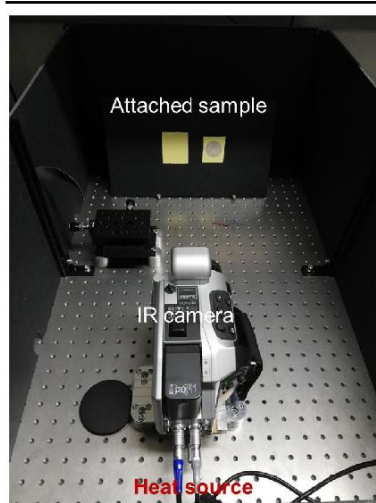
Figure S10 The digital image of the setup for the measurement of IR reflection performance.
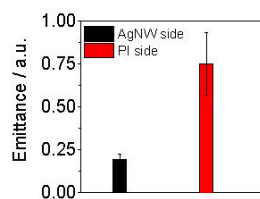
Figure S11 The emittance of PI/TPU/AgNW-500 on AgNW side and PI side.

6
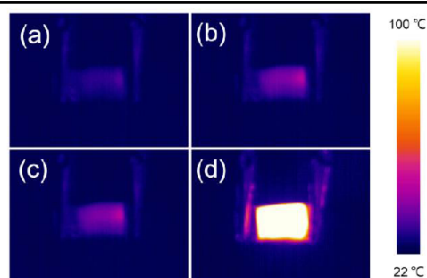
Figure S12 Thermal images of PI/TPU/AgNW-25 with applying different current. (a) 0.05A; (b) 0.13A; (c) 0.17A; (d) 0.35A.
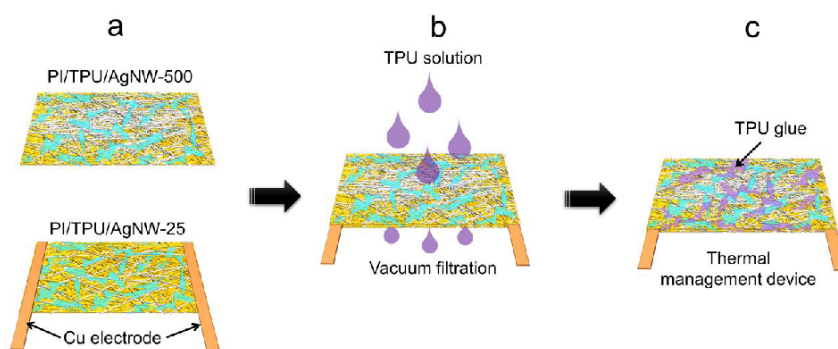
Figure S13 The schematic diagram of the thermal management device. (a) Two dual-sided nonwovens containing different amounts of AgNWs (the top PI/TPU/AgNW-500 for reducing emissivity and the bottom PI/TPU/AgNW-25 for heat compensation) were stacked as shown. Two Cu tapes were used as the electrode, attaching to the AgNW networks of PI/TPU/AgNW-25. (b) Well-stacked PI/TPU/AgNW-500 and PI/TPU/AgNW-25 were filtered 2mL TPU solution under a light vacuum to glue dual nonwovens together in case of delamination. (c) The resulted thermal management device is with tightly bonded double layers of PI/TPU/AgNW-500 and PI/TPU/AgNW-25 after drying.

7

Supplementary tables:

Table S1 Electrical resistance of dual-sided nonwoven with different amount of AgNW

Sample	Used AgNW(17 g L^{-1}) / μL	Content of AgNW / (g m^{-2})	Sheet resistance / Ω sq^{-1}
PI	0	-	5.7×10^8
PI/TPU	0	-	5.8×10^8
PI/TPU/AgNW-1	1	0.017	4.9×10^8
PI/TPU/AgNW-2.5	2.5	0.0425	4.8×10^8
PI/TPU/AgNW-5	5	0.085	9.55×10^4
PI/TPU/AgNW-10	10	0.17	2.54×10^3
PI/TPU/AgNW-25	25	0.425	30.7
PI/TPU/AgNW-50	50	0.85	9.1
PI/TPU/AgNW-100	100	1.7	1.7
PI/TPU/AgNW-250	250	4.25	0.6
PI/TPU/AgNW-500	500	8.5	0.2

WILEY-VCH

Table S2 IR reflectance of the dual-sided nonwoven versus previous Ag coated textiles

Sample	Material	Reflectance	ref
Laminated Nanofiber Membrane	Ag/cellulose/carbon nanotube	0.7 (2 - 18 μm)	1
multifunctional E-textile	Cotton/AgNW	0.59 (2 - 16 μm)	2
Metallic nanowire cloth	Cotton/AgNW	0.4 (2 - 15 μm)	3
Normal cloth	Cotton	0.01 (2 - 15 μm)	3
PI nonwoven	PI	0.44 (2 - 18 μm)	**This work**
PI/TPU/AgNW-500	PI/TPU/AgNW	>0.8 (2 - 18 μm)	**This work**

9

WILEY-VCH

Table S3. The relevant parameters of PI nowoven, TPU solution and AgNW dispersion used for the preparation of dual-sided membrane

Relevant parameter		Value
PI nonwoven	Fiber diameter /μm	0.30 ± 0.07
	Pore size / μm	1.7
	Thickness /μm	48.0 ± 2.5
	Air permeability / mm s^{-1}	20.3 ± 0.5
	Water contact angle / degree	140
TPU solution	Solvent	THF
	Concentration / wt%	8
	Used amount / mL	2
AgNW aqueous dispersion	Diameter of AgNW / μm	0.10 ± 0.03
	Length of AgNW /μm	20-60
	Concentration of dispersion / g L^{-1}	17
	Used amount / μL	X (See Table S1)

References

1. X. Yue, M. He, T. Zhang, D. Yang, F. Qiu, ACS Appl. Mater. Inter. **2020**, 12, 12285.

2. Y. L. Lian, H. Yu, M. Y. Wang, X. N. Yang, Z. Li, F. Yang, Y. Wang, H. L. Tai, Y. L. Liao, J. Y. Wu, X. R. Wang, Y. D. Jiang, G. M. Tao, J. Mater. Chem. C **2020**, 8, 8399.

3. P. C. Hsu, X. G. Liu, C. Liu, X. Xie, H. R. Lee, A. J. Welch, T. Zhao, Y. Cui, Nano lett. **2015**, 15, 365.

10

Ultralight heat-insulating, electrically conductive carbon fibrous sponges for wearable mechanosensing devices with advanced warming function

Qiang Gao, Thomas Tran, Xiaojian Liao, Sabine Rosenfeldt, Chao Gao, Haoqing Hou, Markus Retsch, Seema Agarwal*, Andreas Greiner*

1

ABSTRACT: Ultralight highly porous sponges are attractive for electronic devices due to superelasticity, outstanding resilience, and thermal insulation. However, fabricating an ultralight conductive sponge with low thermal conductivity, mechanical flexibility, and piezoresistivity, as well as adjustable heating behavior, is still a challenge. Here, an ultralight carbon nanofibrous sponge fabricated by pyrolyzing a graphene oxide coated polyimide sponge is reported. The resulting carbon sponge demonstrates a high electrical conductivity of 0.03 - 4.72 S m^{-1} and a low thermal conductivity of 0.027 - 0.038 W m^{-1} K^{-1} (20 °C, in ambient air), as well as a low density to ~6 mg cm^{-3}. Additionally, the sponge exhibits mechanical flexibility, stability, excellent piezoresistivity, and an adjustable heating behavior. Hence, it could be utilized as a sensing device, including thermal management making them promising for use in smart sportswear, human-machine interfaces, and wearable healthcare devices.

1. INTRODUCTION

Wearable electronics are essential for the realization of human-robot interactions, healthcare monitoring, and an individual's physical activity detection.[1-5] Specifically, wearable mechnosensors[6-8], transferring a mechanical trigger (e.g., pressure, strain, and friction) into detectable electronic units (e.g., resistance, current, voltage, or capacitance), have attracted considerable attention. Recently, a large number of conductive composite elastomers composed of novel conductive materials, e.g., graphene, MXene, carbon nanotubes, metal nanowires, carbon black, and elastic substrates, such as polyurethane and polydimethylsiloxane, are reported for sensing applications[9-12]. Even if these materials are often used in flexible electronics, their large

2

120

weight limits their application in wearable sensing devices, for example, in smart sportswear. Today, most wearable sensing devices provide a single sensing function, but demand for multifunctional wearable devices increases[13-15]. For devices that monitor physical activity and provide thermotherapy at the same time, a tunable combination of device weight, electrical, and thermal conductivity is interesting[16]. Therefore, the development of suitably conductive but ultralight materials is crucial.

Ultralight polymeric sponges, such as polyimide (PI) fibrous sponges, combine the advantageous features of ultralow density, high specific surface area, hierarchical pore structure, desirable mechanical robustness and flexibility, and prominent thermal insulation performance. Such sponges have been widely investigated for biological, environmental, biomedical, energy, and electronics applications[17-19]. However, their inherent insulating nature restricts the application as an electrically active element. The conductivity of polymeric sponges is improved by the addition of conducting material (e.g., nanocarbon, nano metal, or a conducting polymer).[20] The introduction of a large amount of conducting additive increases its thermal conductivity and bulk density[21-22] but decreases portability and thermal insulation. Advanced graphene and carbon nanotube aerogels[23-25] have good electrical conductivity, low thermal conductivity, high mechanical flexibility, as well as an ultralow weight, making them potential materials for applications in flexible electronics. However, the high preparation cost of the carbon precursor limits their widespread application.[26] Porous carbon sponges derived from synthesized polymeric materials[27-28] or natural sources[29-30] have demonstrated an ultralow weight and good electrical conductivity. Still, the degradation of mechanical properties induced by the pyrolysis process, especially decreased flexibility and compression resilience, cannot meet the requirements for wearable devices, as they often face diverse deformations when worn. Recently, it has been demonstrated

3

that the addition of graphene can enhance the mechanical stability of carbon sponges.[31] However, current graphene modified nanofiber assemblies usually demonstrated sever issue of poor distribution of graphene caused by the size mismatch between sheet-type coating materials and pores of the substrates.[32-33]

Herein, we report ultralight, 3D carbon sponges (CSs) derived from electrospun PI fibers coated with graphene oxide (GO). Our coating-fabrication strategy (first coating short fibers with GO and followed assembling into sponge using coated short fibers) instead of commonly used fabrication-coating method (directly coating as-prepared sponge with GO) solves the issue of inhomogeneous distribution of large size sheet materials in the electrospun fiber assemblies. The resultant CS exhibits a unique characteristic of good electrical conductivity (0.03 - 4.72 S m^{-1}) and high thermal insulation performance (0.027 - 0.038 W m^{-1} K^{-1}), which is difficult to be simultaneously obtained in current natural and synthetic materials. The CS exhibits physically robust and mechanically stable properties under multi compression deformations. Since the electrical conductivity highly depends on compression strain, these CSs are suited for ultilzing as wearable piezoresistive sensors to detect physical movements of human body in real-time. The thermal insulation is due to the carbon compounds and high porosity of our material. Good thermal insulation allows maintaining temperature very well. Additionally, remaining heat losses can be compensated by Joule heating, which can be controlled by the working voltage as well as the compression strain since our material shows piezoresistivity. Comparing to the conventional heating mode controlled by input voltage, the strain dependent heating is demonstrated an economic heating mode, due to more heat production by using a low voltage. Such an advanced heating function based on piezoresistivity offers another feasible way of tuning temperature of flexible heating devices. The low density (6 - 30 mg cm^{-3}) allows the application as an ultralight device. The unique combined superiorities of

4

ultralow density, excellent flexibility, strain-dependent electrical and thermal properties make the CSs extremely promising for future applications in wearable devices with heating functionality and other types of flexible electronics.

2. EXPERIMENTAL SECTION

2.1 Materials

Polyimide (PI) electrospun nonwoven was supplied by Jiangxi Xiancai nanofiber Technology Co. Ltd. Graphene oxide (GO) was given by Hangzhou Gaoxi Technology Co. Ltd. Polyurethane (PU) was synthesized using a previously published procedure[34]. Tetrahydrofuran (THF, $\geq$ 99.5%, Fisher Scientific) and 2-propanol were distilled before use. Deionized water (18.2 MΩ cm) was taken from a Millipore-Q Plus purification system (Merck Millipore, Merck KGaA, Darmstadt, Germany).

2.2 Preparation of CS

As depicted in **Figure 1a**, the first step (step 1) in the preparation of the sponge is to make PI short fibers (SFs) by mechanical cutting. In detail: 10 g of PI fiber nonwovens were cut by scissors and then transferred into 1 L of a water/isopropanol mixture (1:1, v/v) and cooled down with liquid nitrogen until the suspension formed a paste. In this frozen state, the paste was shredded by a mixer (Robot Coupe Blixer 4, Rudolf Lange GmbH & Co. K) at 4000 rpm for 10 min to obtain a PI SF dispersion. Dried PI SF powders were obtained by Freeze-drying for 48 h. The freeze-dried PI SFs had a length of L = 88.6 ± 52.1 μm and an average diameter of d = 454.5 ± 114.3 nm. The average length was calculated with ImageJ software by randomly selecting 50 SFs in the optical images, and the average diameter was calculated by randomly selecting 100 positions of fibers in the SEM images. In step 2, 1 g of PI SFs was dispersed in 100 mL of PU solution (1 wt%, in THF). The

5

suspension was shaken by hand for 5 min. Then, the dispersion was filtered through a polyethylene terephthalate (PET) mesh (pore size 50 μm) to remove the extra PU solution. The filtered SFs were washed with water several times to obtain PU-coated SFs, designated as PIPU SF. In step 3, PIPU SFs were mixed with superfluous GO dispersion (0.05 mg mL^{-1}, in water). The suspension with PIPU SFs was shaken by hand for 5 min to shake off non-immobilized GO platelets. Afterward, the GO-coated PIPU SFs were taken out of the dispersion and freeze-dried for 48 h, named as PIPUGO SF. In step 4, 100 mg PIPUGO SFs were dispersed in 10 mL of dioxane and freeze-dried for 48 h to obtain a PIPUGO sponge. Note that the difference between step 3 and step 4 is that the PIPUGO SFs resulting from step 3 is the raw material to prepare the sponge. The PIPUGO sponges (step 4) possessed fixed density and shape as a requirement. In step 5, the PIPUGO sponges were carbonized by thermal treatment by heating from room temperature to 1000 °C (heating rate of 5 K min^{-1}) and maintaining this temperature for 1 h in a nitrogen atmosphere. Afterward, the carbonized sample was cooled to room temperature. The obtained sample was designated as CS. Note that except when stated otherwise, the GO content of CS used in this work is always 7 wt%, and the density of CS is 10.6 mg cm^{-3}.

2.3 Analytical instruments and characterization methods

An SEM (Zeiss LEO 1530, Jena, Germany; Schottky field emission cathode) was employed to observe fiber morphology and fiber networks in the sponges. Transmission Electron Microscopy (TEM) images were obtained on a ZEISS EM922 Omega microscope at an acceleration voltage of 200 keV. The fibers were collected with a copper grid for observation. Sheet resistance was investigated using a four-point measurement method using a Signatone SYS-301 coupled with a Keithley 2420 high-current source meter. Five measurements were carried out for each sample. X-ray diffraction (XRD) was recorded using Bragg-Brentano-geometry on an Empyrean

6

diffractometer (PANalytical B.V.; the Netherlands) using Cu K_α radiation (λ = 1.54187 Å). The samples were placed on glass slides (Menzel-Gläser; Thermo Scientific). The raw data are shown as they are.

XPS was performed with a Physical Electronics PHI VersaProbe III - Scanning XPS Microprobe, equipped with a monochromatic aluminum K-alpha source. The measurements were done as survey scans without sputtering using a pass energy of 224 eV. Data evaluation was performed by the software provided by the instrument.

Raman spectrum was performed on an Alpha 300 RA+ imaging system (WiTEC, 2016), equipped with a UHTS 300 spectrometer and a back-illuminated camera (Andor Newton 970 EMCCD). The measurements were conducted at an excitation wavelength of λ = 532 nm, using a laser power of 0.2 mW and an integration time of 0.5 s $pixel^{-1}$ (Zeiss EC Epiplan-Neofluar Dic 100x / 0.9, step size 100 nm $pixel^{-1}$, software WITec Control FIVE 5.3). All spectra were subjected to a cosmic ray removal routine and baseline correction.

The compression tests and the cyclic compression tests were performed on a tensile tester (ZwickiLine Z0.5; BT1-FR0.5TN. D14; Zwick/Roell, Germany) coupled with a 20 N sensor at a compression rate of 50 mm min^{-1}.

The bulk electrical resistance (R) was measured with a Signatone SYS-301 coupled with a Keithley 2420 high-current source meter in a two-probe configuration. The sample was inserted between two copper plates. The distance between the plates was adjusted. The electrical conductivity (σ) was calculated according to the following relations:

$$R = \rho L/S \tag{1},$$

$$\rho = RS/L \tag{2},$$

$$\sigma = 1/\rho = L/RS \tag{3},$$

7

where ρ, L, S, are the electrical resistivity, the length, and the cross-section area of the sample, respectively.

An LED was connected into a circuit powered by a DF-3010 DC power source with a fixed strain sample, which was inserted between copper electrodes as mentioned above in the resistance measurement. The resistance during cycling compression tests was recorded by a digital multimeter (EMOS Multimeter EM391).

The CS sensor was assembled with two strips of perfluoroalkoxy alkane films (1 cm $\times$ 10 cm, the thickness of 9.8 $\pm$ 1 μm). A CS was connected with copper wires, fixed by a layer of aluminum tape on the top and bottom surface. Sensing performances were measured with a digital multimeter (Keithley 2700), facilitating the constant-current method with 2 copper wires. All parameters were set to the default values (auto range, 0.1 s integration time).

Joule heating was investigated by inserting a sponge between copper electrodes, by different DC voltages, and with different fixed strains. The apparent temperature was recorded by a Keysight U5856A IR camera, and the software of Keysight TrueIR Analysis and Reporting Tool was used to analyze IR thermal graphs.

The thermal conductivity of the sponge was characterized by HotDisk Thermal Constants Analyzer (TPS 2500s) coupled with a Kapton sensor (HotDisk C5465). The applied heating time and heating powers were 10 s and 5 mW, respectively. The measurements took place 5 times, with 20 min intervals between each measurement.

3. RESULTS AND DISCUSSION

The fabrication procedure of CS is illustrated in **Figure 1a**. A more detailed description is given in the experiment section (Supplementary material). The procedure starts with the preparation of

8

electrospun PI short fibers (SFs) by mechanical cutting of long, as-spun fiber nonwovens (step 1) followed by coating with cationic polyurethane (PU) (step 2) and graphene oxide (GO) (step 3), freeze-drying (step 4), and carbonization (step 5). The PI SFs (after step 1) had a length of 89 ± 52 µm (**Figure S1**) and a diameter of 455 ± 114 nm. Since the surfaces of GO and PI are both negatively charged, covering the PI SFs with a thin layer of cationic PU (step 2) is obligatory to guarantee a strong interaction between the fiber backbone and GO. The scanning electron microscopy (SEM) image (**Figure S2**) of the PU modified PI SFs (PIPU SFs, PU content 3.4 ± 1.3 wt%, step 2) revealed a homogeneous fiber surface with an average fiber diameter of 552 ± 200 nm. The thin PU layer was investigated by small-angle X-ray scattering (SAXS) and a simple shake test. (**Figures S3, S4** and the description there). In step 3, the PIPU SFs were immersed in a GO dispersion (0.05 mg ml^{-1}, in water). The exfoliated GO with a lateral size of approximately 20 µm and a thickness of only 1 nm (**Figure S5**) wrapped around the PIPU fiber (PIPUGO SF in **Figure 1b**), which we explain with the high bending flexibility of GO and effective electrostatic interaction between the cationic (PU) and acid (GO) functional groups. Apart from the strong electrostatic interaction, hydrogen bonds between PU and GO is another vital interaction for the GO surface modification. The transmission electron microscopy (TEM) (**Figure 1c**) investigation of the surface layer of PIPUGO SF (diameter: 586 ± 265 nm, PIPU: GO ratio was 93:7 w/w) revealed a rough surface due to immobilized GO nanosheets. The wrinkles (**Figure 1d**) are probably caused by compressive stress as a consequence of the volume shrinkage of the former solvent swollen PU-layer, as well as folds and cracks to counteract the repulsive interaction between equal charges of functional groups in GO. The fact that the surface of PIPUGO SF exhibits even more wrinkles after thermal treatment (**Figure 1e**) strengthens this hypothesis. After sponge formation by freeze-drying (step 4), PIPUGO sponges with fixed shape and density were

9

obtained. In the last step of the fabrication (step 5), the electrical conductivity needed for the piezoresistive behavior is introduced by thermal treatment, and the final sample was designated as CS. Therefore, the PIPUGO sponge (electric conductivity $< 10^{-7}$ S m^{-1}) is heated to 1000 °C in a nitrogen atmosphere to partially restore the aromatic graphene structure. An electric conductivity of 0.85 ± 0.03 S m^{-1} was measured for the resulting CS and a reduced fiber diameter of 445 ± 148 nm due to the mass loss and release of gases like CO, CO_2, CH_4, and N_2 during the pyrolysis process was obtained.[35] After carbonization, the CS presented the typical black color (**Figure 1f**) of carbon materials and showed shrinkage of ~ 14.6% in volume compared to the PIPUGO sponge (yellow color). The CS had a porosity of 99.7% and showed a typical cellular porous structure and homogeneous graphene coating on the surface of the fibers (**Figure S6**). The relevant properties of CS and PIPUGO sponge are shown in **Table 1**.

10
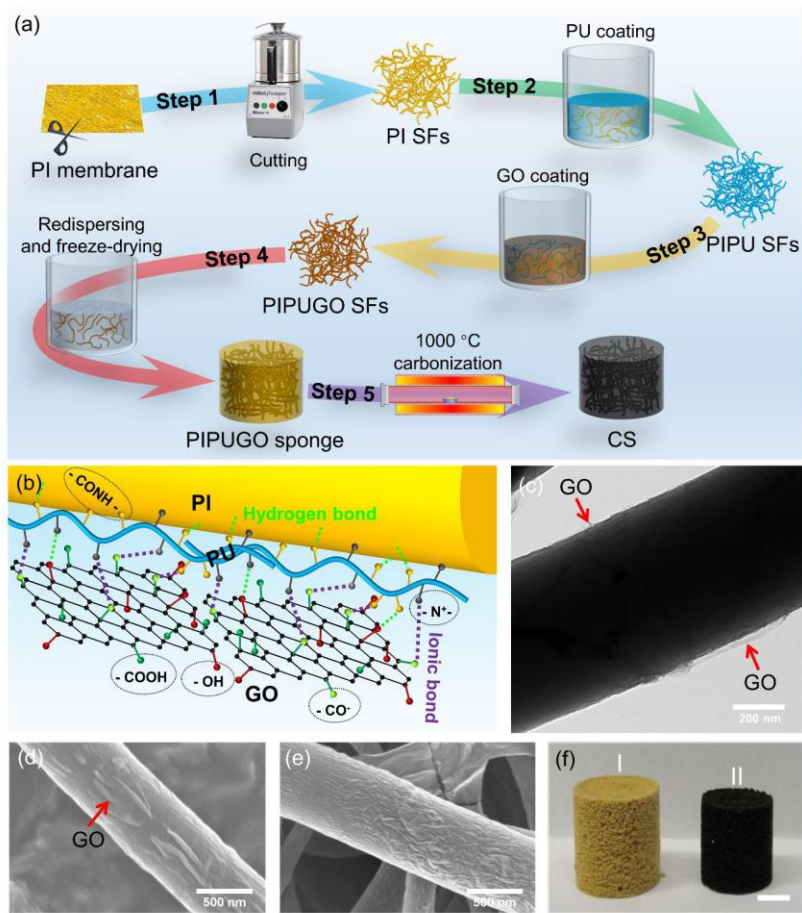
Figure 1. (a) The fabrication procedure of CS. (b) The mechanism of surface interactions for the assembly of PIPUGO SF. Color code: PI yellow, PU blue, and GO black. (c) TEM and (d) SEM images of PIPUGO SF. (e) SEM image of PIPUGO fiber after carbonization. (f) Digital images of the resulting PIPUGO sponge (I) and CS (II). Scale bar 1 cm.

Table 1. Summary of measured physical parameters of PIPUGO sponge and CS.

	PIPUGO sponge	CS
Initial component	PI, PU, GO	PI, PU, GO
Fiber diameter / nm	585 ± 264	455 ± 147
Density / mg cm^{-3}	14.8 ± 0.1	10.6 ± 0.5
[a] Deformation (50%) / %	21.41 ± 0.50	4.83 ± 0.50
[b] Stress (50%) / kPa	3.75 ± 0.30	7.29 ± 0.30
E modulus / kPa	4.26 ± 0.21	5.33 ± 0.21
Electrical condcutivity / S m^{-1}	$< 3 \times 10^{-7}$	0.85 ± 0.03

a The deformation (50%) denotes a deformation of the sample after compression test (the 101st cycle) with a strain of 50%.

b Stress (50%) describes the stress of the sample under a compressible strain of 50% (the 101st cycle).

We would like to emphasize the important role of the intermediate surface modification (step 2, **Figure 1**) of the pristine PI SFs in the preparation of porous sponges. Without intermediate modification with PU, the GO nanosheets peeled off easily (**Figure S4**). Additionally, a bottom-up fabrication strategy provides a way to construct either a membrane or a sponge from SFs with a homogeneous GO coating. Previously, large-size GO sheets were also reported for dip-coating or vacuum filtration [32-33] to modify electrospun networks, but the nonhomogeneity of the GO coating is demonstrated when contrasting the middle part with the surface of the network. This has resulted from the small pore size of electrospun networks, which hinders large sheet materials from penetrating the center of the network. Also, using an infiltration method, large-size 2D GO

12

sheets simply formed a film on the PI networked fibers, blocking the pores and thereby hindering a homogenous coating on fibers. Breaking down large sheets into smaller pieces might solve the problem but could significantly reduce the electrical conductivity of the sample. A previous study demonstrated that the electrical resistance of the films composed of small-sized GO sheets was significantly higher compared to those prepared with large-sized sheets[36]. In our work, the PI SFs' modification with the cationic PU granted access to a homogenous coating of 2D large sheets on the fiber surfaces. GOs were found homogeneously coated on the fibers even in the center of the network (**Figure S7**). The content of GO on the fiber is also tunable (**Figure S8**). The method can also be extended to the coating of other 2D sheets, such as single-layered silicates, opening a window to modify nanofibrous networks with 2D materials.

Structural characterization of the PI SF, PIPUGO sponge, and CS and for comparison of GO powder and a dried PU polymer was carried out by Fourier Transform Infrared Spectroscopy (FTIR) (**Figure S9**). X-ray diffraction (XRD) (**Figure 2a**) on PI SF revealed an amorphous halo with an asymmetric shape as a prominent feature. The local maxima of the halo around $2\theta = 7.0°$, $18.2°$, and $25.4°$ hint to small short-ranged ordered phases with characteristic correlation lengths inside the PI fiber of ≈ 13.0 Å, ≈ 5.0 Å, and ≈ 3.5 Å, respectively. These values can be explained by the monomeric repeating unit of PI and the mean in-plane and out-plane distance between non-ideal ordered polymeric chains, indicating that single-layer GO-coated fibers were still amorphous. The XRD spectra of PIPU SF and PIPUGO sponge displayed a similar trend as that of PI SF. Whereas the CS displayed broad reflexes around $2\theta = 25.5°$ and $44°$, denoting the rise in graphitic carbon. From the X-ray photoelectron spectroscopy (XPS) (**Figure 2b**), it can be observed that the contents of O and N elements decreased from 25.8 % and 3.9 % to 2.1 % and 2.7 %, respectively. Simultaneously, graphitic carbon content increased from 70.3 % to 94.2 % after heat treatment.

13

During the thermal treatment of the PIPUGO sponge (step 5), volatile species escaped resulting in a shrinkage of the CS volume. Raman spectroscopy is used to characterize the crystalline structure of graphite. The CS displayed typical D band (1350 cm^{-1}, ascribing to the disorder-induced phonon mode leading to the infinite size of crystals and defects) and G band (1590 cm^{-1}, involving out-of-phase intra-layer displacements) (**Figure 2c**), reflecting the formation of carbon structures in both turbostratic form and graphitization[37], which was mainly induced by the evolution of volatiles. In addition, the intensity ratio I_D/I_G value (~1.90) suggests that those fibers were still amorphous carbon, which agrees with the result of XRD. Importantly, after carbonization, the CS displayed a desirable conductivity of 0.85 ± 0.03 S m^{-1}, which is essential for the application as a piezoresistive sensor.

Physically robust and mechanically stable sponges were subjected to a multi-compression test with different loads. The relevant changes in mechanical properties are illustrated in **Table S1**. The stress-strain curve (20% maximal compression strain) displayed a decrease of the elastic modulus (EM) from 35.5 kPa to 5.7 kPa between the first and the third cycle (**Figure S10**). On continuing the test till the 100th cycle, the CS exhibited excellent elasticity (EM ~ 4 kPa) and stability even up to 1000 cycles. The durability of our carbon sponge is significantly better than traditional carbonized polymer aerogel and foams[38-40], which generally present fragile nature or limited shape recovering ability, and even better than some ceramic nanofiber sponges (100 cycles)[41]. The stress-strain curve showed the typical hysteresis obtained for superelastic materials. To be more specific, the stress at full load is 86 kPa for a maximum strain of 80 % (**Figure 2d**). The outstanding shape persistence was also demonstrated in multi-compression tests using the same sponge (**Figure 2e**). This shape resistance of the CS is outstanding. Fine-tuning the deformation in the composite sponges by increasing the GO layer thickness of the fibers is possible. **Figure 2f** compared the

14

deformation after compression of CSs containing different amounts of GO (7 wt%, 13 wt%, and 18 wt%). All those GO incorporated sponges exhibited a deformation < 5%. With the increase of GO, the shape recovery ability of sponges further improved. Much smaller deformations (< 3%) were also possible in sponges having very high amounts of GO (18 wt. %). However, this sponge (18 wt. %) was not the best candidate for usage, as there is merely an improvement of less than 2% in deformation by using nearly tripling the GO content, but a dramatic increase of the fabrication cost. As a comparison, the PI-1000 sponge (carbonized PI sponge: carbonization temperature 1000 °C) derived from a cross-linked PI sponge[18] displayed > 60% deformation after compression of 80% (**Figure S11**), attributed to the inherently fragile nature of carbonized PI. By modifying PI with mechanically robust and flexible GO nanosheets, the CS in this work demonstrated a superelastic character[31]. When the CS was compressed, the fiber skeletons were bent by force instead of breaking. When removing the force, the elastic fiber skeletons recovered to the original shape, resulting in the shape recovery of the CS. The high porosity is another crucial contribution to its superelasticity.

15
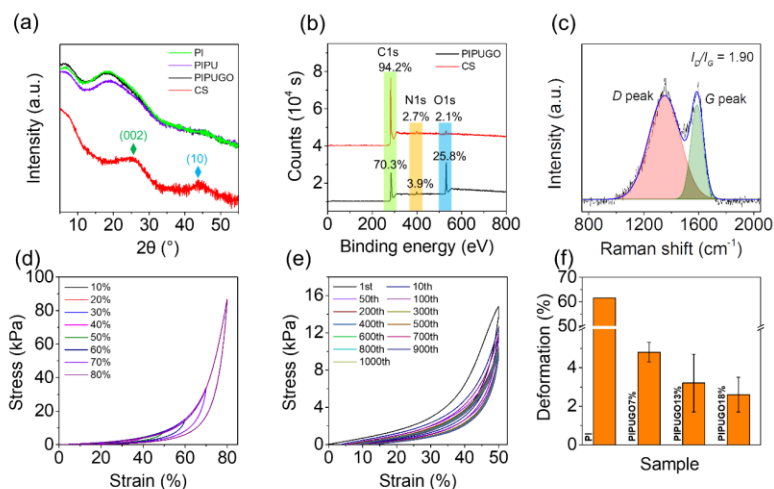
Figure 2. Investigations of the physical, chemical, and mechanical properties of CS. (a) XRD of PI (SF), PIPU (SF), PIPUGO sponge, and CS. Indexing as expected for graphitic carbon.[37] (b) XPS spectrum of CS in comparison with the one of PIPUGO sponge. (c) Raman spectrum of CS. The value of I_D/I_G was calculated by the ratio of the integrated area of the D and G peak. (d) Stress-strain curve of CS with different maximal compression strains. The curves are taken in compression cycle 10. (e) Multiple stress-strain curves of CS (maximal compression strain of 50%). (f) Deformation of CS containing various amounts of GO. The deformation took place after the first compression with maximal strain of 80%, 50 mm min^{-1} compression speed). The percentage number denotes the mass percentage of GO in the PIPUGO sponge, as determined before heating to 1000°C. For comparison, data of a PI sponge-derived sample are given.

An excellent mechanoresponsive electrical conductivity, also called piezoresistivity, is crucial for a high-performance piezoresistive sensor, which transfers pressure into an electric signal. We

16

directly displayed the piezoresistive performance of CS by employing a blue light-emitting diode (LED) and applying a voltage of 2.5 V as shown in **Figure 3a**. When the CS was in the original, uncompressed state, the LED emitted very weak, blue light. On gradually increasing the compression up to 80%, the illuminance of the LED increased from weak to brilliant blue. The compression of the CS led to the decrease in the size of the voids and consequently to a deformation of the CS network, resulting in forming more temporally electronic pathways (**Figure 3b and** SEM images in **Figure S12**) and hence an increased electric conductivity. SEM images (**Figure 3c**) showed that the size of the voids (marked by dashed lines) decreased, and thus, the contact areas of the solid material increased with increasing strain. This is also demonstrated by the 3D profiles (**Figure S13**) of the CS. The CS displayed typical piezoresistive behavior within the range of compressing strain up to 80%. The correlation between compression and resulting resistance ($\Delta R/R_0$) is linear (**Figure 3d**, the linear correlation coefficient of least square regression is $R^2=0.997$). The evaluation leads to a gauge factor of GF = 0.24, which is low compared to commonly used metal gauge strains (GF mostly in the range of 2-4). But in contrast to metals, CS provided long-time reversibility of mechanical deformation as an additional feature. The corresponding change in electrical resistance is proportional to the applied pressure (**Figure 3e**) and in the millisecond range (**Figure 3f**), but is nearly independent of the compression cycle (**Figure S14**). Moreover, we demonstrated that the stress-strain curves on CS are almost independent of the compression speed (**Figure S14**), benefitting the use as pressure sensors.

The CS can be integrated into a simple wearable pressure sensor (**Figure S15**) to monitor joint movements. The CS sensor was used to monitor multiple bending movements of the index finger, elbow, wrist, and knees, respectively. It detected bending (peak) and straight (valley) states of joint movements in real-time, demonstrating that CS is an excellent material for wearable sensors

17

(**Figure 3g, Figure S16**), which have potential application for example in wellness monitoring activities during exercises.
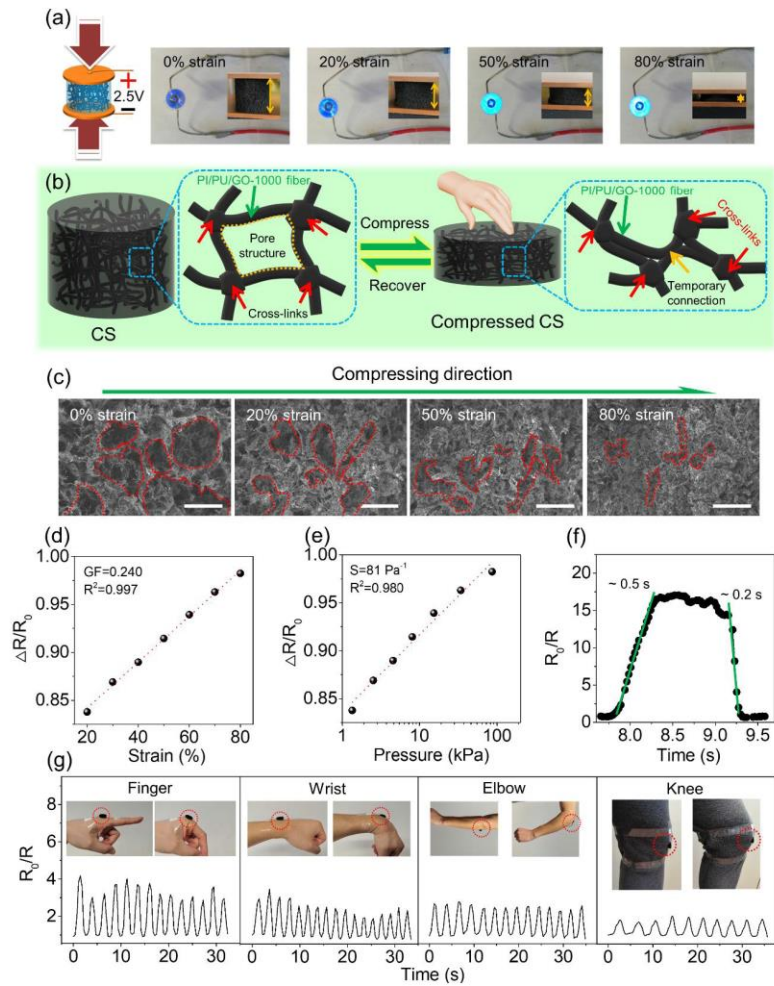
18

Figure 3. Piezoresistive properties of CS sponge. (a) Proof of concept for the application of CS as a piezoresistive sensor. The illuminance of the blue LED changed with strain. (b) Schematic illustration of elastic deformation of CS. (c) SEM images of CS under different strains. Red dashed lines (guideline for eyes only) depict voids. Scale bar 500 μm (d-e) The resistance change of the CS sensor as a function of compression strain and pressure p (GF gauge factor, R^2 coefficient of linear least square regression, sensitivity S = $(\Delta R/R_0)/p$). The data show an excellent detection range up to ~80% strain and ~90 kPa. (f) The response time of the CS sensor. The green lines mark the response time after gain and release of a maximal strain of ~50%. (g) The sensing performance of the CS sensor for real-time detection of finger, elbow, wrist, and knee movements.

19
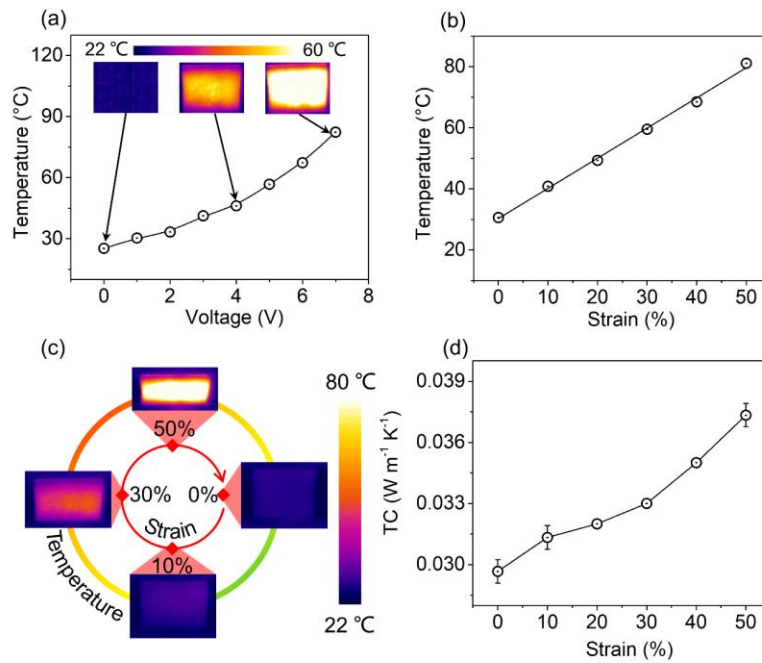
Figure 4. The mechanoresponsive heating properties of CS. (a) The Joule heating behavior of uncompressed CS under different working voltages. (b) The mechanoresponsive heating upon different compression strains with an excitation voltage of 1 V and (c) corresponding thermal images. (d) The thermal conductivity (TC) of CS upon different compression strains.

Our carbon-based material (diameter: 1.5 cm and height: 1.4 cm) possesses an extraordinary Joule-heating performance, which we investigated under ambient conditions (20 °C) by applying a low voltage of ≤7 V. The temperature was evaluated with an infrared (IR) camera (recording without using any correction by Keysight TrueIR Analysis and Reporting Tool software, **Figure 4a**). The CS demonstrated a fast heating performance up to >80 °C (equilibrium state) within 7s under ~7 V and a fast cooling feature from 80 °C to room temperature also within ~7s. Furthermore, the CS displayed an advanced mechanoresponsive Joule heating performance upon loading compression. It demonstrated a linear relationship with different loading compression strains under 1 V, and showed a widely tunable temperature range from room temperature to 81 °C by applying a compression strain from 0 to 50%, as shown in **Figure 4b**. The compressed CS possesses lower resistance compared to that without loading strain, therefore producing more Joule heat and showing a higher temperature, as depicted in **Figure 4c** according to the equation;

$$Q = U^2/R \cdot t \tag{4},$$

where U, R, and t denote voltage, electrical resistance, and time, respectively. The mechanoresponsive heating is due to the piezoresistivity of the sponge. The mechanoresponsive heating behavior of CS allows heating devices to work in a more energy-saving heating mode.

As a typical porous sponge, apart from the electrothermal feature, the CS demonstrated extraordinary thermal insulation with intriguing mechanoresponsive thermal conductivity. The CS

20

138

displays a thermal conductivity of 0.029-0.037 W m^{-1} K^{-1} depending upon the compression strains from 0 to 50% (**Figure 4d**, Hot Disk measurements). Hence, even under high compression, CS is still a prominent thermal insulating material, equal or even better than natural sheep wool (0.039 W m^{-1} K^{-1}), cotton (0.040 W m^{-1} K^{-1}), commercial fiber insulating board (0.048 W m^{-1} K^{-1}), and most other types of commercial insulation materials (0.035-0.160 W m^{-1} K^{-1}). Moreover, the CS displayed an interesting combination of not only high thermal insulation but also a desirable electrical conductivity, which is unique compared to other types of materials (**Figure 5a**).

Both thermal conductivity and electrical conductivity of CS are adjustable by densification of CS (**Table S2**). Changing the density from 6.4 mg cm^{-3} to 29.1 mg cm^{-3} changed the thermal conductivity from 0.027 W m^{-1} K^{-1} to 0.038 W m^{-1} K^{-1}, still maintaining a very low value. From the thermal image (**Figure S17**, equilibrium state), it could be seen that the bottom of CS showed the same apparent temperature (~150 °C, L2) as the hot plate (L1), a much lower apparent temperature (~53 °C, L3) in the middle part of the sponge (compared to hot plate), and an apparent temperature (~34 °C, L4) on the top part close to ambient air (~24 °C, L5), indicating its excellent thermal insulating performance. Depending on its interesting thermal properties, including mechanoresponsive electric Joule heating and outstanding thermal insulation performance, CS can be applied as wearable devices for thermal management, keeping the human body warm. The presented sponge shows an excellent combination of properties, such as decent electrical conductivity, high thermal resistivity, specific electrical conductivity, specific thermal resistivity, high porosity, and ultra flexibility with a compressible strain of up to 80% (**Figure 5b**) compared to previous aerogels/sponges[30, 42-44], which are hard to present all these properties high. For example, inorganic nanofiber aerogels[43] generally display flexibility (MaxCS), high porosity (P) and high thermal insulation properties (TR and lg TR/D). However, their poor electrical properties

21

139

(lg EC, and lg EC/D) are ill-suitable for electrofunctionality usage. Additionally, the composite aerogels[42] (e.g. eggplant-derived SiC aerogel) displayed high values of MaxCS, lg EC, and lg EC/D, but low values of TR, lg TR/D, and P, generally meaning poor thermal insulation performance. On the contrary, our sponge provides a unique combination property to serve as an ultralight electrical conductor and a high-performance thermal insulator, which could be very promising for wearable electronics. Furthermore, the intriguing electric heating feature can be used for heat compensation and heat therapy to wearers.
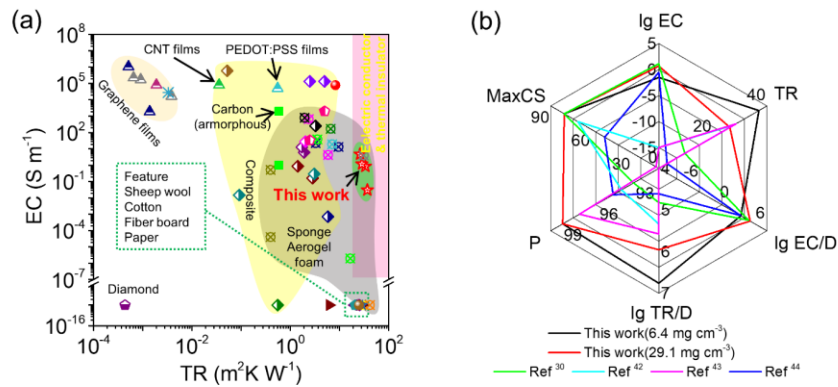
Figure 5. (a) Comparison of the electrical conductivity and thermal resistivity versus other materials. Details see supporting information **Table S3.** (b) Comparison of the combined properties versus previous 3D porous materials. Ref.[30]: SiC-coated carbonized loofah sponge, Ref.[42]: Eggplant-derived SiC aerogel, Ref.[43]: Silica nanofibrous aerogels, Ref.[44]: Graphene-crosslinked carbon nanotube sponge/polyimide nanocomposite. (Abbreviation: lg: the logarithm base 10; EC: electrical conductivity; TR: thermal resistivity; D: density; P: porosity; MaxCS: max compression strain)

22

140

4. CONCLUSION

In summary, we explore ultralight carbon sponges by carbonizing GO-coated PI composite sponges. Intermediate modification with a polycationic PU proved necessary for getting a stable and uniform GO coating on polymer precursor fibers. The resultant sponges demonstrated ultralow density of 6 - 30 mg cm^{-3}. The excellent mechanical flexibility of our carbon sponge allowed a deformation as high as 80% and high durability of multiple compression under 50% deformation. Moreover, our carbon sponges presented the unique combination property of both high electrical conductivity (0.03 - 4.72 S m^{-1}) and thermal insulation (0.027 - 0.038 W m^{-1} K^{-1}), which rarely exists in current materials. In addition, our carbon sponges displayed attractive mechanoresponsive electrical and thermal properties, attributed to the high porosity and compression ability. The mechanoresponsive electrical conductivity endows the carbon sponges with mechanical sensing possibility. Meanwhile, the mechanoresponsive thermal property provides the carbon sponge Joule heating function, operated by either tuning voltage or deformation. Based on these advantageous characteristics, our sponge demonstrated a novel application for multifunctional wearable sensing systems with an advanced modality of thermal management.

ASSOCIATED CONTENT

Supporting Information

The Supporting Information is available free of charge at:

Optical and SEM images of PI short fibers; SEM image of PIPU fibers; The characterization of small-angle X-ray scattering; GO coating stability of PIPUGO SF and PIGO SF; Characterization of exfoliated GO; SEM images of the hierarchical pore structure of CS at different magnifications; SEM images of different GO-coated PI membranes; Schematic diagram of fibers with different

23

thicknesses of GO coating and corresponding SEM images; FTIR spectrums; Compression stress-strain curve; Digital images of PI-1000 sponge during and after the compression test; Mechanical and piezoresistive behavior of CS; CS application for a simple body movement sensor; Digital images and corresponding real-time electric signal of the CS sensor for the detection of joint movement; The apparent temperature of CS in different planes; Physical parameter, multi-compression test, electrical and thermal conductivity of CS. (PDF)

AUTHOR INFORMATION

Corresponding Authors

Seema Agarwal - Macromolecular Chemistry II and Bavarian Polymer Institute, Department of Chemistry, University of Bayreuth, Universitätsstrasse 30, 95440 Bayreuth, Germany; E-mail: agarwal@uni-bayreuth.de

Andreas Greiner - Macromolecular Chemistry II and Bavarian Polymer Institute, Department of Chemistry, University of Bayreuth, Universitätsstrasse 30, 95440 Bayreuth, Germany; E-mail: greiner@uni-bayreuth.de

Authors

Qiang Gao - Macromolecular Chemistry II and Bavarian Polymer Institute, Department of Chemistry, University of Bayreuth, Universitätsstrasse 30, 95440 Bayreuth, Germany

Thomas Tran - Bavarian Center for Battery Technology (BayBatt), Bavarian Polymer Institute, and Bayreuth Center for Colloids and Interfaces, Department of Chemistry, Physical Chemistry I, University of Bayreuth, Universitätsstrasse 30, 95440 Bayreuth, Germany

Xiaojian Liao - Macromolecular Chemistry II and Bavarian Polymer Institute, Department of Chemistry, University of Bayreuth, Universitätsstrasse 30, 95440 Bayreuth, Germany

24

Sabine Rosenfeldt - Bavarian Center for Battery Technology (BayBatt), Bavarian Polymer Institute, and Bayreuth Center for Colloids and Interfaces, Department of Chemistry, Physical Chemistry I, University of Bayreuth, Universitätsstrasse 30, 95440 Bayreuth, Germany

Chao Gao - MOE Key Laboratory of Macromolecular Synthesis and Functionalization, Department of Polymer Science and Engineering, Institute of Applied Mechanics, State Key Laboratory of Fluid Power and Mechatronic Systems, Zhejiang University, Hangzhou 310027, China; Hangzhou Gaoxi Technology Co., Ltd., Hangzhou 310027, P. R. China

Haoqing Hou - College of Chemistry and Chemical Engineering, Jiangxi Normal University, Nanchang 330022, PR China

Markus Retsch - Bavarian Center for Battery Technology (BayBatt), Bavarian Polymer Institute, and Bayreuth Center for Colloids and Interfaces, Department of Chemistry, Physical Chemistry I, University of Bayreuth, Universitätsstrasse 30, 95440 Bayreuth, Germany

Notes

There are no conflicts to declare.

25

REFERENCES

1. Gao, W.; Emaminejad, S.; Nyein, H. Y. Y.; Challa, S.; Chen, K.; Peck, A.; Fahad, H. M.; Ota, H.; Shiraki, H.; Kiriya, D., Fully integrated wearable sensor arrays for multiplexed in situ perspiration analysis. Nature **2016**, 529 (7587), 509-514.

2. Pang, C.; Lee, G.-Y.; Kim, T.-i.; Kim, S. M.; Kim, H. N.; Ahn, S.-H.; Suh, K.-Y., A flexible and highly sensitive strain-gauge sensor using reversible interlocking of nanofibres. Nat. Mater. **2012**, 11 (9), 795-801.

3. Raspopovic, S.; Valle, G.; Petrini, F. M., Sensory feedback for limb prostheses in amputees. Nat. Mater. **2021**, 1-15.

4. Baumgartner, M.; Hartmann, F.; Drack, M.; Preninger, D.; Wirthl, D.; Gerstmayr, R.; Lehner, L.; Mao, G.; Pruckner, R.; Demchyshyn, S., Resilient yet entirely degradable gelatin-based biogels for soft robots and electronics. Nat. Mater. **2020**, 19 (10), 1102-1109.

5. Wu, Y.; Liu, Y.; Zhou, Y.; Man, Q.; Hu, C.; Asghar, W.; Li, F.; Yu, Z.; Shang, J.; Liu, G.; Liao, M.; Li, R.-W., A skin-inspired tactile sensor for smart prosthetics. Sci. Robot. **2018**, 3 (22), eaat0429.

6. Gao, W.; Ota, H.; Kiriya, D.; Takei, K.; Javey, A., Flexible electronics toward wearable sensing. Acc. Chem. Res. **2019**, 52 (3), 523-533.

7. Kang, D.; Pikhitsa, P. V.; Choi, Y. W.; Lee, C.; Shin, S. S.; Piao, L.; Park, B.; Suh, K.-Y.; Kim, T.-i.; Choi, M., Ultrasensitive mechanical crack-based sensor inspired by the spider sensory system. Nature **2014**, 516 (7530), 222-226.

26

8. Lim, H. R.; Kim, H. S.; Qazi, R.; Kwon, Y. T.; Jeong, J. W.; Yeo, W. H., Advanced soft materials, sensor integrations, and applications of wearable flexible hybrid electronics in healthcare, energy, and environment. Adv. Mater. **2020**, 32 (15), 1901924.

9. Huynh, T. P.; Haick, H., Autonomous flexible sensors for health monitoring. Adv. Mater. **2018**, 30 (50), 1802337.

10. He, W.; Sohn, M.; Ma, R.; Kang, D. J., Flexible single-electrode triboelectric nanogenerators with MXene/PDMS composite film for biomechanical motion sensors. Nano Energy **2020**, 78, 105383.

11. Qi, D.; Zhang, K.; Tian, G.; Jiang, B.; Huang, Y., Stretchable electronics based on PDMS substrates. Adv. Mater. **2021**, 33 (6), 2003155.

12. Jayathilaka, W. A. D. M.; Qi, K.; Qin, Y.; Chinnappan, A.; Serrano‐García, W.; Baskar, C.; Wang, H.; He, J.; Cui, S.; Thomas, S. W., Significance of nanomaterials in wearables: a review on wearable actuators and sensors. Adv. Mater. **2019**, 31 (7), 1805921.

13. Lee, Y.; Park, J.; Choe, A.; Cho, S.; Kim, J.; Ko, H., Mimicking human and biological skins for multifunctional skin electronics. Adv. Funct. Mater. **2020**, 30 (20), 1904523.

14. Sim, K.; Rao, Z.; Zou, Z.; Ershad, F.; Lei, J.; Thukral, A.; Chen, J.; Huang, Q.-A.; Xiao, J.; Yu, C., Metal oxide semiconductor nanomembrane–based soft unnoticeable multifunctional electronics for wearable human-machine interfaces. Sci. Adv. **2019**, 5 (8), eaav9653.

15. Ding, T.; Chan, K. H.; Zhou, Y.; Wang, X.-Q.; Cheng, Y.; Li, T.; Ho, G. W., Scalable thermoelectric fibers for multifunctional textile-electronics. Nat. Commun. **2020**, 11 (1), 1-8.

16. Lee, G.; Bae, G. Y.; Son, J. H.; Lee, S.; Kim, S. W.; Kim, D.; Lee, S. G.; Cho, K., User‐interactive thermotherapeutic electronic skin based on stretchable thermochromic strain sensor. Adv. Sci. **2020**, 7 (17), 2001184.

27

17. Jiang, S. H.; Agarwal, S.; Greiner, A., Low-density open cellular sponges as functional materials. Angew. Chem. Int. Ed. **2017**, 56 (49), 15520-15538.

18. Jiang, S.; Uch, B.; Agarwal, S.; Greiner, A., Ultralight, thermally insulating, compressible polyimide fiber assembled sponges. ACS Appl. Mater. Interfaces **2017**, 9 (37), 32308-32315.

19. Duan, G.; Jiang, S.; Jérôme, V.; Wendorff, J. H.; Fathi, A.; Uhm, J.; Altstädt, V.; Herling, M.; Breu, J.; Freitag, R.; Agarwal, S.; Greiner, A., Ultralight, soft polymer sponges by self‑assembly of short electrospun fibers in colloidal dispersions. Adv. Funct. Mater. **2015**, 25 (19), 2850-2856.

20. Ding, Y.; Xu, T.; Onyilagha, O.; Fong, H.; Zhu, Z., Recent advances in flexible and wearable pressure sensors based on piezoresistive 3D monolithic conductive sponges. ACS Appl. Mater. Interfaces **2019**, 11 (7), 6685-6704.

21. Wang, Y.; Wang, Z.; Chen, Y.; Zhang, H.; Yousaf, M.; Wu, H.; Zou, M.; Cao, A.; Han, R. P., Hyperporous sponge interconnected by hierarchical carbon nanotubes as a high‑performance potassium‑ion battery anode. Adv. Mater. **2018**, 30 (32), 1802074.

22. Qin, M.; Xu, Y.; Cao, R.; Feng, W.; Chen, L., Efficiently controlling the 3D thermal conductivity of a polymer nanocomposite via a hyperelastic double-continuous network of graphene and sponge. Adv. Funct. Mater. **2018**, 28 (45), 1805053.

23. Gui, X.; Wei, J.; Wang, K.; Cao, A.; Zhu, H.; Jia, Y.; Shu, Q.; Wu, D., Carbon nanotube sponges. Adv. Mater. **2010**, 22 (5), 617-21.

24. Lee, M. H.; Kang, Y. H.; Kim, J.; Lee, Y. K.; Cho, S. Y., Freely shapable and 3D porous carbon nanotube foam using rapid solvent evaporation method for flexible thermoelectric power generators. Adv. Energy Mater. **2019**, 9 (29), 1900914.

28

25. Zhu, C.; Han, T. Y.; Duoss, E. B.; Golobic, A. M.; Kuntz, J. D.; Spadaccini, C. M.; Worsley, M. A., Highly compressible 3D periodic graphene aerogel microlattices. Nat. Commun. **2015**, 6, 6962.

26. Wang, C.; Xia, K.; Wang, H.; Liang, X.; Yin, Z.; Zhang, Y., Advanced Carbon for Flexible and Wearable Electronics. Adv. Mater. **2019**, 31 (9), e1801072.

27. Li, J.; Ding, Y.; Yu, N.; Gao, Q.; Fan, X.; Wei, X.; Zhang, G.; Ma, Z.; He, X., Lightweight and stiff carbon foams derived from rigid thermosetting polyimide foam with superior electromagnetic interference shielding performance. Carbon **2020**, 158, 45-54.

28. Yuan, Y.; Liu, L.; Yang, M.; Zhang, T.; Xu, F.; Lin, Z.; Ding, Y.; Wang, C.; Li, J.; Yin, W., Lightweight, thermally insulating and stiff carbon honeycomb-induced graphene composite foams with a horizontal laminated structure for electromagnetic interference shielding. Carbon **2017**, 123, 223-232.

29. Yuan, Y.; Ding, Y.; Wang, C.; Xu, F.; Lin, Z.; Qin, Y.; Li, Y.; Yang, M.; He, X.; Peng, Q.; Li, Y., Multifunctional stiff carbon foam derived from bread. ACS Appl. Mater. Interfaces **2016**, 8 (26), 16852-61.

30. Li, S.; Liu, D.; Li, W.; Sui, G., Strong and heat-resistant SiC-coated carbonized natural loofah sponge for electromagnetic interference shielding. ACS Sustain. Chem. Eng. **2019**, 8 (1), 435-444.

31. Kim, K. H.; Oh, Y.; Islam, M. F., Graphene coating makes carbon nanotube aerogels superelastic and resistant to fatigue. Nat. Nanotechnol. **2012**, 7 (9), 562-566.

32. Zhan, Y. Q.; Wan, X. Y.; He, S. J.; Yang, Q. B.; He, Y., Design of durable and efficient poly(arylene ether nitrile)/bioinspired polydopamine coated graphene oxide nanofibrous composite membrane for anionic dyes separation. Chem. Eng. J. **2018**, 333, 132-145.

29

33. Zhang, M.; Cui, J.; Lu, T.; Tang, G.; Wu, S.; Ma, W.; Huang, C., Robust, functionalized reduced graphene-based nanofibrous membrane for contaminated water purification. Chem. Eng. J. **2021**, 404, 126347.

34. Hu, P.; Greiner, A.; Agarwal, S., Synthesis and properties evaluation of quaternized polyurethanes as antibacterial adhesives. J. Polym. Sci. A: Polym. Chem. **2019**, 57 (6), 752-757.

35. Inagaki, M.; Ohta, N.; Hishiyama, Y., Aromatic polyimides as carbon precursors. Carbon **2013**, 61, 1-21.

36. Zheng, Q.; Ip, W. H.; Lin, X.; Yousefi, N.; Yeung, K. K.; Li, Z.; Kim, J.-K., Transparent conductive films consisting of ultralarge graphene sheets produced by Langmuir–Blodgett assembly. ACS Nano **2011**, 5 (7), 6039-6051.

37. Zhang, M.; Niu, H.; Qi, S.; Tian, G.; Wang, X.; Wu, D., Structure evolutions involved in the carbonization of polyimide fibers with different chemical constitution. Mater. Today Commun. **2014**, 1 (1-2), 1-8.

38. Chen, H.-B.; Wang, Y.-Z.; Schiraldi, D. A., Preparation and flammability of poly (vinyl alcohol) composite aerogels. ACS Appl. Mater. Interfaces **2014**, 6 (9), 6790-6796.

39. Wei, G.; Miao, Y.-E.; Zhang, C.; Yang, Z.; Liu, Z.; Tjiu, W. W.; Liu, T., Ni-doped graphene/carbon cryogels and their applications as versatile sorbents for water purification. ACS Appl. Mater. Interfaces **2013**, 5 (15), 7584-7591.

40. Huang, Y.; Lai, F.; Zhang, L.; Lu, H.; Miao, Y.-E.; Liu, T., Elastic carbon aerogels reconstructed from electrospun nanofibers and graphene as three-dimensional networked matrix for efficient energy storage/conversion. Sci. Rep. **2016**, 6 (1), 1-11.

30

41. Wang, H.; Zhang, X.; Wang, N.; Li, Y.; Feng, X.; Huang, Y.; Zhao, C.; Liu, Z.; Fang, M.; Ou, G., Ultralight, scalable, and high-temperature–resilient ceramic nanofiber sponges. Sci. Adv. **2017**, 3 (6), e1603170.

42. Liang, C.; Wang, Z., Eggplant-derived SiC aerogels with high-performance electromagnetic wave absorption and thermal insulation properties. Chem. Eng. J. **2019**, 373, 598-605.

43. Wang, F.; Dou, L.; Dai, J.; Li, Y.; Huang, L.; Si, Y.; Yu, J.; Ding, B., In situ synthesis of biomimetic silica nanofibrous aerogels with temperature‐invariant superelasticity over one million compressions. Angew. Chem. Int. Ed. **2020**, 59 (21), 8285-8292.

44. Zhang, F.; Feng, Y.; Qin, M.; Gao, L.; Li, Z.; Zhao, F.; Zhang, Z.; Lv, F.; Feng, W., Stress controllability in thermal and electrical conductivity of 3D elastic graphene‐crosslinked carbon nanotube sponge/polyimide nanocomposite. Adv. Funct. Mater. **2019**, 29 (25), 1901383.

31

Supporting Information

Ultralight heat-insulating, electrically conductive carbon fibrous sponges for wearable mechanosensing devices with advanced warming function

Qiang Gao[a], Thomas Tran[b], Xiaojian Liao[a], Sabine Rosenfeldt[b], Chao Gao[c], Haoqing Hou[d], Markus Retsch[b], Seema Agarwal[a], Andreas Greiner[a*]*

[a] Macromolecular Chemistry II and Bavarian Polymer Institute, Department of Chemistry, University of Bayreuth, Universitätsstrasse 30, 95440 Bayreuth, Germany

[b] Bavarian Center for Battery Technology (BayBatt), Bavarian Polymer Institute, and Bayreuth Center for Colloids and Interfaces, Department of Chemistry, Physical Chemistry I, University of Bayreuth, Universitätsstrasse 30, 95440 Bayreuth, Germany

[c] MOE Key Laboratory of Macromolecular Synthesis and Functionalization, Department of Polymer Science and Engineering, Institute of Applied Mechanics, State Key Laboratory of Fluid Power and Mechatronic Systems, Zhejiang University, Hangzhou 310027, China. Hangzhou Gaoxi Technology Co., Ltd., Hangzhou 310027, P. R. China

[d] College of Chemistry and Chemical Engineering, Jiangxi Normal University, Nanchang 330022, PR China

* Corresponding author, E-mail: agarwal@uni-bayreuth.de (Seema Agarwal); greiner@uni-bayreuth.de (Andreas Greiner)

1

Characterizations:

The optical image (Figure S1) was performed on a Digitales Mikroskop (VHX-100, KEYENCE) coupled with a VH-Z450. A 500x magnification lens was used for the observation.

Optical Microscopy images and corresponding 3D profiles (Figure S12) were taken with the Technical Documentation Microscopy (Smartzoom 5, ZEISS) equipped with a ZEISS Lens (PlanApo D 5x/0.3 FWD 30mm).

For SAXS analysis the samples were measured as obtained at ambient conditions using a Double Ganesha Air system (SAXSLAB, Denmark), equipped with a rotation copper anode 8mICROmAX ==/hf; Rigaku Corporation, Japan) and a position sensitive detector (PILATUS 300K, Dectris). 1D data were obtained by radial averaging, the data are normalized to incident beam, transmission, accumulation time and an assumed sample thickness of 1 mm. Background subtraction was done using the scattering of air or the corresponding solvent. Further data analysis was done using the software Scatter [1] or Sasview.

FTIR was performed on Spectrum 100 FTIR (Perkin Elmer). All samples were measured in the wavenumber region between 400 - 4000 cm^{-1} with data points in the interval of 1 cm^{-1} four times

Reference

[1] Förster, S.; Fischer, S.; Zielske, K.; Schellbach, C.; Sztucki, M.; Lindner, P.; Perlich, J., Calculation of scattering-patterns of ordered nano-and mesoscale materials. Adv. Colloid Interface Sci. **2011,** 163 (1), 53-83.

2

Supporting Figures
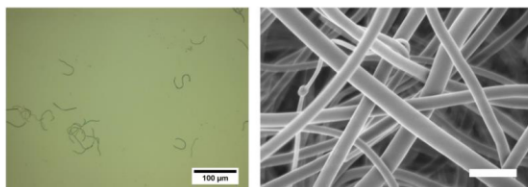
Figure S1. Optical (left) and SEM (right, scale bar 2 μm) images of PI short fibers. Fiber length:

89 ± 52 μm and fiber diameter: 445 ± 114 nm
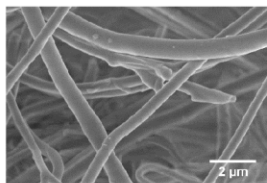
Figure S2. SEM image of PIPU fibers.

3
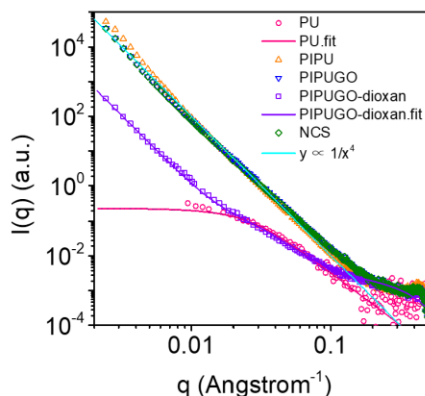
Figure S3. Investigation of the CS formation using small-angle X-ray scattering (SAXS). The radial averaged data are corrected for the solvent or the air scattering and normalized to the same absolute scale at high q for better visibility. Experimental data were given by symbols, theoretical descriptions by lines.

The single steps of the CS fabrication were addressed in the main text (**Figure 1a**). The PU solution (1 wt% in THF, used in step 2, pink color) could be described with a polymer excluded volume model. The idea of this model is that parts of long-chain molecules cannot occupy space which is already occupied by other parts of it. This excluded volume is modeled by a clustered network of spheres, which is characterized by a Porod exponent of 3 (mass fractal) and a radius of gyration of $R_g = 7$ nm.

The scattering of the sponges (PIPU orange, PIPUGO blue and CS green) are characterized mainly by the sharp interfaces inside the dried sponges, which exhibit a q^{-4} power law (typical for the surface to volume ratio of dense systems, Porod law). The PIPUGO sponge was put into dioxane to allow swelling of PU. The corresponding 1D-SAXS is plotted in violet. In the intermediate range (0.01 Å^{-1} < q < 0.15 Å^{-1}), (compared to sponges) it showed a significantly different behavior, which strongly resembles dissolved PU-chains. In a first approach we were

4

able to describe the PIPUGO intensity by addition of three partial intensities, namely (1) a Porod regime (contribution of sponge network, mainly at low q), (2) an intensity expected from the PU polymers (polymer excluded volume model, $R_g = 7$ nm hinting to a PU layer thickness in that size range, main contribution at intermediate q) and (3) an intensity of circular discs (contribution of GO sheets, mainly at high q, modeled by nanodiscs with 1 nm thickness and 20 µm lateral dimension). Since the thickness of the individual fibers of dried PIPUGO should be equal or smaller, we estimated the maximal PU layer thickness to 14 nm ($=2\ R_g$). Note, that the PU layer was a prerequisite for the GO coating of CS sponges. Since the surfaces of GO and PI are both negatively charged, just dipping the PI sponge into an (aqueous) solution of GO (0.05 wt%) was no option.
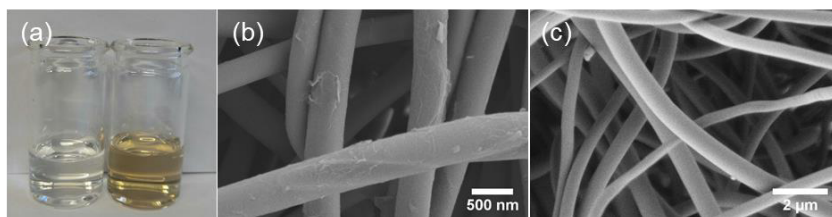
Figure S4. GO coating stability of PIPUGO SF and PIGO SF. (a) Photos of PIPUGO SF (left) and PIGO SF (right) dispersions (2 mg fiber in 2 mL water) after shaking the dispersions by hand. The first solution is transparent and thus, hints at a complete and stable immobilization of GO onto PIPU fibers. The brown color of the dispersion (more intense with increasing shaking time) is an indication that the interaction of GO and PI is very weak, resulting in peeling off of already attached GO. Corresponding SEM images of (b) PIPUGO SF and (c) PIGO SF filtered out from the dispersion. A PET mesh (pore size 50 µm) was used to separate fibers from the dispersion.

5
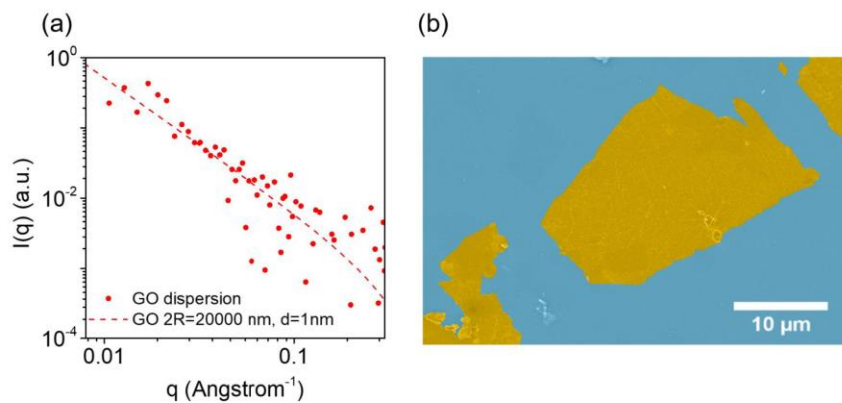
Figure S5. Characterization of exfoliated GO. (a) SAXS data of a GO dispersion (5 mg mL^{-1} in water, red dots, the solvent, water, is already subtracted) compared to the theoretical intensity (line) of discs with a radius of R = 10 μm and a thickness of 1 nm. (b) Photoshop colored SEM image of GO nanosheets (GO in yellow, background in blue)
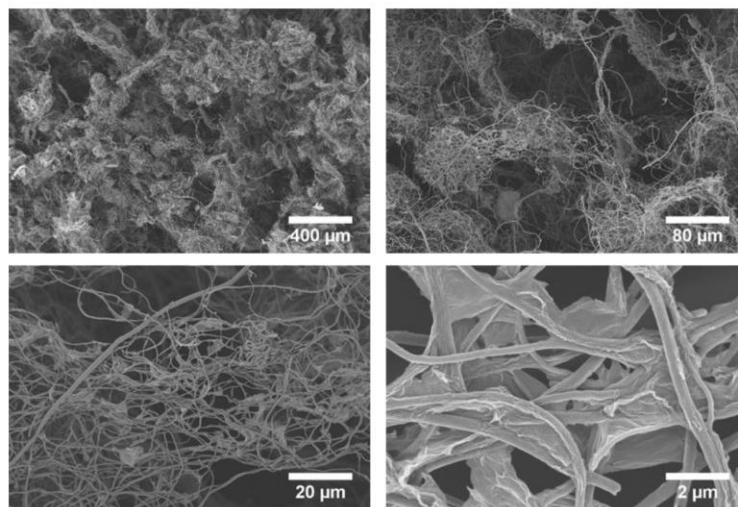
Figure S6. SEM images of the hierarchical pore structure of CS at different magnifications.

6
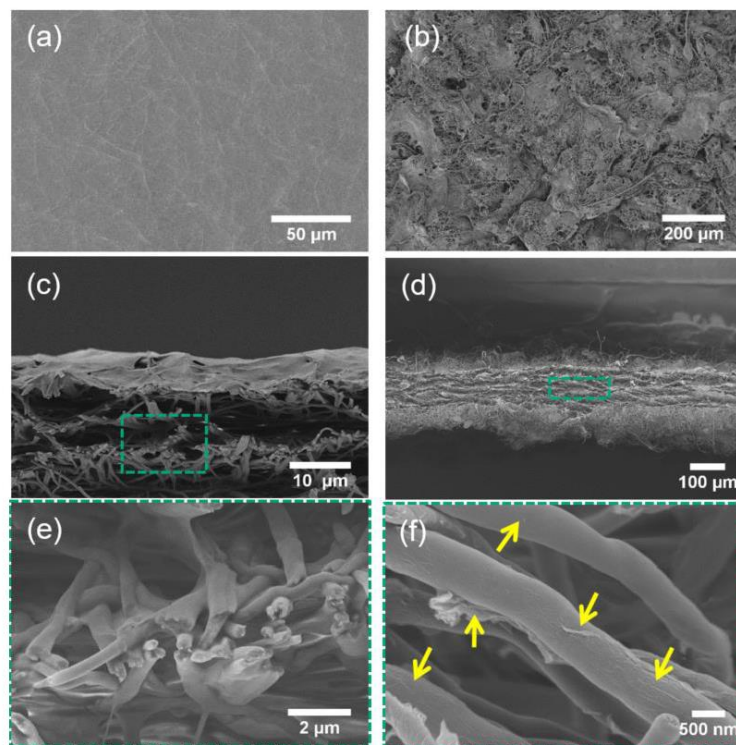
Figure S7 SEM images of different GO-coated PI membranes. (a) PI membrane (step 1, starting material) after the filtration of GO dispersion (0.05 mg mL^{-1}, 2mL). (b) PIPUGO SF (step 4, starting material, 10 mg) membrane prepared with the wet-laid method. (c-f) Corresponding cross-sections of PI membrane (c,e) and PIPUGO SF membrane (d-f) in different magnifications. GO was labeled with yellow arrows.

7
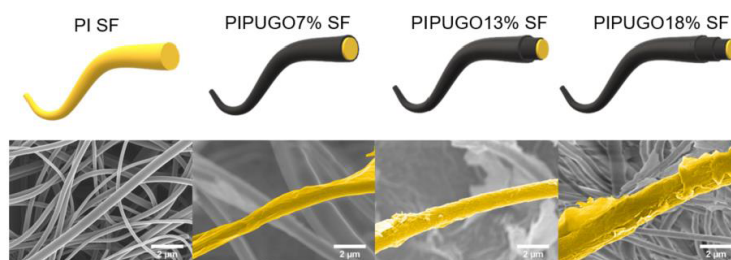
Figure S8. Schematic diagram of fibers with different thicknesses of GO coating and corresponding SEM images (GO on the fiber surface is colored in yellow). PI SF was directly obtained from step 1. PIPUGO7% SF was from step 4. PIPUGO13% SF was prepared by using PIPUGO7% SF as starting material to repeat step 2 and step 3. Similarly, PIPUGO18% SF was prepared by using PIPUGO13% SF as starting material to repeat step 2 and step 3.
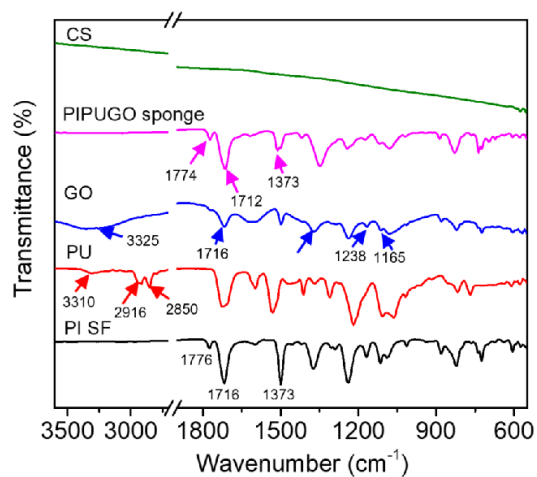
Figure S9. FTIR spectrums of PI SF, PIPUGO sponge and CS and for comparison of a GO powder and a PU polymer.

8

The FTIR spectrum of PI shows all signals expected for the pristine polymer, in detail the vibration bands of imide rings (characteristic doublet of C=O out/in-plane vibration at $1716/1776$ cm^{-1}, C-N-C axial/transverse stretching at 1373 cm^{-1} and C-N-C out of plane bending at 721 cm^{-1}), vibration bands stemming from the aromatic rings (tangential vibrations ~1000-1600 cm^{-1}, radial skeleton vibration ~565-750 cm^{-1} and out of plane bending vibrations ~600-950 cm^{-1}). Interpretation of FTIR bands of the composite sponge (PIPUGO) was difficult since it showed features of the polymeric scaffold as well as of GO. Therefore, we measured the pattern of the used PU polymer and GO powder and compared it with the one of the PIPUGO sponge. The PU shows N-H stretching vibrations (3310 cm^{-1}) and CH stretching vibrations (2850 cm^{-1} and 2916 cm^{-1}). The GO spectrum shows typical bands of hydroxyl stretching and deformation (3325 cm^{-1} and 1373 cm^{-1}), C-OH stretching (1238 cm^{-1} and 1165 cm^{-1}), C=O stretching (1716 cm^{-1}). In the FTIR data of PIPUGO the dramatic reduction of the intensity of C-N vibrations (1373 cm^{-1}) and the missing of CH peaks indicated the fully wrapped surface of PIPU SF by GOs. The shift of C=O vibrations (1351 cm^{-1} and 1718 cm^{-1}) demonstrated the existence of hydrogen bonds in the PIPUGO. Consequently, vibration bands of C=O, C-O, C-N are vanished in the spectrum of CS, indicating that the pyrolysis of PIPU leads to non-volatile heterocyclic graphitic structures and gases like H_2, CO, CO_2 and N_2.

9
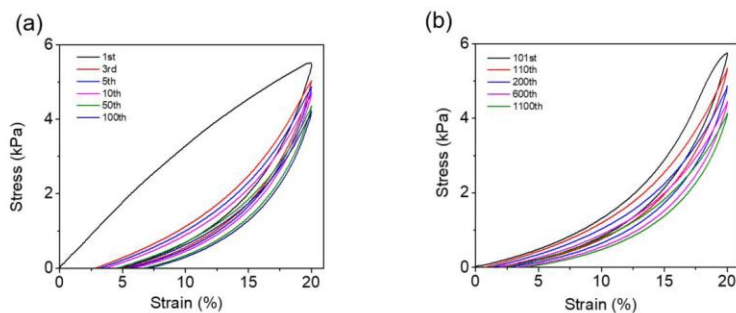
Figure S10. Compression stress-strain curve of (a) the first 100-cycle and (b) the following 1000 cycles of CS. (Compression speed 50 mm min^{-1})
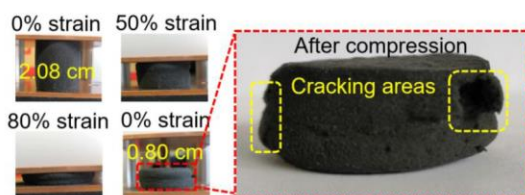
Figure S11. Digital images of PI-1000 sponge during and after the compression test. The original height (2.08 cm) and the height after compression (0.80 cm) of PI-1000 are labeled in the corresponding image. Due to the lack of mechanical resilience, the PI-1000 sponge was unable to recover its shape after compression. It displayed a large deformation and cracking areas on the surface.

10
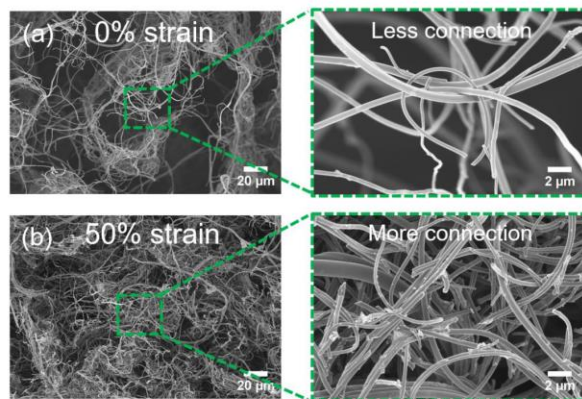
Figure S12. SEM images of CS. (a) Under 0% compression strain. In this state, CS presented less connections between fibers and high resistance. (b) Under 50% compression strain. In this state, more temporary fiber connections were formed by the compression to increase the ability of electron passes, leading to a reduction of resistance.
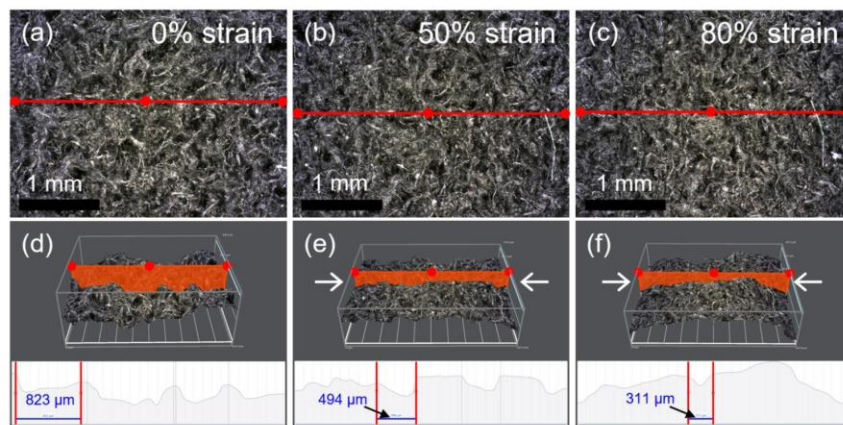
Figure S13. Optical Microscopy images (a-c) and corresponding 3D profiles (d-f, white arrow represents compression direction). The width of the major large pore reduces from ~800 μm to ~300 μm in the direction of compression.

11
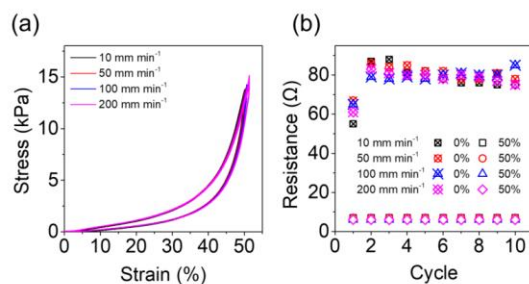
Figure S14. Mechanical and piezoresistive behavior of CS. For each compression experiment with multiple cycles, one sponge was used. (a) Stress-strain curves of PI/PU/GO 1000 using different compression speeds. The data are taken in the 10th compression cycle. (b) Resistance independence of compression cycle number and strain (0% and 50%).
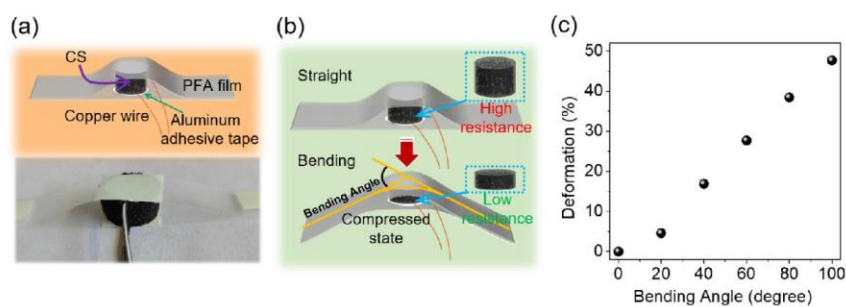
Figure S15. CS application for a simple body movement sensor. (a) A schematic diagram (top) and digital image (bottom) of the CS sensor. The CS sensor was assembled with two strips of perfluoroalkoxy alkane (PFA) films (1 cm × 10 cm, thickness of 9.8 ± 1 μm). Copper wire electrodes were fixed with aluminum adhesive tapes. (b) The working mechanism of the CS sensor. When the CS sensor is bent, the bending angle of the plastic strip causes a compression deformation of the CS and consequently leads to a change in resistance. (c) The deformation of CS upon the bending angle of the CS sensor.

12
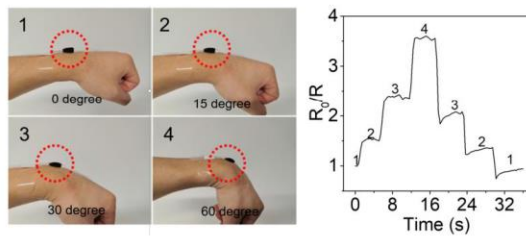
Figure S16. Digital images (left) and corresponding real-time electric signal (resistance, right) of the CS sensor for the detection of joint movement.
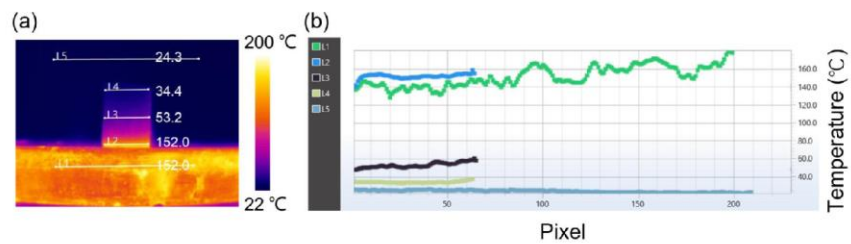
Figure S17. The apparent temperature of CS in different planes. (a) Thermal image of CS standing on a hot plate. L1, L2, L3, L4 and L5 respectively denote the hot plate, the bottom, middle and top plane of CS, and ambient air. The numbers at the right side of each line are the average temperature of the lines. (b) The temperature of the lines in the left thermal image. In each curve, the 0 of X-axis means the starting left point of the line.

13

Supporting Tables

<div align="center">

Table S1. Multi-compression test of CS

</div>

Test name	Stress / kPa	E modulus / kPa	Deformation / %
Initial (20 %)	5.5	35.4	0
100 cycles (20 %)	4.2	6.3	2.6
1000 cycles (20 %)	4.1	6.1	5.3
100 cycles (50 %)	12.0	3.7	16.7

The 20% and 50% respectively describe the maximum strain of tests. The compression speed was set to 50 mm min^{-1}. The elastic modulus was calculated at the point of 5% strain (EM = Stress (at 5%) / 5%).

14

Table S2. Summary of electrically conductivity (EC) and thermal conductivity (TC) of CS with different densities.

Density / mg cm^{-3}	EC / S m^{-1}	TC / W m^{-1}K^{-1}
6.42 ± 0.07	0.03 ± 0.00	0.027± 0.000
10.63 ± 0.45	0.85 ± 0.03	0.029 ± 0.001
18.87 ± 0.03	1.17 ± 0.00	0.034 ± 0.002
29.12 ± 5.25	4.72 ± 0.31	0.038 ± 0.000

15

Table S3. Comparison of the electrical conductivity and thermal resistivity for different

materials.

Type	Component	EC / S m^{-1}	TR / m K W^{-1}	Reference
Film	CNT	8.03×10^4	0.036	Ref S1
	Graphene	8.02×10^4	0.002	Ref S2
	PEDOT:PSS	5.0×10^4	0.555	Ref S3
	Garphene	1900 - 1.06×10^6	0.0013-0.0005	Ref S4
	Graphene	1.66×10^4 – 2.23×10^5	0.004-0.001	Ref S5
	Paper	< 1.00×10^{-15}	20	From Internet
	Fiber insulating board	< 1.00×10^{-15}	20.1	From Internet
Fabric	graphene	2.8×10^4	0.003	Ref S6
	Kevlar	< 1.00×10^{-15}	43.478	Ref S7
Composite	Graphene, PMMA	0.16-0.86	2.857-1.428	Ref S8
	EP, carbonized wood	6-12.5	1.923-1.724	Ref S9
	Graphene, CNT, PI	0.015-0.29	0.092-3.077	Ref S10
	Ag, Melamin, EP, CNT	253.4	3.279	Ref S11
	Glass microspheres, carbon nanofibers	0.0007	5.882	Ref S12
	Boron nitride, cellulose, epoxy	1.0×10^{-12}	0.319	Ref S13
	MWCNT, Fe3O4, Ag, epoxy	28	2.041	Ref S14
	Divinyltetramethyldisiloxane-bis(benzocyclobutene), boron nitride nanosheets	1.0×10^{-11} - 1.0×10^{-15}	0.555	Ref S15
	SWCNT, PEDOT:PSS, PVAc	1.35×10^5	5-2.5	Ref S16
	PTFE , boron nitride	9.1×10^{-13}-2.3×10^{-12}	3.257-1.383	Ref S17
	Graphene, boron nitride, epoxy	5.9×10^5	0.052	Ref S18
Others	Diamond	< 1.00×10^{-15}	0.001	From Internet
	Comercial insulating material	< 1.00×10^{-15}	28.6-6.2	From Internet
	Carbon (amorphous)	1-2000	~ 0.6	From Internet
	Solid solution	33.3-2000	2.5-5	Ref S19
	Superlattice	7.9×10^4	8.3	Ref S20
	CNT	166.7	6.666	Ref S21

16

	SiC, phenol−formaldehyde resin, loofah sponge	12.9-22.3	9.6-3.3	Ref S22
	Fluorinated graphene	4×10^{-5}-0.51	0.4	Ref S23
	MXene, PI	4	31.3	Ref S24
	CNT	4.2-658	5.9-2.4	Ref S1
	Carbonized bread	2×10^{-6}-37.7	16.7-3.6	Ref S25
3D networks (Sponge, foam, aerogel)	poly(3-hexylthiophene)	19	7.1	Ref S26
	LM, PDMS	800	2.0	Ref S27
	Silica	-	27.7	Ref S28
	SiC	-	28.6	Ref S29
	Silica	-	41.7	Ref S30
	Sheep wool	$<1.00\times10^{-15}$	25.6	From Internet
	Feather	$<1.00\times10^{-15}$	29.4	From Internet
	Cotton	$<1.00\times10^{-15}$	25	From Internet
	Air	$<1.00\times10^{-14}$- 1.00×10^{-8}	43.5	From Internet
	Carbonized nanofibrous sponge	0.03-4.72	37.0-26.3	This work

The data "From Internet" was inquired from "Thermal Conductivity Coefficients for common Solids, Liquids and Gases" (https://www.engineeringtoolbox.com/thermal-conductivity-d_429.html). Note that the typical electric insulator, such as cotton, sheep wool, feather, Kevlar fiber were given a universal EC in a value of $<1.00\times10^{-15}$ S m^{-1}.

The detailed legend of Figure 5a based on the data of Table S4 is shown here as follows:

Film: ▲ S1 ▲ S2 ▲ S3 ▲ S4 △ S5 ⬟ Fiber insulation board ◄ Paper
Fabric: ✳ S6 ✳ S7
Composite: ◆ S8 ◆ S9 ◆ S10 ◆ S11 ◆ S12 ◆ S13 ◆ S14 ◆ S15 ◆ S16 ◆ S17 ◆ S18
Others: ◐ S19 ● S20 ⬢ Diamond ▶ Commercial insulation materials ■ Carbon(armorphous)
3D networks (Sponge, foam, aerogel): ⊠ S21 ⊠ S22 ⊠ S23 ⊠ S24 ⊠ S1 ⊠ S25 ⊠ S26 ⊠ S27 ⊠ S28
⊠ S29 ⊠ S30 ★ Features ◆ Sheep wool ● Cotton ★ This work

17

References

S1. Lee, M. H.; Kang, Y. H.; Kim, J.; Lee, Y. K.; Cho, S. Y., Freely shapable and 3D porous carbon nanotube foam using rapid solvent evaporation method for flexible thermoelectric power generators. Adv. Energy Mater. **2019,** 9 (29), 1900914.

S2. Zhang, M.; Wang, Y.; Huang, L.; Xu, Z.; Li, C.; Shi, G., Multifunctional Pristine Chemically Modified Graphene Films as Strong as Stainless Steel. Adv. Mater. **2015,** 27 (42), 6708-13.

S3. Weathers, A.; Khan, Z. U.; Brooke, R.; Evans, D.; Pettes, M. T.; Andreasen, J. W.; Crispin, X.; Shi, L., Significant electronic thermal transport in the conducting polymer poly (3, 4-ethylenedioxythiophene). Adv. Mater. **2015,** 27 (12), 2101-2106.

S4. Peng, L.; Xu, Z.; Liu, Z.; Guo, Y.; Li, P.; Gao, C., Ultrahigh Thermal Conductive yet Superflexible Graphene Films. Adv. Mater. **2017,** 29 (27).

S5. Teng, C.; Xie, D.; Wang, J. F.; Yang, Z.; Ren, G. Y.; Zhu, Y., Ultrahigh Conductive Graphene Paper Based on Ball-Milling Exfoliated Graphene. Adv. Funct. Mater. **2017,** 27 (20).

S6. Li, Z.; Xu, Z.; Liu, Y.; Wang, R.; Gao, C., Multifunctional non-woven fabrics of interfused graphene fibres. Nat. Commun. **2016,** 7, 13684.

S7. Liu, Z.; Lyu, J.; Fang, D.; Zhang, X., Nanofibrous Kevlar Aerogel Threads for Thermal Insulation in Harsh Environments. ACS Nano **2019,** 13 (5), 5703-5711.

S8. Fan, Z.; Gong, F.; Nguyen, S. T.; Duong, H. M., Advanced multifunctional graphene aerogel – Poly (methyl methacrylate) composites: Experiments and modeling. Carbon **2015,** 81, 396-404.

S9. Shen, Z.; Feng, J., Preparation of thermally conductive polymer composites with good electromagnetic interference shielding efficiency based on natural wood-derived carbon scaffolds. ACS Sustain. Chem. Eng. **2019,** 7 (6), 6259-6266.

18

S10.   Zhang, F.; Feng, Y. Y.; Qin, M. M.; Gao, L.; Li, Z. Y.; Zhao, F. L.; Zhang, Z. X.; Lv, F.; Feng, W., Stress Controllability in Thermal and Electrical Conductivity of 3D Elastic Graphene-Crosslinked Carbon Nanotube Sponge/Polyimide Nanocomposite. Adv. Funct. Mater. **2019,** 29 (25).

S11.   Xu, Y.; Li, Y.; Hua, W.; Zhang, A.; Bao, J., Light-Weight Silver Plating Foam and Carbon Nanotube Hybridized Epoxy Composite Foams with Exceptional Conductivity and Electromagnetic Shielding Property. ACS Appl. Mater. Interfaces **2016,** 8 (36), 24131-42.

S12.   Herrera-Ramírez, L. C.; Cano, M.; de Villoria, R. G., Low thermal and high electrical conductivity in hollow glass microspheres covered with carbon nanofiber–polymer composites. Compos. Sci. Technol. **2017,** 151, 211-218.

S13.   Chen, J.; Huang, X.; Zhu, Y.; Jiang, P., Cellulose nanofiber supported 3D interconnected BN nanosheets for epoxy nanocomposites with ultrahigh thermal management capability. Adv. Funct. Mater. **2017,** 27 (5), 1604754.

S14.   Wang, L.; Qiu, H.; Liang, C.; Song, P.; Han, Y.; Han, Y.; Gu, J.; Kong, J.; Pan, D.; Guo, Z., Electromagnetic interference shielding MWCNT-Fe3O4@Ag/epoxy nanocomposites with satisfactory thermal conductivity and high thermal stability. Carbon **2019,** 141, 506-514.

S15.   Li, Q.; Chen, L.; Gadinski, M. R.; Zhang, S.; Zhang, G.; Li, H. U.; Iagodkine, E.; Haque, A.; Chen, L.-Q.; Jackson, T. N., Flexible high-temperature dielectric materials from polymer nanocomposites. Nature **2015,** 523 (7562), 576-579.

S16.   Yu, C.; Choi, K.; Yin, L.; Grunlan, J. C., Light-weight flexible carbon nanotube based organic composites with large thermoelectric power factors. ACS Nano **2011,** 5 (10), 7885-7892.

S17.   Pan, C.; Kou, K.; Jia, Q.; Zhang, Y.; Wu, G.; Ji, T., Improved thermal conductivity and dielectric properties of hBN/PTFE composites via surface treatment by silane coupling agent. Compos. B. Eng. **2017,** 111, 83-90.

19

S18.   Ma, T.; Liu, Z.; Wen, J.; Gao, Y.; Ren, X.; Chen, H.; Jin, C.; Ma, X.-L.; Xu, N.; Cheng, H.-M., Tailoring the thermal and electrical transport properties of graphene films by grain size engineering. Nat. Commun. **2017,** 8 (1), 1-9.

S19.   Zhao, K.; Blichfeld, A. B.; Eikeland, E.; Qiu, P.; Ren, D.; Iversen, B. B.; Shi, X.; Chen, L., Extremely low thermal conductivity and high thermoelectric performance in liquid-like $Cu_2Se_{1-x}S_x$ polymorphic materials. J. Mater. Chem. A **2017,** 5 (34), 18148-18156.

S20.   Wan, C.; Gu, X.; Dang, F.; Itoh, T.; Wang, Y.; Sasaki, H.; Kondo, M.; Koga, K.; Yabuki, K.; Snyder, G. J.; Yang, R.; Koumoto, K., Flexible n-type thermoelectric materials by organic intercalation of layered transition metal dichalcogenide TiS_2. Nat. Mater. **2015,** 14 (6), 622-7.

S21.   Gui, X.; Wei, J.; Wang, K.; Cao, A.; Zhu, H.; Jia, Y.; Shu, Q.; Wu, D., Carbon nanotube sponges. Adv. Mater. **2010,** 22 (5), 617-21.

S22.   Li, S.; Liu, D.; Li, W.; Sui, G., Strong and heat-resistant SiC-coated carbonized natural loofah sponge for electromagnetic interference shielding. ACS Sustain. Chem. Eng. **2019,** 8 (1), 435-444.

S23.   Zhang, C.; Huang, R.; Wang, P.; Wang, Y.; Zhou, Z.; Zhang, H.; Wu, Z.; Li, L., Highly Compressible, Thermally Conductive, yet Electrically Insulating Fluorinated Graphene Aerogel. ACS Appl. Mater. Interfaces **2020,** 12 (52), 58170-58178.

S24.   Liu, J.; Zhang, H. B.; Xie, X.; Yang, R.; Liu, Z.; Liu, Y.; Yu, Z. Z., Multifunctional, Superelastic, and Lightweight MXene/Polyimide Aerogels. Small **2018,** 14 (45), e1802479.

S25.   Yuan, Y.; Ding, Y.; Wang, C.; Xu, F.; Lin, Z.; Qin, Y.; Li, Y.; Yang, M.; He, X.; Peng, Q.; Li, Y., Multifunctional Stiff Carbon Foam Derived from Bread. ACS Appl. Mater. Interfaces **2016,** 8 (26), 16852-61.

S26.   Kroon, R.; Ryan, J. D.; Kiefer, D.; Yu, L.; Hynynen, J.; Olsson, E.; Müller, C., Bulk Doping of Millimeter-Thick Conjugated Polymer Foams for Plastic Thermoelectrics. Adv. Funct. Mater. **2017,** 27 (47), 1704183.

20

S27.   Yao, B.; Xu, X.; Li, H.; Han, Z.; Hao, J.; Yang, G.; Xie, Z.; Chen, Y.; Liu, W.; Wang, Q., Soft liquid-metal/elastomer foam with compression-adjustable thermal conductivity and electromagnetic interference shielding. Chem. Eng. J. **2021,** 410, 128288.

S28.   Yang, R.; Hu, F.; An, L.; Armstrong, J.; Hu, Y.; Li, C.; Huang, Y.; Ren, S., A hierarchical mesoporous insulation ceramic. Nano Lett **2019,** 20 (2), 1110-1116.

S29.   Liang, C.; Wang, Z., Eggplant-derived SiC aerogels with high-performance electromagnetic wave absorption and thermal insulation properties. Chem. Eng. J. **2019,** 373, 598-605.

S30.   Wang, F.; Dou, L.; Dai, J.; Li, Y.; Huang, L.; Si, Y.; Yu, J.; Ding, B., In situ Synthesis of Biomimetic Silica Nanofibrous Aerogels with Temperature-Invariant Superelasticity over One Million Compressions. Angew. Chem. Int. Ed. **2020,** 59 (21), 8285-8292.

21

6. Eidesstattliche Erklärung

(Eidesstattliche) Versicherungen und Erklärungen

(§ 9 Satz 2 Nr. 3 PromO BayNAT)

Hiermit versichere ich eidesstattlich, dass ich die Arbeit selbstständig verfasst und keine anderen als die von mir angegebenen Quellen und Hilfsmittel benutzt habe (vgl. Art. 64 Abs. 1 Satz 6 BayHSchG).

(§ 9 Satz 2 Nr. 3 PromO BayNAT)

Hiermit erkläre ich, dass ich die Dissertation nicht bereits zur Erlangung eines akademischen Grades eingereicht habe und dass ich nicht bereits diese oder eine gleichartige Doktorprüfung endgültig nicht bestanden habe.

(§ 9 Satz 2 Nr. 4 PromO BayNAT)

Hiermit erkläre ich, dass ich Hilfe von gewerblichen Promotionsberatern bzw. -vermittlern oder ähnlichen Dienstleistern weder bisher in Anspruch genommen habe noch künftig in Anspruch nehmen werde.

(§ 9 Satz 2 Nr. 7 PromO BayNAT)

Hiermit erkläre ich mein Einverständnis, dass die elektronische Fassung meiner Dissertation unter Wahrung meiner Urheberrechte und des Datenschutzes einer gesonderten Überprüfung unterzogen werden kann.

(§ 9 Satz 2 Nr. 8 PromO BayNAT)

Hiermit erkläre ich mein Einverständnis, dass bei Verdacht wissenschaftlichen Fehlverhaltens Ermittlungen durch universitätsinterne Organe der wissenschaftlichen Selbstkontrolle stattfinden können.

……………………………………………………………………………………………
Ort, Datum, Unterschrift